Etude physique de quelques problèmes de biologie : de la molécule individuelle à la cellule vivante

P.-F. Lenne

Université de Droit, d'Économie et des Sciences
d'Aix Marseille
Faculté des Sciences et Techniques de Saint Jérôme

DOSSIER DE TRAVAUX

présenté par

Pierre-François LENNE

pour obtenir une

HABILITATION À DIRIGER DES RECHERCHES

Etude physique de quelques problèmes de biologie : de la molécule individuelle à la cellule vivante

Discipline : Physique et Sciences de la Matière

Soutenance le 14 février 2007 Devant la Commission d'Examen :

François Amblard	(Rapporteur)
Claude Boccara	(Examinateur)
Maïté Coppey-Moisan	(Examinateur)
Hugues Giovannini	(Rapporteur)
Christian Le Grimellec	(Rapporteur)

Université de Droit, d'Économie et des Sciences
d'Aix Marseille
Faculté des Sciences et Techniques de Saint Jérôme

DOSSIER DE TRAVAUX

présenté par

Pierre-François LENNE

pour obtenir une

HABILITATION À DIRIGER DES RECHERCHES

Etude physique de quelques problèmes de biologie : de la molécule individuelle à la cellule vivante

Discipline : Physique et Sciences de la Matière

Soutenance le 14 février 2007 Devant la Commission d'Examen :

François Amblard	(Rapporteur)
Claude Boccara	(Examinateur)
Maïté Coppey-Moisan	(Examinateur)
Hugues Giovannini	(Rapporteur)
Christian Le Grimellec	(Rapporteur)

Table des matières

Introduction

Je suis chercheur au CNRS depuis environ 5 ans, et cela fait 8 ans que j'ai soutenu ma thèse de doctorat d'université. L'habilitation à diriger les recherches (HDR) marque une étape dans le parcours d'un chercheur travaillant en France. S'il est correctement jugé par ses pairs, on lui donne le droit d'encadrer des doctorants. Dans le but d'obtenir l'HDR, je retrace dans le présent rapport mon parcours de recherche depuis la fin de ma thèse jusqu'à aujourd'hui. Je l'ai rédigé en suivant un ordre chronologique. Le premier chapitre présente mon travail de post-doctorat, les deux suivants mes travaux en biologie et en physique à l'Institut Fresnel. Le dernier chapitre est consacré à mes projets actuels et à venir. J'inclus à la fin de chaque chapitre un ou deux articles significatifs.

Je suis physicien de formation : de 1991 à 1994, j'ai suivi le Magistère Interuniversitaire de Physique à l'Ecole Normale Supérieure de Paris. Après avoir obtenu le DEA de Physique des Solides de Paris, j'ai passé l'agrégation de Sciences Physiques en 1995. De 1995 à 1998, j'ai effectué ma thèse à l'Université Joseph Fourier de Grenoble, dans le laboratoire de Spectrométrie Physique, sous la direction de Bruno Berge. Mon travail de thèse a porté sur des phénomènes de transitions de phase dans des systèmes bidimensionnels. Plus précisément, j'ai travaillé sur deux exemples de cristallisation à la surface de l'eau : 1-) la croissance de solides dans une monocouche d'amphiphiles en interaction avec le volume et 2-) les cristaux 2-D de protéines.

Attiré par les questions de biologie, j'ai choisi de m'immerger dans un laboratoire de biologie en effectuant mon postdoctorat au laboratoire Européen de Biologie Moléculaire (EMBL) à Heidelberg. J'appartenais alors à l'équipe "Scanning Probe Techniques" d'Heinrich Hörber et l'équipe de biologie structurale de Matti Saraste. Si l'équipe de physiciens m'a accueilli pour développer et réaliser des expériences de microscopie à force atomique (AFM), c'est à Matti Saraste que je dois mon initation à la biologie et à ses grandes problématiques. Pendant deux ans, j'ai travaillé sur les propriétés mécaniques d'une protéine du cytosquelette, la spectrine, à l'échelle de la

molécule individuelle.

En 2000, j'ai intégré l'équipe d'Hervé Rigneault de l'Institut Fresnel à Marseille avec un projet sur l'exaltation de la luminescence pour la détection de molécules biologiques. J'ai été recruté Maître de Conférences à l'Ecole Nationale Supérieure de Physique de Marseille en octobre 2000 puis au CNRS l'année suivante. Mon activité s'est alors concentrée sur l'organisation membranaire à l'échelle sub-micronique et l'utilisation de structures optiques pour renforcer et structurer les champs lumineux. Les deux projets initialement séparés se sont rejoints aujourd'hui. Après six ans à l'Institut Fresnel, j'aborde actuellement un nouveau sujet sur la mécanique et la dynamique de l'adhésion lors d'un processus de développement embryonnaire.

La biologie et la physique ont des liens étroits mais ténus. Ces disciplines ont certes le même objet d'étude, la nature, mais les questions qu'elles posent, les langages et les méthodologies qu'elles utilisent les séparent souvent. Contrairement aux objets du monde inanimé, qui restent le sujet de prédilection des physiciens, les êtres vivants ont la capacité de se reproduire. Tous les processus biologiques sont compatibles avec ce principe et doivent être organisés pour servir cette fin. Même si la capacité de reproduction n'est pas en contradiction avec les lois de la physique, elle n'en fait pas partie et la notion de finalité est totalement étrangère au monde inanimé.

La physique et la biologie ne diffèrent pas seulement par leur objet d'étude mais aussi par leurs méthodes. Nous (physiciens) cherchons à proposer à partir des lois universelles de la physique des modèles simples formulés en langage mathématique, et testables expérimentalement. Nous développons et utilisons des appareillages sophistiqués et souvent complexes en regard de la simplicité apparente du système d'étude (en physique atomique par exemple). La situation est tout à fait différente en biologie. Le biologiste traîte d'un système extrêmement complexe, en formulant des questions précises et détaillées ; il utilise en général des outils simples (électrophorèses, chambres de culture, hottes, centrifugeuses et refrigérateurs,...) et a très peu recours aux mathématiques, car la modélisation n'est que rarement possible.

Physiciens et biologistes étudient parfois les mêmes objets mais avec des regards différents. Par exemple, le physicien étudie l'ADN comme un polymère aux propriétés remarquables, alors que le biologiste s'interesse à cette molécule en tant que support de l'hérédité. Existe-t-il un lien entre les propriétés mécaniques d'un polymère et sa propension à porter une information ? Si la question mérite d'être posée, il n'est toutefois pas certain que la réponse soit positive.

Les systèmes vivants étant aussi des systèmes physiques, certains mécanismes identifiés dans le monde inanimé peuvent fournir des modèles pour décrire les pro-

cessus biologiques. Mais quand le physicien parvient à modéliser certains mécanismes du vivant à l'aide d'équations, demandons-lui combien de paramètres ajustables il a utilisés. Comme le souligne M.E. Fischer, une des grandes figures de la physique statistique : "la question n'est pas de savoir comment vous expliquerez le phénomènes mais avec combien de constantes". Je considère que cette remarque vaut aujourd'hui aussi bien pour la physique et la biologie. Il est peut être illusoire d'imaginer que les cellules et les organismes vivants dans leur ensemble, issus d'un long processus d'évolution, puissent être décrits par des principes fondamentaux. Il est en revanche légitime de considérer que des principes physiques sous-tendent et guident une variété de processus cellulaires. Les formes et fonctions du vivant ont émergé à partir de mécanismes physico-chimiques à différentes échelles, donnant aux cellules et aux organismes vivants des propriétés multiples, sélectionnées par l'évolution. Les connections de la physique et de la biologie et leur utilité dépendent de notre capacité à reconnaître que les processus biologiques sont à la fois simples et déterminés par de multiples facteurs.

Grâce au développement des techniques expérimentales et des outils informatiques, il devient possible d'étudier quantitativement et en détail des processus biologiques complexes. Gageons que les biologistes vont être amenés à utiliser des techniques plus sophistiquées et que les physiciens caractériseront des systèmes d'une plus grande complexité, parmi lesquels les systèmes vivants constituent la catégorie ultime.

En attendant ce jour, voici ma modeste contribution de physicien à quelques problèmes de biologie.

Chapitre 1

Propriétés mécaniques de molécules individuelles de la spectrine, 1998-2000

Sommaire

1.1 Dépliement forcé par microscopie à force atomique

De septembre 1998 à septembre 2000, j'ai travaillé en tant que post-doctorant au sein du laboratoire européen de biologie moléculaire (EMBL) à Heidelberg, grâce à une bourse Marie Curie. Lors d'une visite de ce laboratoire en 1997, j'avais décidé d'étudier les propriétés mécaniques d'une protéine du cytosquelette à l'échelle de la molécule individuelle. Ce souhait avait été motivé par la lecture d'un article[1] sur le dépliement forcé d'une protéine géante du sarcomère des muscles striés, la titine, par l'équipe d'Hermann Gaub à Münich. Il indiquait que les courbes de force extension d'une protéine individuelle étirée par un microscope à force atomique fournissent une "empreinte" des différents modules de la protéine, qui se déplient un à un. Pour préciser le lien entre la réponse mécanique d'un module protéique et sa structure, j'ai voulu aborder deux questions : 1-) une protéine de structure différente de la titine, - mais également soumises à des contraintes mécaniques -, a-t-elle une "empreinte"

[1] Rief M, Gautel M, Oesterhelt F, Fernandez JM, Gaub HE : Reversible unfolding of individual titin immunoglobulin domains by AFM. Science 1997, 276 :1109-1112.

mécanique différente ? ; 2-) est-il possible de modifier la topologie mécanique d'une protéine en modifiant ponctuellement sa séquence ? Pour répondre à ces questions, j'ai bénéficié de l'instrumentation développée dans l'équipe de microscopie de champ proche d'Heinrich Hörber et d'un système biologique pertinent, la spectrine. La spectrine est une protéine du cytosquelette, associée à l'actine. Elle forme le réseau du cytosquelette des globules rouges. Comme la titine, la spectrine est une protéine modulaire formée de la répétition d'un motif de base, appelé "domaine". Un domaine de spectrine comporte 106 acides aminés formant trois hélices-α connectées par deux boucles, alors qu'un domaine de titine a une structure en feuillets-β (Figure 1.1).

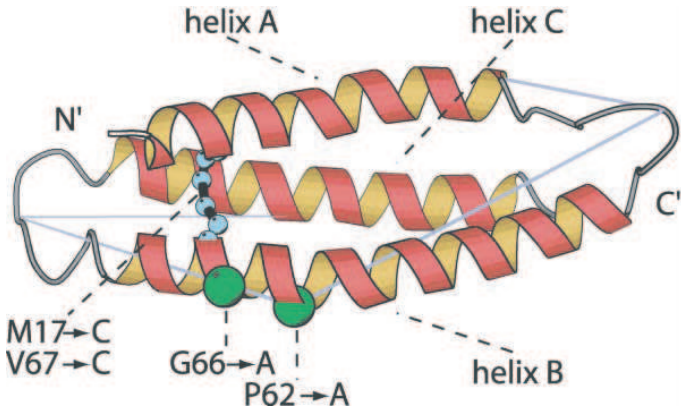

FIG. 1.1 – Structure du domaine R16 de la spectrine. *Les atomes C_α des deux résidus substitués par des alanines dans le mutant AA sont marqués en vert. Le pont disulfure introduit dans le mutant CC est marqué en bleu.*

Le domaine de spectrine que j'ai étudié est caractéristique de tous les membres de la superfamille de la spectrine, incluant la spectrine, l'α-actinine, la dystrophine et l'utrophine. Le génome humain comprend environ cinq cents types de domaines de spectrine, le plus souvent dans les protéines associées à l'actine. J'ai utilisé l'AFM pour suivre les états et les transitions de dépliement de protéines polymériques constituées de la répétition d'un domaine identique de la spectrine.

Pour cela, je me suis initié à la biologie moléculaire, en particulier aux techniques de clonage et d'expression de protéines recombinantes. J'ai été aidé dans cette tâche par Arnt Raae, professeur de biochimie à l'université de Bergen en Norvège, qui était alors en année sabbatique dans le groupe de Matti Saraste.

A l'aide d'un AFM développé à l'EMBL, j'ai démontré que contrairement à ce qui avait été observé pour la titine, le dépliement d'un domaine de spectrine peut se produire par plus d'une étape pendant son étirement. Les courbes de force-extension des molécules individuelles de spectrine sont en effet compatibles avec l'existence d'au

moins un état intermédiaire entre les conformations repliée et totalement dépliée du domaine [30] (article joint). Pour expliquer ces résultats, j'ai proposé un modèle simple rendant compte du dépliement par étirement d'un domaine de spectrine, comme un système énergétique à trois niveaux, séparés par des barrières d'énergie. Une simulation Monte Carlo s'appuyant sur ce modèle, permet de reproduire les données expérimentales et d'évaluer certaines caractéristiques des barrières d'énergie.
Nous avons également construit et étudié des mutants de la spectrine pour corréler la structure fine des domaines de spectrine et leur stabilité mécanique. En particulier, j'ai démontré qu'il est possible de modifier la topologie mécanique de la spectrine en introduisant des mutations ponctuelles [20]. Le premier mutant (CC) comportait deux cystéines entre deux hélices-α pouvant former un pont disulphure. La présence de ce pont raccourcit la longueur étirée d'un domaine, comme le révèlent les courbes de force-extension. Après destablisation chimique du pont, il est en outre possible de suivre par mesure de force la modification de la topologie mécanique de la protéine. Dans le second mutant (AA), deux résidus proline et glycine, substitués par deux résidus alanine stabilisent l'hélice centrale. Contrairement au domaine natif, les courbes de force-extension obtenues pour ce mutant ne présentent pas d'intermédiaires de dépliement. Mes travaux expérimentaux ont stimulé des calculs de dynamique moléculaire dans l'équipe de Michaël Nilges, qui a montré que le dépliement forcé d'une protéine peut suivre plusieurs chemins et en accord avec mes résultats expérimentaux, qu'une mutation ponctuelle peut modifier drastiquement ces chemins. La dynamique moléculaire suggère que les intermédiaires stables sont associés à l'apparition d'un coude dans l'hélice centrale [20].

Ces résultats montrent que l'AFM est un outil de spectroscopie capable de révéler certains détails du paysage énergétique des protéines et les probabilités de transition entre différents états conformationnels. Mes travaux ont donné lieu à trois publications dans des journaux internationaux [30, 26, 20] et à un chapitre de livre [21].

Une dizaine de laboratoires travaille actuellement sur ce type de questions, associant toujours l'utilisation d'une instrumentation de mesure de force à l'ingénierie de protéines. La méthode de dépliement forcé est particulièrement intéressante pour les protéines qui sont sous contraintes mécaniques dans leur contexte physiologique, et complète les techniques plus classiques de dénaturation chimique ou thermique.

FEBS Letters 476 (2000) 124–128 FEBS 23827

States and transitions during forced unfolding of a single spectrin repeat

P.-F. Lenne*, A.J. Raae, S.M. Altmann, M. Saraste, J.K.H. Hörber

European Molecular Biology, Cell Biology and Biophysics Programme, P.O. Box 10.2209, D-69012 Heidelberg, Germany

Received 10 May 2000; received in revised form 29 May 2000

Edited by Giorgio Semenza

Abstract Spectrin is a vital and abundant protein of the cytoskeleton. It has an elongated structure that is made by a chain of so-called spectrin repeats. Each repeat contains three antiparallel α-helices that form a coiled-coil structure. Spectrin forms an oligomeric structure that is able to cross-link actin filaments. In red cells, the spectrin/actin meshwork underlying cell membrane is thought to be responsible for special elastic properties of the cell. In order to determine mechanical unfolding properties of the spectrin repeat, we have used single molecule force spectroscopy to study the states of unfolding of an engineered polymeric protein consisting of identical spectrin domains. We demonstrate that the unfolding of spectrin domains can occur in a stepwise fashion during stretching. The force–extension patterns exhibit features that are compatible with the existence of at least one intermediate between the folded and the completely unfolded conformation. Only those polypeptides that still contain multiple intact repeats display intermediates, indicating a stabilisation effect. Precise force spectroscopy measurements on single molecules using engineered protein constructs reveal states and transitions during the mechanical unfolding of spectrin. Single molecule force spectroscopy appears to open a new window for the analysis of transition probabilities between different conformational states.

Key words: Force spectroscopy; Single molecule; Spectrin repeat; Unfolding intermediate state

1. Introduction

The modular structure of proteins in natural fibres and the cytoskeleton seems to be a general strategy for resistance against mechanical stress [1]. One of the most abundant modular proteins in the cytoskeleton is spectrin. In erythrocytes, spectrin molecules are part of a two-dimensional network that is assumed to provide the red blood cells with special elastic features [2]. The basic constituent of spectrin subunits is the repeat which has about 106 amino acids and is made of three antiparallel α-helices, folded into a left-handed coiled-coil [3]. The repeats are connected by a helical linker [4,5].

The mechanical properties of several modular proteins have already been investigated by atomic force microscopy (AFM) [6], especially titin [7]. Such experiments have demonstrated that the elongation events observed during stretching of single proteins may be attributed to the unfolding of individual domains; experiments with optical tweezers have corroborated these results [8,9]. These studies suggest that single domains unfold one at a time in an all-or-none fashion when subjected to directional mechanical stress. More recently, Oesterhelt et al. [10] have shown that individual bacteriorhodopsins can unfold in a stepwise manner.

In a typical experiment, single proteins are attached to properly prepared surfaces and subsequently captured on AFM tips. They can be stretched to more than 10 times their folded lengths, reaching almost the total contour length (Fig. 1). The force–extension curves show a characteristic sawtooth-like pattern. The reaction coordinate of unfolding is imposed by the direction of pulling, and unfolding events occurring in a single protein can be studied in this way. Each peak is attributed to the breakage of a folded structure.

Rief et al. [11] have shown that under mechanical stress the repeats of the native spectrin break as well defined units. As these repeats are homologous but not identical, we have engineered a polymeric molecule consisting of four identical repeats referred to as $(R16)_4$ in the following, in order to get a better understanding of the mechanical properties of the spectrin repeat. The unfolding features in the motif should thus be multiplied and could be compared within the frame of one repeat [12,13]. The polymeric protein was constructed from the repeat R16 of the α-spectrin chain since the structure had already been determined by nuclear magnetic resonance spectroscopy [3]. The essential features of its structure are confirmed by the recent crystallographic study [5].

We used AFM to unfold the polymeric protein consisting of identical domains. We shall demonstrate that the unfolding of a single spectrin repeat can occur in a stepwise fashion during stretching.

2. Materials and methods

2.1. Construction of polymeric R16

A modified R16 repeat was produced by PCR using the pET R16 plasmid [14] as template. The 5′ primer sequence, CCGGATCC-TCCATGGAAATGAGCGCTGCCCGCGCGAAGCTCAACGAG-TCG, contains a *Bam*HI and a *Bsp*HI site, the initiation codon as well as an N-terminal five-residue extension of the original R16 sequence. The 3′ primer, GGGCGGCCGCTTATTAGCAACAGGTCATGA-TGTACTCCAGGGACTCCTCCAGACGTTGCCCCCGAGC, contains *Nco*I and *Not*I sites as well as two stop codons. The 3′ primer adds an eight-residue extension to the R16 repeat as well as two cysteine residues to the end of the expressed protein products. The gene sequence is extended at both ends so that the polymeric protein product contains a 13-residue linker between the consecutive R16 units, and has two cysteine residues at the C-terminus. The PCR product was cut with *Bam*HI and *Not*I, ligated into a pBluescript SK plasmid and amplified in DH-5α cells. The modified R16 sequence was cut from the vector with *Nco*I and *Not*I, and ligated in frame into the *Nco*I restriction site of a domestic pET24d derivative that confers a six-residue histidine tag and a TEV protease site to the N-terminus of the protein. This vector was cut with two different combinations of restriction enzymes, *Bsp*HI/*Xba*I and *Nco*I/*Not*I, respectively. After purification, the fragments containing the R16 sequences were joined by ligation at the *Bsp*HI and *Nco*I sites, and simultaneously ligated into a pET24d vector which was opened with *Xba*I and *Not*I, and

*Corresponding author. Fax: (49)-6221-387 306.
E-mail: lenne@embl-heidelberg.de

0014-5793/00/$20.00
PII: S0014-5793(00)01704-X

dephosphorylated with shrimp alkaline phosphatase. After transformation, DH-5α cells containing the two-repeat construct were identified by PCR analysis of the bacterial colonies. The four-repeat construct $(R16)_4$ was subsequently made by iterating the same procedure.

2.2. Protein expression and purification

For expression, 0.1 μg of plasmid DNA was used to transform competent BL-21 cells. After growth at 37°C to $A_{600} = 0.7$, the cells were equilibrated at 30°C before isopropyl-1-thio-β-D-thiogalactopyranoside was added to a final concentration of 0.4 mM. After induction for 8 h, the cells were harvested by centrifugation. The cells were suspended in lysis buffer containing 50 mM Tris–HCl, pH 8.0, 30 mM imidazole, 200 mM NaCl, 0.2% NP-40, 0.15 mM phenylmethylsulfonyl fluoride and 0.1 mM 4-(2-aminoethyl)-benzolsulfonyl fluoride, and lysed by sonication. The lysate, 40 ml from a 500 ml cell culture, was mixed with 1.5 ml Ni-NTA resin and kept 10 min on ice. The Ni-NTA/lysate suspension was filtered through a 10 ml Bio-Rad polyprep column. The filtrate was reloaded on the column, and the resin was first washed with the lysis buffer, then with the lysis buffer without detergent containing 1 M NaCl, and with 30 mM imidazole. The bound protein was eluted in 1 ml 200 mM imidazole. The four-repeat construct was almost quantitatively recovered in a soluble state after expression at 30°C.

2.3. AFM

The experiments were performed with an AFM developed at EMBL working in the so-called force spectroscopy mode [15]. The cantilevers (model MLCT-AUHW, Park Scientific, Sunnyvale, CA, USA) were calibrated by using the equirepartition theorem as described by e.g. Florin et al. [16]. The proteins were kept in buffer 50 mM Tris–HCl pH 8.0, 50 mM NaCl. A drop of 40 μl of protein solution (100 μg/ml) was deposited on freshly sputtered gold surfaces as proteins have cysteine residues at the C-terminus to bind covalently to gold. The proteins were allowed to adsorb for 10 min before the sample was rinsed with buffer and brought into the fluid experimental chamber of the AFM. The single proteins were picked up at random by approaching the sample towards the tip while monitoring the deflection amplitude. After contact with the surface was established, the maximum normal forces during the spectroscopy cycles were kept as low as possible. Approach/retraction cycles of the sample with respect to the AFM tip were used to probe the force–extension curves of single molecules of spectrin. We used pulling speeds between 0.3 and 15 nm/ms. The AFM controls distance with 0.1 nm accuracy and the applied force with pN precision.

3. Results and discussion

3.1. Single molecule force spectroscopy on $(R16)_4$

We used recombinant DNA techniques to construct tandem repeats from a single spectrin domain (see Section 2). The method extends the monomer (R16) at both ends so that the polymeric protein product contains a 13-residue linker between the consecutive R16 units and has two cysteine residues at the C-terminal end.

In Fig. 2, an SDS–PAGE analysis of the mono-, di- and tetrameric R16 repeats is shown together with the repeat 13–18 section from the chicken brain α-spectrin chain. The apparent molecular weight of the four-repeat construct $(R16)_4$ is 64 kDa. Due to the extensions in the connecting regions and at the N- and C-terminal ends, the total molecular size is in the same range as that of the native hexameric spectrin repeat 13–18 that was studied by Rief et al. [11].

The force–extension relationships for $(R16)_4$ were measured using an AFM developed at EMBL (Section 2). The proteins formed covalent bonds with the gold surfaces through cysteine residues which were introduced at the C-terminal end. The protein-coated surfaces were then carefully brought into contact with the tip and single proteins were picked up by unspecific binding. By retracting the sample holder away from the AFM tip, single proteins could be completely extended.

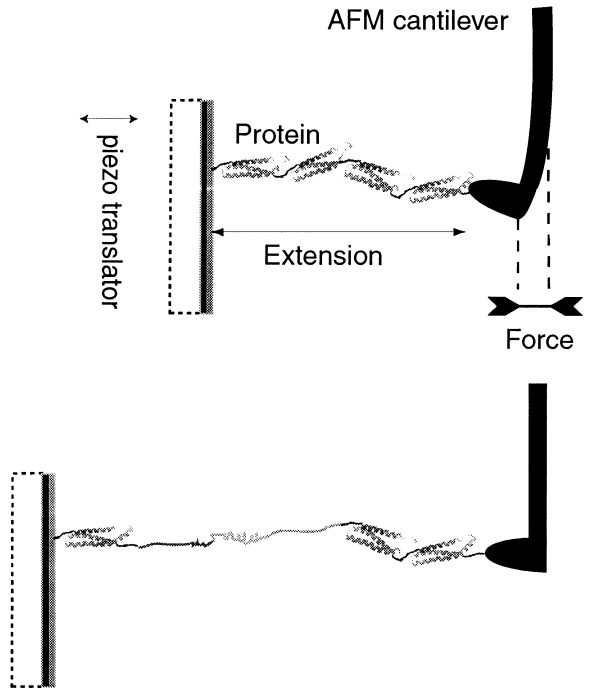

Fig. 1. AFM force measurements. Experimental scheme for protein 'fishing'.

Force–extension curves present the sawtooth-like pattern typical for modular proteins (Fig. 3). Each peak is interpreted as an unfolding event. The loss of each folded structure in the spectrin chain allows a gain of length for the unfolded part of the chain. After each peak, the force drops as a new length of the polypeptide chain is gained but has not yet been extended. The protein is then stretched further until the force is sufficient for another part of the folded structure to unfold. The maximum extension is variable as the polymer is picked up at random positions and not necessarily at its end.

The force–extension curves can be well described by a worm-like chain model (WLC) [17]. It predicts the isothermal restoring force of a flexible polymer, acting as an entropic spring during extension. Fits of the force–extension curves to the WLC model [18] resulted in a persistence length of

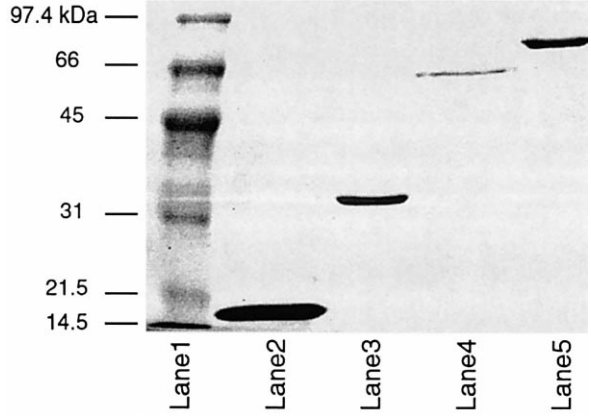

Fig. 2. An SDS–PAGE analysis of the spectrin R16 polymeric products. Lane 1: Bio-Rad LMW markers. Lane 2: monomeric R16 spectrin repeat. Lane 3: dimeric R16 spectrin. Lane 4: tetrameric R16 spectrin. Lane 5: the repeats 13–18 from the α-spectrin chain.

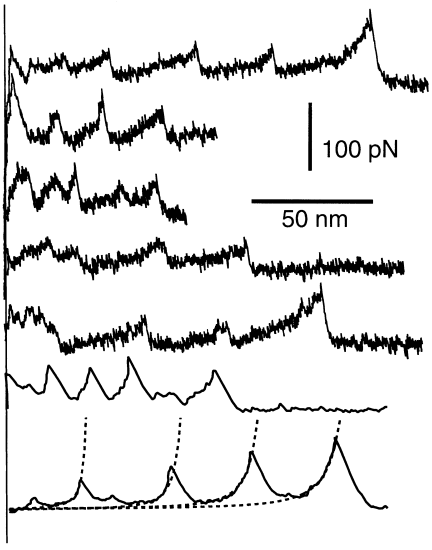

Fig. 3. Unfolding traces of a spectrin construct made of four identical tandem domains $(R16)_4$. The five upper curves were recorded at a pulling speed of 0.3 nm/ms and the two last at 3 nm/ms. The WLC model fits to the left-hand slopes of the unfolding patterns with a persistence length of $p = 0.59 \pm 0.22$ nm (see last curve). As the proteins are picked up at random, the maximum extension varies from one curve to the other but never exceeds the total contour length of the protein.

$p = 0.59 \pm 0.22$ nm ($n = 20$). Two consecutive force peaks are spaced by a distance that reflects the gain of length produced by a single unfolding event. These distances were measured for 250 unfolding events.

A histogram of distances (Fig. 4a) reveals a length distribution with two major peaks, at 15.5 nm (± 3.5 nm) and 31 nm (± 7 nm) when fitted with a mixture of two Gaussians. The force distributions associated with the short and long elongation events are also clearly distinct (Fig. 4b,c). The mean force for the short and long elongation events are 60 and 80 pN, respectively, at a pulling speed of 3 nm/ms.

General features of the unfolding events are provided by a detailed statistical analysis of the whole set of measurements:

1. The short unfolding events are most likely for a short extension, i.e. at the first stage of pulling (80% below 35 nm, $n = 87$) of the protein whereas the long unfolding events are observed at longer extension (50% above 35 nm, $n = 94$).
2. When two short unfolding events occur, they are consecutive in 90% of the cases.

We measured the same unfolding patterns for different speeds (0.3, 0.75 and 1.5 nm/ms). The mean unfolding force was decreased by approximately 20% when the pulling speed was reduced by a factor of 10 (see insets in Fig. 4b,c). The strength of the bonds that stabilise protein structures can depend on the speed of retraction as it has been shown for the biotin/streptavidin system [19].

3.2. Reversibility of unfolding

After reaching the extended state and before rupturing the bond between the protein and the tip, the protein was relaxed to its initial length (Fig. 5). After waiting for 5 s, the protein was stretched again and four force peaks were observed. This suggests that the four domains spontaneously refold during

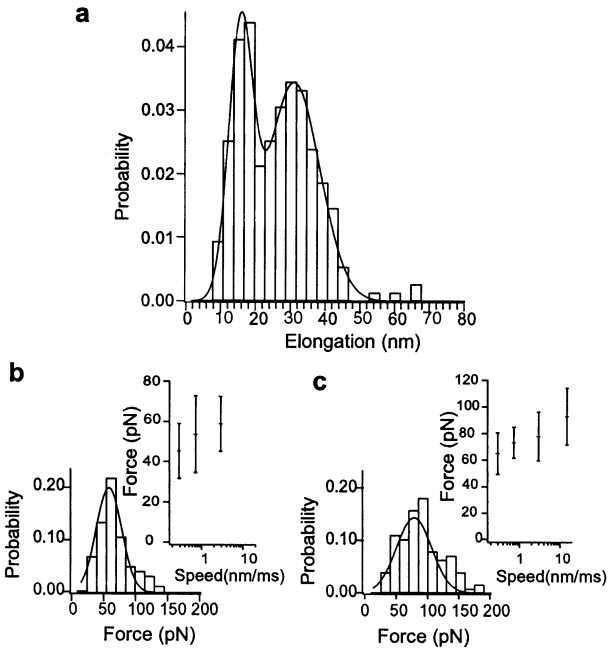

Fig. 4. Elongation events and unfolding forces of the spectrin construct $(R16)_4$. (a) Histogram probability of elongation after an unfolding event ($n = 250$). The line corresponds to a fit by a normalised function, the sum of two Gauss functions. The Gauss functions are centred on 15.5 nm and 31 nm. Unfolding force probability histogram and force–speed dependence for short elongation events (b) and long elongation events (c).

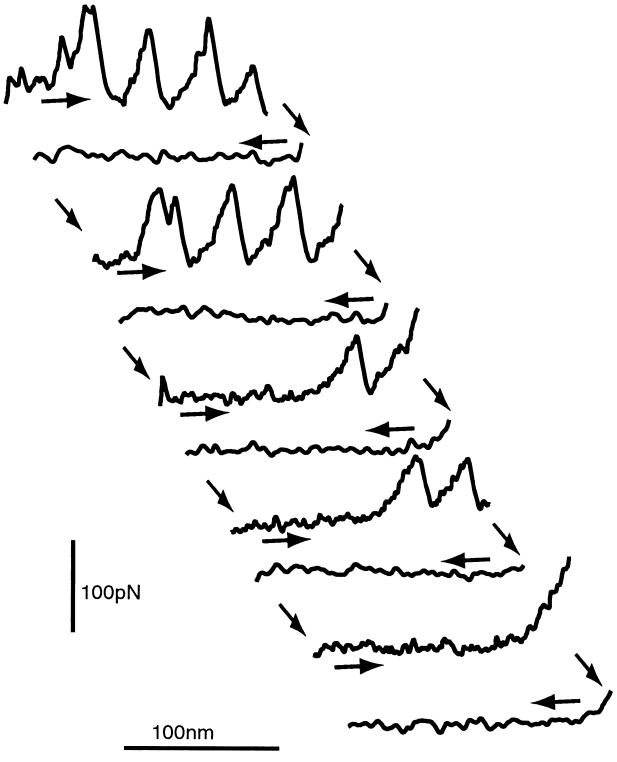

Fig. 5. Cycles of unfolding–refolding of a single molecule of spectrin (see text).

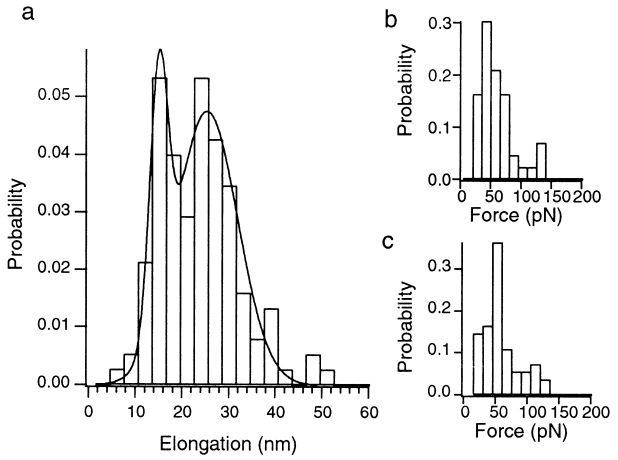

Fig. 6. Elongation events and unfolding forces of the natural hexameric 13–18 spectrin repeat (from chicken brain α-spectrin). (a) Histogram probability of elongation after an unfolding event ($n = 125$). The line corresponds to a fit by a normalised function, the sum of two Gauss functions. The Gauss functions are centred on 15 nm and 26 nm. Unfolding force probability histogram and for short elongation events (b) and long elongation events (c) at a pulling speed of 0.3 nm/ms.

relaxation. If the relaxation time is decreased to 1 s, the number of refolded domains is decreased in each cycle. This demonstrates that refolding occurs on a time scale of seconds and is therefore significantly slower than the unfolding rate.

3.3. Comparison with the native spectrin repeats

We have carried out equivalent measurements with another construct made of six homologous but non-identical repeats (the repeats 13–18 from chicken brain α-spectrin, see also [11]). Our measurements result in a similar distribution of elongation events; the most probable events occur at 15 and 26 nm (Fig. 6). The mean unfolding force is 55 pN for both the short and long elongation events with a pulling speed of 0.3 nm/ms. The long elongation event is in agreement with the results reported by Rief et al. [11]. However, because we were able to collect much more data than Rief et al., we could clearly observe short elongation events in our measurements both on $(R16)_4$ as well as R13–R18 when plotting their elongation length distributions.

3.4. Intermediates

The origin of the two distinct elongation events observed can have several causes. One can argue that short elongations are due to multiple-molecule pick-up. We showed that short elongations correspond to low forces and long elongations to large forces. Multiple pick-ups could indeed lead to shorter elongations but this would automatically have to go along with higher forces than for the long elongations which fit the unfolding length of a single repeat very well. We carefully excluded the possibility of multiple pick-ups by discarding any force curves displaying an off-set in the force indicating multiple parallel springs, i.e. multiple-molecule pick-up, from our analysis.

The second possible cause of a 'premature' unfolding of the R16 motif could be due to destabilising long range surface forces. These would have to reach further than 10 nm from the surface, as we observed partial unfolding at a distance out to more than 50 nm.

This is not the case. We recorded force spectra of levers in water and phosphate-buffered saline at distances between 5 and 30 nm from the surface clearly showing that the electrostatic forces can be completely ignored at a few nanometers from the surface [20].

A third possibility could be that the proteins denature at least partially on the surface. This would, in addition to the cysteine–gold bond, increase the binding forces. It would also preclude the observation of a total of more than three repeats unfolding partially or fully in one trace. In several measurements where partial unfolding occurred, the unfolding lengths sum to more than these three repeats. If the protein was only partially denatured, it seems very unlikely that reversibility, as we observed it, would be possible. Refolding of the rest of such a partially denatured domain seems very unlikely. Also the rest of the domain can be expected to be distorted greatly and increasingly by the recurrence of the surface forces influence which led to the partial denaturing.

These reasons make multiple pick-ups and at least direct surface effects quite unlikely, and we believe that the existence of the different elongation events is due to at least one stable intermediate between the folded state and completely unfolded state during forced unfolding.

Thermodynamic studies have not yet documented such an intermediate: fluorescence spectroscopy and circular dichroism measurements have shown that single spectrin repeats undergo a reversible two-state transition [21,22]. Statistical analysis of the force curves shows that well defined short elongation events of 15.5 nm take place. The 15.5 nm elongation is half of that produced by the total unfolding of one domain. It may thus correspond either to the gain of length between a folded and unfolded domain or to the gain of length between a partially and completely unfolded domain. The variation in our length distributions is large but comparable with data of Yang et al. [23]. This broadness is partly attributed to the fact that we chose to measure the distance between peaks rather than the gain of contour lengths between consecutive peaks which are obtained by multiple-parameter fits [23]. Moreover, spectrin unfolds at very low forces, and therefore unavoidably any distribution is broadened in comparison to the unfolding of titin for instance. It could also be a consequence that several possible intermediates contribute to the distributions.

We assume that, as two short elongation events are consecutive in most cases, the unfolding of one domain results from at least two transitions, each producing on average a similar elongation. An intriguing observation is then that the rest of the partially unfolded domain is stable on a time scale of 1/10 of a second as the pulling speed is in the nm/ms range. This is an unexpected result and needs more in-depth study.

A molecular dynamics simulation [24] has recently suggested that protein domains such as the fibronectin-type 3 module can unfold in a stepwise fashion. In this case, unfolding follows a pathway in which a 'β-sandwich' first separates from the fold, and the individual β-sheets unfold secondly. The molecular pathway of unfolding is unknown for the spectrin domain, but it may well involve a partial opening of the bundle and/or the loss of the secondary structure at the ends of the helices which may be elongated before the helical bundle finally opens.

The different unfolding events are not only distinct in elon-

gation lengths but also in the unfolding forces. The mean unfolding force for short elongation events is 60 pN whereas the force associated to long elongation events is 80 pN (at a pulling speed of 3 nm/ms). This shows that the transition from a native folded conformation to an intermediate is mechanically different from the transition from a totally folded conformation to a completely unfolded conformation.

The feature that the unfolding of the domains depends on the extension of the chain is also interesting by itself. At short extensions of the polypeptide chain, short unfolding events are more likely than long ones. This behaviour suggests that the selection of the unfolding pathway may be influenced by changes in the mechanical properties during the extension of polypeptide chain. Relaxation processes following the breakage of folded structures possibly govern the access to intermediates. This may indicate as well that the unfolding of tandem repeats in spectrin chains is not completely independent [25]. The tandem spectrin repeats are not classical independent structural domains, and have stabilising interactions. A folded repeat may have a different stability depending on whether its neighbouring repeats are folded or unfolded. As suggested by our measurements, a folded repeat unfolds more likely by steps when its neighbouring repeats are folded (at small extension of the chain) than when they are unfolded (at large extension). The observed intermediates are conformational states which are stable from milliseconds to seconds, i.e. on time scales accessible in AFM measurements.

Although the molecular complexity of unfolding pathways can be very high, our AFM measurements demonstrate that force spectroscopy of single properly engineered proteins can give important clues on thermally averaged energy landscapes relevant on laboratory time scales. In the future, we expect an increasing contribution by force spectroscopy measurements to the understanding of protein folding as proteins will be engineered in order to systematically perturb the unfolding pathways imposed by the real space directionality in such measurements.

Acknowledgements: We thank M. Nilges and J. Linge for discussions, L. Serrano and T. Gibson for reading of this manuscript, and G. Stier for his technical advice. Support was provided by a grant to P.-F.L. from the European Commission (TMR) and a grant to A.J.R. from the Norwegian Research Council.

References

[1] Smith, B.L. et al. (1999) Nature 399, 761–763.
[2] Elgsaeter, A., Stokke, B.T., Mikkelsen, A. and Branton, D. (1986) Science 234, 1217–1223.
[3] Pascual, J., Pfuhl, M., Walther, D., Saraste, M. and Nilges, M. (1997) J. Mol. Biol. 273, 740–751.
[4] Djinovic-Carugo, K., Young, P., Gautel, M. and Saraste, M. (1999) Cell 98, 537–546.
[5] Grum, V.L., Li, D., MacDonald, R.I. and Mondragon, A. (1999) Cell 98, 523–535.
[6] Fisher, T.E., Oberhauser, A.F., Carrion-Vazquez, M., Marszalek, P.E. and Fernandez, J.M. (1999) Trends Biochem. Sci. 24, 379–384.
[7] Rief, M., Gautel, M., Oesterhelt, F., Fernandez, J.M. and Gaub, H. (1997) Science 276, 1109–1112.
[8] Kellermayer, M.S., Smith, S.B., Granzier, H.L. and Bustamante, C. (1997) Science 276, 1112–1116.
[9] Tskhovrebova, L., Trinick, J., Sleep, J.A. and Simmons, R.M. (1997) Nature 387, 308–312.
[10] Oesterhelt, F., Oesterhelt, D., Pfeiffer, M., Engel, A., Gaub, H.E. and Muller, D.J. (2000) Science 288, 143–146.
[11] Rief, M., Pascual, J., Saraste, M. and Gaub, H. (1999) J. Mol. Biol. 286, 553–561.
[12] Carrion-Vazquez, M., Oberhauser, A.F., Fowler, S.B., Marszalek, P.E., Broedel, S.E., Clarke, J. and Fernandez, J.M. (1999) Proc. Natl. Acad. Sci. USA 96, 3694–3699.
[13] Yang, G. et al. (2000) Proc. Natl. Acad. Sci. USA 97, 139–144.
[14] Pascual, J., Pfuhl, M., Rivas, G., Pastore, A. and Saraste, M. (1996) FEBS Lett. 383, 201–207.
[15] Rief, M., Oesterhelt, F., Heymann, B. and Gaub, H.E. (1997) Science 275, 1295–1297.
[16] Florin, E.-L., Rief, M., Lehmann, H., Ludwig, M., Dornmair, C., Moy, V.T. and Gaub, H.E. (1995) Biosens. Bioelectron. 10, 895–901.
[17] Fixman, M. and Kovac, J. (1973) J. Chem. Phys. 56, 1564–1568.
[18] Bouchiat, S.M., Wang, M.D., Allemand, J.-F., Strick, T., Block, S.M. and Croquette, V. (1999) Biophys. J. 76, 409–413.
[19] Merkel, R., Nassoy, P., Leung, A., Ritchie, K. and Evans, E. (1999) Nature 397, 50–53.
[20] Butt, A.-J. (1991) Biophys. J. 60, 1438–1444.
[21] Lusitani, D., Menhart, N., Keiderling, T.A. and Fung, L.W.-M. (1998) Biochemistry 37, 16546–16554.
[22] DeSilva, T.M., Harper, S.L., Kotula, L., Hensley, P., Curtis, P.J., Otvos Jr., L. and Speicher, D.W. (1997) Biochemistry 36, 3991–3997.
[23] Carrion-Vazquez, M., Marszalek, P.E., Oberhauser, A.F. and Fernandez, J.M. (1999) Proc. Natl. Acad. Sci. USA 96, 11288–11292.
[24] Paci, E. and Karplus, M. (1999) J. Mol. Biol. 288, 441–459.
[25] Menhart, N., Mitchell, T., Lusitani, D., Topouzian, N. and Fung, L.W.-M. (1996) J. Biol. Chem. 271, 30410–30416.

Chapitre 2

Domaines membranaires et analyse du confinement, 2001-2006

2.1 Introduction et contexte

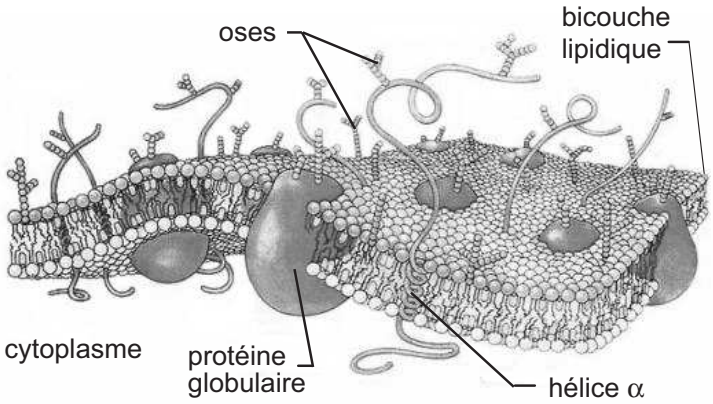

FIG. 2.1 – *Modèle de Singer et Nicolson, 1972.*
Schéma inspiré par le modèle de Singer et Nicolson montrant la mosaïque fluide. Figure tirée de [Bretscher MS : The molecules of the cell membrane. Sci. Am. 1985, 253 :100-108].

L'histoire moderne des membranes biologiques commence en 1972 avec le modèle fondateur de mosaïque fluide de Singer et Nicolson postulant que la bicouche lipidique constitue une matrice fluide dans laquelle les protéines sont insérées, libres de diffuser et distribuées de manière aléatoire[2] (Figure 2.1). Les expériences menées depuis, principalement par des mesures de la diffusion, ont cependant révélé une

[2]Singer SJ, Nicolson GL : The fluid mosaic model of the structure of cell membranes. Science 1972, 175 :720-731.

grande complexité de l'organisation dynamique des membranes biologiques, reliée aux fonctions biologiques qui y sont accomplies. Ce domaine de recherche très actif réunit une communauté de biologistes, biochimistes, biophysiciens et physiciens au sein de laquelle, dans l'attente de l'émergence d'un modèle réaliste de membranes cellulaires, débats et controverses battent leur plein. Au coeur du débat se trouve en particulier le concept de radeaux lipidiques ou "lipid raft", proposé initialement en 1988 par deux biologistes, K. Simons et G. Van Meer, pour expliquer l'asymétrie du transport membranaire (Figure 2.2). Ces microdomaines de quelques dizaines de nanomètres serviraient de plate-formes de tri et de signalisation, en recrutant des protéines ayant pour eux une grande affinité. Ils sont décrits comme étant riches en cholestérol, glycolipides, sphingolipides et en phospholipides présentant moins d'insaturations que celles des lipides dans la membrane environnante, ce qui permet un meilleur compactage des chaînes saturées de sphingolipides. Dans cette description, la présence de cholestérol induirait une phase liquide ordonné ayant une fluidité plus faible que le reste de la membrane. De nombreuses questions concernant ces microdomaines sont encore débattues : existent-ils (ils n'ont en effet jamais été observés directement et n'ont pu être mis en évidence que par des méthodes biochimiques invasives sujettes à caution) ? Sont-ils stables ? Quelle est leur distribution de taille et leur dynamique ? Confinent-ils les molécules et si oui, lesquelles et comment ?

Dans ce contexte tumultueux, j'ai proposé une nouvelle méthode expérimentale, permettant de détecter des domaines membranaires dans les cellules vivantes. Elle est fondée sur la spectroscopie de corrélation de fluorescence (FCS). Les efforts conjoints de notre équipe et celle de Didier Marguet du Centre d'Immunologie de Marseille Luminy (CIML) ont rendu possibles la démonstration et la mise en oeuvre de cette méthode sur des systèmes biologiques pertinents. J'ai co-encadré sur ce sujet la thèse de Laure Wawrezinieck, soutenue en septembre 2006.

2.2 La Spectrocopie de Corrélation de Fluorescence (FCS)

Alors que la plupart des études de diffusion membranaire ont été effectuées par mesure de retour de fluorescence après photoblanchiment (acronyme anglais FPR) et suivi de particules individuelles (SPT)[3], nous avons fait le choix d'utiliser la spectroscopie de corrélation de fluorescence (FCS). En FPR, les molécules retournant dans la région blanchie diffusent sur une surface au moins dix fois plus grande que cette

[3]Saxton MJ, Jacobson K : Single-particle tracking : applications to membrane dynamics. Annu. Rev. Biophys. Biomol. Struct. 1997, 26 :373-399.

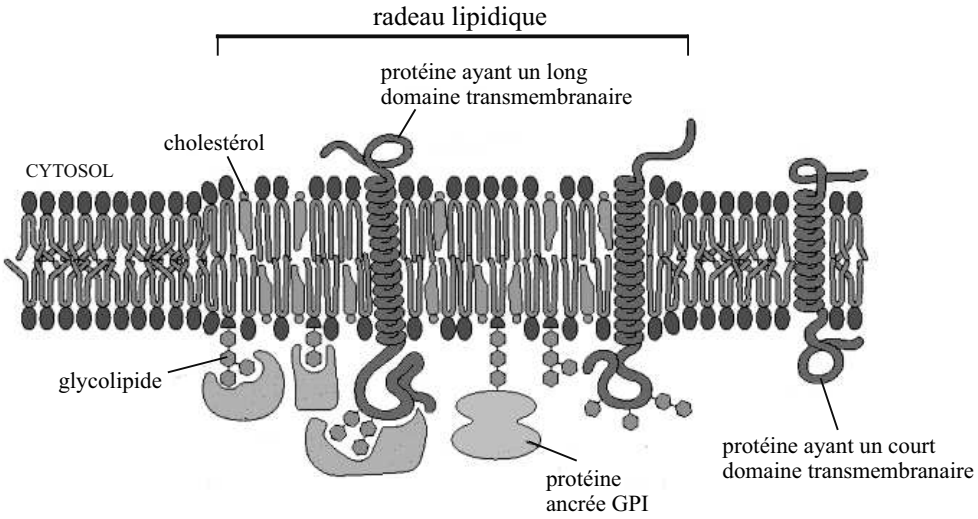

FIG. 2.2 – *Modèle de radeau lipidique selon Simons et Ikonen (d'après Alberts B, Lohnson A, Lewis J, Raff M, Roberts K, Walter P : Molecular Biology of the Cell. 4th ed. Garland Publishing, New York, 2002.). Dans ce modèle, les chaînes carbonées des sphingolipides sont majoritairement saturées et occupent moins d'espace latéral que leurs têtes hydrophiles ; les interstices sont comblés par des molécules de cholestérol. Ces agrégats serrés de sphingolipides et cholestérol formeraient des plateformes au sein de phases plus fluides composées de phospholipides insaturés*

dernière. Il est par conséquent difficile d'obtenir des informations sur des hétérogénéités sub-microniques. Le SPT offre une alternative puissante à la FPR en raison de sa haute résolution ($\sim$ 50 nm). Elle a été utilisée avec succès pour détecter des "corrals" (synonyme d'enclos) dus au cytosquelette sous-jacent à la membrane. Elle requiert cependant une analyse statistique souvent difficile. La FCS est une autre méthode utilisée pour mesurer la diffusion de molécules fluorescentes ; elle exploite les fluctuations de fluorescence produites par un petit nombre de molécules diffusant à travers un volume d'observation d'une fraction de femtolitre, défini par un montage de microscopie confocale (Figure 2.3).

Pour caractériser les fluctuations de fluorescence, on détermine la fonction d'autocorrélation temporelle de l'intensité de fluorescence qui permet d'extraire deux informations : le nombre moyen de molécules dans le volume d'observation (donc la concentration locale) et la mobilité des molécules. Pour une diffusion libre en deux dimensions, le temps de demi-décroissance de la fonction d'autocorrélation temporelle correspond au temps de diffusion de la molécule à travers le volume d'observation ; il est simplement relié au coefficient de diffusion D par $\tau_D = w_{xy}^2/(4D)$ où w désigne le waist transversal du faisceau laser focalisé.

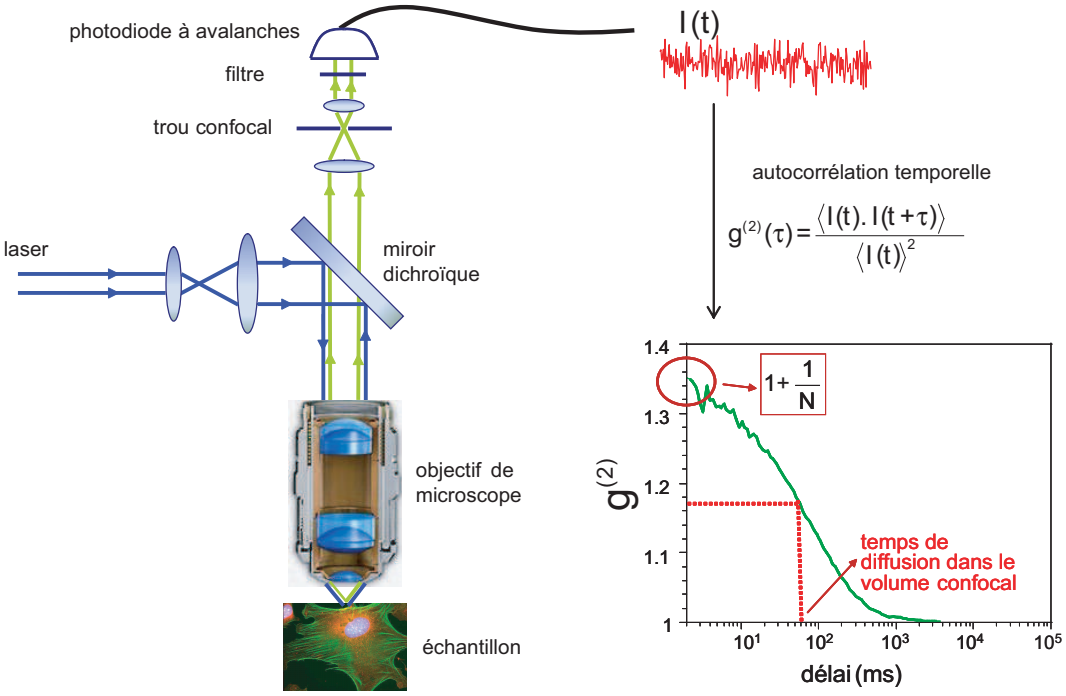

FIG. 2.3 – La spectroscopie par corrélation de fluorescence. *L'intensité fluorescence est collectée par un montage confocale et autocorrélée.*

2.3 Les lois de diffusion par FCS

La méthode, exposée dans l'article joint [17], repose sur la mesure du temps de diffusion d'une espèce moléculaire à différentes échelles spatiales. Dans le cas d'une diffusion brownienne en deux dimensions, le temps de diffusion est proportionnelle à la surface d'observation. Si la diffusion est perturbée, ce n'est plus nécessairement le cas et on peut mesurer des écarts à cette loi simple de diffusion. A partir de simulations Monte Carlo de diffusion, nous avons montré qu'il était possible de distinguer différents types d'organisation membranaire (réseau de barrières ou domaines de confinement isolés) à partir des lois de diffusion obtenues par FCS. Nos travaux ont été salués par une note de M. Saxton "New and Notable" dans Biophys. J. Nous avons revisité les questions controversées d'organisation membranaire en étudiant une grande variété de marqueurs membranaires [4]. Nous avons montré que les analogues fluorescents des sphingolipides et les protéines ancrées par un glycosylphosphatidylinositol (GPI) sont seulement confinés par des microdomaines d'origine lipidique. En revanche, le récepteur à la transférine est compartimenté à la fois par l'organisation lipidique et le réseau du cytosquelette. Nous confirmons ainsi l'existence d'une micro-architecture d'origine lipidique par des mesures sur cellules

vivantes.

Bien que les domaines soient plus petits que la limite de diffraction optique, ils modifient les lois de diffusion à des échelles spatiales plus grandes, ce qui permet de les détecter par FCS. Pour sonder les hétérogénéités membranaires, nous montrerons que des structures optiques sub-longueur d'onde permettent d'étudier plus directement sous la limite de diffraction optique les anomalies de la diffusion et peuvent révéler la structure "ultra-fine" des membranes (Cf chapitre 3).

Fluorescence Correlation Spectroscopy Diffusion Laws to Probe the Submicron Cell Membrane Organization

Laure Wawrezinieck,*† Hervé Rigneault,* Didier Marguet,† and Pierre-François Lenne*
*Institut Fresnel, MOSAIC Group, CNRS UMR 6133-Université Paul Cézanne Aix-Marseille III, Domaine Universitaire de Saint Jérôme, F-13397 Marseille Cedex 20, France; and †Centre d'Immunologie de Marseille-Luminy, MOSAIC group, CNRS UMR 6102-INSERM UMR 631-Université de la Méditerranée, Parc Scientifique de Luminy, Case 906, F-13288 Marseille Cedex 9, France

ABSTRACT To probe the complexity of the cell membrane organization and dynamics, it is important to obtain simple physical observables from experiments on live cells. Here we show that fluorescence correlation spectroscopy (FCS) measurements at different spatial scales enable distinguishing between different submicron confinement models. By plotting the diffusion time versus the transverse area of the confocal volume, we introduce the so-called FCS diffusion law, which is the key concept throughout this article. First, we report experimental FCS diffusion laws for two membrane constituents, which are respectively a putative raft marker and a cytoskeleton-hindered transmembrane protein. We find that these two constituents exhibit very distinct behaviors. To understand these results, we propose different models, which account for the diffusion of molecules either in a membrane comprising isolated microdomains or in a meshwork. By simulating FCS experiments for these two types of organization, we obtain FCS diffusion laws in agreement with our experimental observations. We also demonstrate that simple observables derived from these FCS diffusion laws are strongly related to confinement parameters such as the partition of molecules in microdomains and the average confinement time of molecules in a microdomain or a single mesh of a meshwork.

INTRODUCTION

The processes responsible for the molecular confinement in live cell plasma membranes have been widely investigated in the last past years. These studies have demonstrated the existence of different mechanisms that could be responsible for the confinement of lipids and proteins in the plasma membrane, such as the cytoskeleton, the molecular clustering, or the extracellular matrix (1). Among them, the actin cytoskeleton has been shown to be responsible for confining transmembrane proteins (2) as well as lipids (3). In this case, the actin filaments act as barriers that hinder the diffusion of membrane components. Beside this cytoskeleton confinement, models of the membrane structure have included lateral lipid heterogeneities, thereby enriching the fluid mosaic view initially proposed by Singer and Nicolson (4). Evidences for membrane domains come mainly from biochemical studies, which show that some membrane constituents are resistant to solubilization by nonionic detergents at low temperature (5). The remaining detergent resistant membranes are found to be enriched in cholesterol and sphingolipids. These results have led to a postulate for the organization of the plasma membrane in which cholesterol and sphingolipid-rich domains coexist with more fluid domains enriched in phospholipids with unsaturated hydrocarbon chains (6,7). Though increasing evidences that those domains exist, the data regarding their structure and dynamics are still very few and mainly indirect.

This lack of data principally results from the absence of appropriate tools. Indeed, optical tools such as confocal microscopy have not enabled the observation of separate domains and suggest that the size of the domains is below the optical resolution (<200 nm) (8). Alternative approaches, such as single-particle tracking (2,9,10) and optical tweezers (11), have a better spatial resolution and have shed a new light on this question. Single particle tracking and single dye tracking have proved to be valuable tools to measure the diffusion properties in membranes and to unravel hop diffusion. Nevertheless they suffer from two drawbacks: i), in most cases, these experiments require the labeling of a single molecule with a bead or a gold colloidal particle, which proves to be difficult; and ii), a large number of trajectories need to be recorded and analyzed to fit statistical criteria. One must be cautious in interpreting experimental results on a few diffusing particles, since distributions of hopping rates may be broad (12) and the detection of transiently confining structures thus requires the study of many molecules. In this respect, FCS may appear as a more appropriate technique since it analyzes an ensemble of molecules diffusing in the detection volume. Although FCS studies have reported anomalous diffusion in live cells (13), it has not been applied to study confinement in membranes. Here, we detail the rationales of the FCS analysis performed at various spatial scales to probe the submicron organization of the cell membrane. The method that we proposed recently (14) has been independently implemented in another context by Okamato's group (15,16).

Submitted June 3, 2005, and accepted for publication August 30, 2005.

Address reprint requests to Pierre-François Lenne, Institut Fresnel, MOSAIC Group, CNRS UMR 6133-Université Paul Cézanne Aix-Marseille III, Domaine Universitaire de Saint Jérôme, F-13397 Marseille Cedex 20, France. Tel: 33-491-28-8049; Fax: 33-491-28-8067; E-mail: lenne@fresnel.fr.

Abbreviations used: FCS, fluorescence correlation spectroscopy; ACF, autocorrelation function; GFP, green fluorescent protein; BODIPY, 4,4-difluoro-5,7-dimethyl-4-bora-3a, 4a-diaza-*s*-indacene; FL-G_{M1}, BODIPY-ganglioside G_{M1}; TfR, human transferrin receptor; RhG6, rhodamine 6G; FWHM, full width at half-maximum; 2D, two-dimensional.

0006-3495/05/12/4029/14 $2.00 doi: 10.1529/biophysj.105.067959

FCS is a mature and powerful technique for measuring diffusion coefficients and chemical reaction rates both in vivo and in vitro (17). It measures the spontaneous fluctuations of fluorescence in an open volume defined by a focused laser and confocal optics. These fluctuations can arise in particular from the diffusion of fluorescent molecules into or out of this open sampling volume. To analyze statistically the fluctuations, one computes the time ACF, which provides information on diffusion properties.

Though the size of the detection volume is diffraction limited, the ACF can be altered by processes occurring on smaller spatial scales. It has been recently shown (18,19) that confinement in small cell compartments modifies ACFs computed by FCS. In these studies, analytical formula taking into account the volume and geometry of confined regions are proposed to fit experimental ACFs. Although this approach might be useful to determine diffusion coefficients in small volume compartments, its validity is restricted to simple geometries and its implementation is difficult without any a priori knowledge of the geometry.

In this article, we suggest observables that can be obtained from FCS and that are useful to detect confinement in microdomains. First, we emphasize the problems encountered when fitting ACFs, and point out the need for measuring the so-called FCS diffusion laws, instead of only interpreting the shape of ACFs measured at a single size of waist.

The manuscript is organized as follows: we first introduce and show FCS experimental diffusion laws for a lipid and a transmembrane protein. The studied lipid is FL-G_{M1}, which is considered to be a raft marker, and the transmembrane protein is TfR-GFP, diffusion of which is supposed to be hindered by the cytoskeleton meshwork. Interestingly, these two constituents exhibit two different FCS diffusion laws. To explain these results, we simulate in the second part different diffusion processes, which could explain the FCS diffusion laws that have been measured experimentally. We first address the basic issue of confinement of a molecule freely diffusing in an impermeable or permeable 2D domain, and then focus on restricted diffusion in multiple microdomains in mosaic geometries. Two geometries are explored more accurately: the first one accounts for isolated microdomains, in which molecules can partition dynamically (''partitioning microdomains''); and the second accounts for the actin meshwork. Finally, the experimental FCS diffusion laws are reinterpreted thanks to the new light shed by the simulations.

MATERIALS AND METHODS:

A list of the parameters used in the following is given in Table 1.

Cell culture and staining

All experiments are carried out on COS-7 cells (American Type Culture Collection No. CRL-1657).

Fluorescent conjugated lipid probe BODIPY-ganglioside G_{M1} (FL-G_{M1}) (Molecular Probes, Eugene, OR) is incorporated in the plasma membrane by a lipid exchange procedure (20).

To obtain the TfR-GFP recombinant protein expression, cells are transiently transfected with a mixture of the plasmid and ExGen 500 reagent (Euromedex, Souffelweyersheim, France).

FCS measurements are performed at 37°C at least 16 h after each of these incorporations.

FCS setup

Confocal fluorescence microscopy and fluorescence correlation spectroscopy are performed on a custom apparatus, which has been developed from an Axiovert 200 inverted microscope (Zeiss, Jena, Germany). The excitation light of the 488 nm line of an Ar^+-ion laser is focused onto the sample through a Zeiss C-Apochromat 40×, numerical aperture =1.2, water immersion objective. The fluorescence is collected by the same objective, separated from the excitation light by a dichroic mirror, then split by a 50/50 cube splitter and sent onto two avalanche photodiodes through 525–565 nm bandpass filters. Cross correlation between the two channels is preferred to autocorrelation of one channel, since it reduces artifacts due to the dead time of each detector and after pulses. A confocal pinhole (20 or 50 μm in diameter) reduces the out-of-plane fluorescence. Precise positioning of the cell membrane in the confocal volume is obtained by moving the sample step-by-step with a three-axis piezo-scanner, which is controlled by a digital controller (Physik Instrumente, Karlsruhe, Germany). Scanning softwares are written with LabView (National Instruments, Austin, TX).

FCS measurements are performed by illuminating the sample with an excitation power of 3.5 μW at the back-aperture of the objective. Autocorrelation is processed by a hardware correlator (ALV-GmBH, Langen, Germany). Data are analyzed with built-in functions of IgorPro (Wavemetrics, Lake Oswego, OR).

Fitting of autocorrelation functions

In a standard FCS experiment, a diffusion measurement is carried out for a single size of the confocal volume, i.e., a single value of the laser beam transversal waist w at the focal plane of the focusing objective. The diffusion coefficient is determined from the measurement of the apparent diffusion time τ_d^{app} of a fluorescent molecule through the confocal volume, which is defined as the FWHM of the ACF. For free translational two-dimension diffusion, τ_d^{app} matches the actual diffusion time through the confocal volume $\tau_d^{\infty} = w^2/(4D_{micro})$, where D_{micro} is the microscopic diffusion coefficient of the fluorescent molecule in the plane of diffusion. If the diffusion is free, and in the case of a Gaussian approximation of the detectable emission intensity distribution, the ACF is given by (21)

$$g^{(2)}(\tau) = 1 + \frac{1}{N}\frac{1}{1+\frac{\tau}{\tau_d^{\infty}}}, \quad (1)$$

where N is the average number of molecules in the detection volume.

For anomalous diffusion, the mean-square displacement of particles is no longer proportional to time t as for free diffusion, but rather to t^{α}, with $0 < \alpha \leq 1$. This diffusion mode corresponds to molecules diffusing in the presence of multiple energy potential traps with binding energies that vary over wide ranges of time and space (22). Anomalous diffusion can also result from diffusion on a percolating cluster at the threshold. In FCS, if diffusion is anomalous, α can be determined from the ACF, which is given by

$$g^{(2)}(\tau) = \frac{1}{N}\frac{1}{1+\left(\frac{\tau}{\tau_{anomalous}}\right)^{\alpha}}, \quad (2)$$

where $\tau_{anomalous}$ is equal to τ_d^{app} if $\alpha = 1$.

When diffusion is free, then $\alpha = 1$. We will show in the Experimental Evidence section that the converse is false.

TABLE 1 Main parameters used in the simulations

Parameter description	Symbol	Value/Range of values/Calculation
Simulation parameters		
Time step	Δt_0	2.10^{-6}s
Simulation box	A	Square, 10×10 μm^2
Total simulated time		$> 4.10^3$ s
Half-size of the domains	r	Radius of a circular domain/Half-size of the side of a square domain. Varied between 50 nm and 100 nm.
Mean elementary jump length	σ	Between $r/100$ and $r/20$
Microscopic diffusion coefficient	D_{micro}	Between 1.0 and 10.0 μm^2/s
Waist of the excitation focal spot	w	Between 0 and 1 μm
Calculated parameters		
Apparent diffusion time	$\tau_{\text{d}}^{\text{app}}$	FWHM of the autocorrelation function
Free diffusion time in the focal spot	τ_{d}^{∞}	$w^2/(4D_{\text{micro}})$
Free diffusion time in a single domain	$\tau_{\text{d}}^{\text{domain}}$	$r^2/(4D_{\text{micro}})$ in a circular domain of radius r, $(1.122r)^2/(4D_{\text{micro}})$ in a square domain
Confinement time in a single domain	τ_{conf}	
Confinement strength	S_{conf}	$\tau_{\text{conf}}/\tau_{\text{d}}^{\text{domain}}$
Confinement size parameter	X_{c}	$\sqrt{(\text{Area of the focal spot})/\text{Area of the domain}}$
Specific parameters for isolated microdomains		
Density of the domains	d	(Total area of the domains)/Area of the simulation box
Microscopic diffusion coefficient inside the domains	$D_{\text{micro}}^{\text{in}}$	Between 1.0 and 5.0 μm^2/s
Microscopic diffusion coefficient outside of the domains	$D_{\text{micro}}^{\text{out}}$	$3\,D_{\text{micro}}^{\text{in}}$ (Dietrich et al. (29))
Probability of going into a domain	P_{in}	Between 0 and 1 (for $r/\sigma = 30$)
Probability of going out of a domain	P_{out}	Between 10^{-3} and 1 (for $r/\sigma = 30$)
Specific parameters for the meshwork		
Probability of crossing a barrier	P	Between 6.10^{-3} and 1 (for $r/\sigma = 5$)
Experimental outcomes		
Intercept time of the diffusion law in regime iii	t_0	
Effective diffusion coefficient	D_{eff}	
Partition of the molecules in microdomains	α	(Number of molecules in domains)/Total number of molecules

Size of the confocal volume

The size of the confocal volume can be controlled by selecting either with a diaphragm or a variable telescope (14,16) the lateral extension of the laser excitation beam falling onto the back-aperture of the microscope objective. Similar approaches have been implemented in fluorescence recovery after photobleaching experiments (23,24).

The size of the confocal volume can be inferred from the free diffusion time τ_{d}^{∞} of a fluorophore in the open confocal volume, and its known diffusion coefficient (Fig. 1). Here, Rh6G, of which the diffusion coefficient is known ($D_{\text{Rh6G}} = 2.8\,10^2$ μm^2/s) (21) is used to calibrate the size of the confocal volume. The radius of the illuminated observation area can be modulated between 190 and 400 nm. The Rh6G diffusion time through the confocal volume obtained by fulfilling the rear-aperture of the microscope objective allows the determination of the smallest waist accessible with our setup: w_{min}=190 nm. In all experiments, the excitation power at the back-aperture of the objective is kept constant for all waist sizes. To validate the calibration protocol of the waists in the context of 2D diffusion measurements, we have studied the diffusion of Bodipy-PC probes freely diffusing in giant unilamellar vesicles (14). We have checked that the determination of the diffusion coefficient is correct and independent on the size of the waist as expected for free 2D diffusion.

Simulations of confined diffusion and FCS

Scheme of simulations

We have implemented simulations as close as possible to real FCS experiments. We have included a fluorescent molecule in an area A, which is composed of a single domain or of multiple domains (Fig. 2). If not otherwise stated, the excitation laser beam is supposed to be Gaussian: $I(x, y) = I_0\exp(-2(x^2 + y^2)/w^2)$, where x and y are the Cartesian coordinates originating at the center of the area A. Depending on the objective back-aperture filling used, w can vary from 200 nm to 400 nm in a standard FCS setup.

The fluorescent molecule performs a random walk from a starting position that is randomly selected in the surface A. For the sake of simplicity and without any loss of generality, we simulate the walk of a single molecule. Simulating independent multiple molecules would not change the ACF profile but only its amplitude.

The random walk is performed as follows:

At each time step Δt_0, the particle performs a jump (ΔX, ΔY), which is determined by two independent random variables with a Gaussian distribution centered on 0 and a standard deviation $\sigma_{\text{x}} = \sigma_{\text{y}}$. The jump length $\Delta R = \sqrt{(\Delta X)^2 + (\Delta Y)^2}$ is therefore a random variable with a standard deviation $\sigma = \sqrt{2}\sigma_{\text{x}}$. The microscopic diffusion coefficient D_{micro} is related to σ by $D_{\text{micro}} = \sigma^2/(4\,\Delta t_0)$. Typically, 10^9–10^{10} steps are calculated for a trajectory. The mean elementary jump length is kept small (from 1/100 to 1/20) with respect to the size of domains (see below).

Detection and ACF

At each time step, the detected intensity is computed assuming a Poisson distribution; the number of detected fluorescence photons n_{ph} for a particle at position (x, y) is given by a random variable following a Poisson distribution function with parameter $\beta I(x, y)$, where β describes the collection efficiency of the setup (25). To analyze fluorescence fluctuations, the normalized time autocorrelation function ACF is defined as

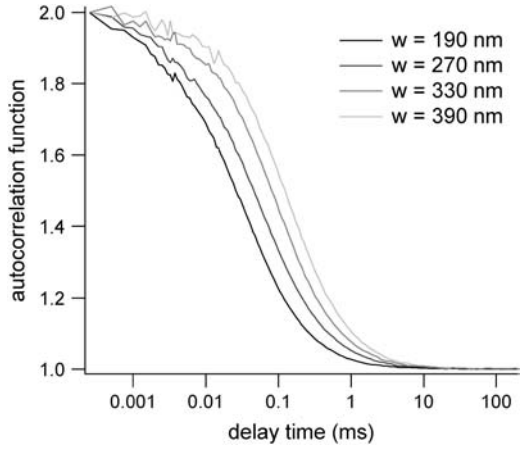

FIGURE 1 Rh6G autocorrelation functions measured by FCS at various beam waists w. The diffusion time is used to calibrate w.

$$g^{(2)}(\tau) = \frac{\langle n_{\mathrm{ph}}(t) n_{\mathrm{ph}}(t+\tau)\rangle}{\langle n_{\mathrm{ph}}(t)\rangle^2}, \tag{3}$$

where $\langle\ \rangle$ represents a time average.

In our simulations, the ACF is calculated either after the whole trajectory of the particle has been obtained or in parallel. The software correlator used to compute the ACFs follows the architecture proposed by (26) and described in (25). It has a logarithmic timescale, each channel having an individual sampling time and delay time.

Domains and barriers

Domains are considered to be regions in which the diffusion is free but restricted by barriers. These barriers can represent physical obstacles (cytoskeleton fences) or energy barriers (phase separations). Barriers are considered to be infinitely thin: they are lines that the molecule can cross with a given probability P. The probability P of crossing a barrier is independent of time. External boundaries of the surface A are impermeable. When the molecule hits the external boundaries, it is reflected at the wall.

When the molecule hits a barrier, a number *rand* is drawn at random between 0 and 1 and compared to the probability P of crossing the barrier. *rand* is generated by a number generator of Park and Miller with Bays-Durham shuffle and added safeguards, and has a period of $\sim 2 \times 10^9$ (27). If *rand* $< P$, the barrier is crossed; if not, the molecule remains at its previous position. This condition seems appropriate for biological membranes that are viscous.

Confinement in a permeable domain: definition of the confinement strength

This section aims at defining the input parameters and the associated physical parameters that are relevant to study the transient confinement in domains. In particular, we define the confinement time and the confinement strength, and give their expression as functions of the input parameters.

A circular permeable domain is now embedded in a square area. We define the confinement time τ_{conf} as the average time needed by a molecule placed at the center of the domain to escape from it. We have studied the ratio of the confinement time over the free diffusion time in the domain $\tau_{\mathrm{d}}^{\mathrm{domain}}$ as a function of P (Fig. 3).

Results can be approximated by a curve of the form:

$$\frac{\tau_{\mathrm{conf}}}{\tau_{\mathrm{d}}^{\mathrm{domain}}} = A + B\frac{\sigma}{r}\frac{1-P}{P}, \tag{4}$$

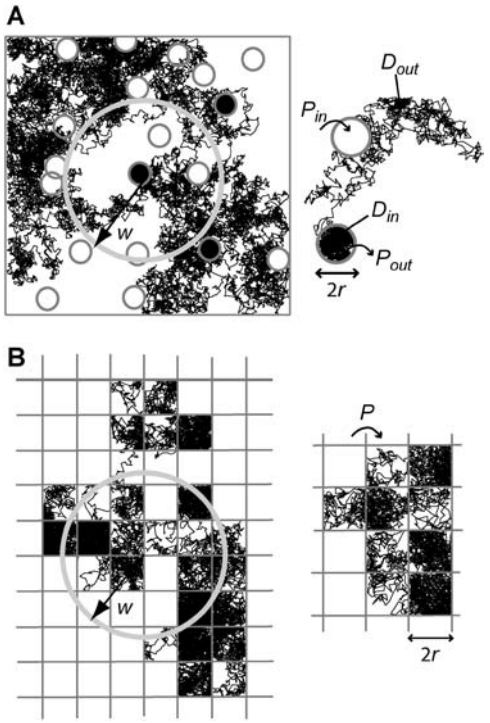

FIGURE 2 Simulated trajectories of a molecule in the cell membrane drawn for two models of confined diffusion. Fluorescence fluctuations arise from the detection volume of size w that is defined by a laser beam. In real optics, the diffraction limit sets in the minimum size w to $w_{\mathrm{min}} \sim 190$ nm. (*A*) Model for isolated microdomains: static circular microdomains of radius r are embedded in a fluid phase. The molecules have a Brownian motion as long as they stay in the same phase. The probabilities of going into and out of the microdomains, P_{in} and P_{out} respectively, can be asymmetric. Here, $r =$ 100 nm, $w = 600$ nm, $P_{\mathrm{in}} = 0.05$, and $P_{\mathrm{out}} = 0.02$. (*B*) Meshwork model: molecules have to jump over regularly spaced barriers. The molecules have a Brownian motion described by a microscopic diffusion coefficient D_{micro} as long as they stay within the same mesh. The probability that the molecule can cross the barrier is P. Here $r = 100$ nm, $w = 500$ nm, and $P = 0.05$.

where A and B are two positive constants: $A = 1$ (by definition) and $B = 0.95$ (fitted value).

This curve has the same shape as that derived by Saxton for the mean escape time from a corral (12). Nevertheless, different definitions for the escape time and the diffusion time were chosen in Saxton (12), which were more adapted to a single-particle tracking study, leading to different values for the two parameters A and B.

With our definition, parameter A is equal to 1, which means that the confinement time in a domain surrounded by fully permeable barriers is equal to the free diffusion time in the domain. When the probability P of crossing the barrier is <1, the confinement time gets longer than the diffusion time. The ratio $\tau_{\mathrm{conf}}/\tau_{\mathrm{d}}^{\mathrm{domain}}$ is the key parameter expressing the height of the barrier that molecules have to pass. In the following, we will define the confinement strength as $S_{\mathrm{conf}} = \tau_{\mathrm{conf}}/\tau_{\mathrm{d}}^{\mathrm{domain}}$. It has to be noted that this confinement strength is not only a function of P, but also a function of the mean diffusion step length σ and the radius r of the domain (see Eq. 4).

One may wonder if τ_{conf} is an accessible parameter, not only with single-particle analysis, but also from a FCS study. To assess this point, we simulate a FCS experiment with a laser spot centered on the permeable domain. The laser beam waist w is chosen equal to the radius r of the domain, so that the apparent diffusion time $\tau_{\mathrm{d}}^{\mathrm{app}}$ represents the average time spent by a molecule in the domain. In this case, we found that $\tau_{\mathrm{d}}^{\mathrm{app}}$ matches

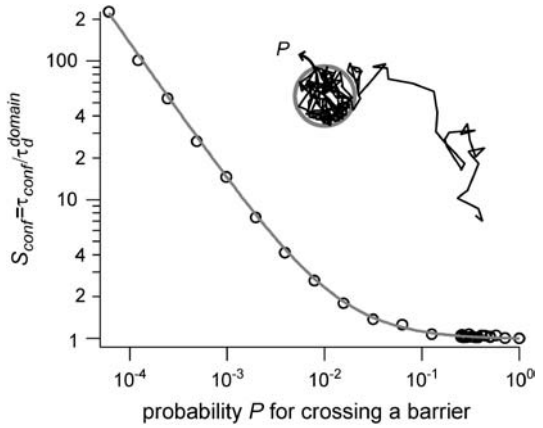

FIGURE 3 Confinement strength of a circular domain as a function of the probability P of crossing the barrier.

τ_{conf} as a function of P. As a result, τ_{conf} is still easy to determine with a FCS analysis.

In the case where the confinement area is a square, the value of the radius of the circle is simply replaced in Eq. 4 by the average length between the center of the square and the side of the square. This length is equal to $(4/\pi)\int_0^{\pi/4}(r/|\cos(\theta)|)d\theta = (4r/\pi)\ln(\sqrt{2}+1) = 1.1222r$, where θ is the angle that a line from the center of the square makes with one side. Doing the same analysis leads to coefficients $A = 1$ and $B = 1.34$.

Simulations and data analysis

We have implemented the simulations in C++ (Microsoft Visual C++, Version 6.0). They are run on a PC (Pentium III processor). Results have been analyzed and fitted with Igor Pro software (Wavemetrics).

EXPERIMENTAL EVIDENCE: NEED FOR FCS DIFFUSION LAW MEASUREMENTS

To connect our simulations to real experiments, FCS measurements at various spatial scales have been carried out for a lipid and a transmembrane protein inserted in the cell plasma membrane. The experimental results that are explained here have to be considered as a support to our theoretical considerations; they are representative of a large number of experimental results that have been carried out and that will be presented in details in P.-F. Lenne, L. Wawrezinieck, F. Conchonaud, O. Wurtz, A. Boned, H. Rigneault, and D. Marguet (unpublished).

This section points out the need for performing FCS diffusion law measurements, instead of the sole study of the shape of the autocorrelation function at a single waist.

Experimental autocorrelation functions

Confocal images of COS-7 cells after staining with fluorescent lipids FL-G_{M1} showed a uniform distribution of the probes in the plasma membrane and a vesicular staining figured by intracellular small dots (Fig. 4 *A*). Confocal images for TfR-GFP expressing cells (Fig. 4 *B*) show comparable intracellular and membrane fluorescence signal distribution.

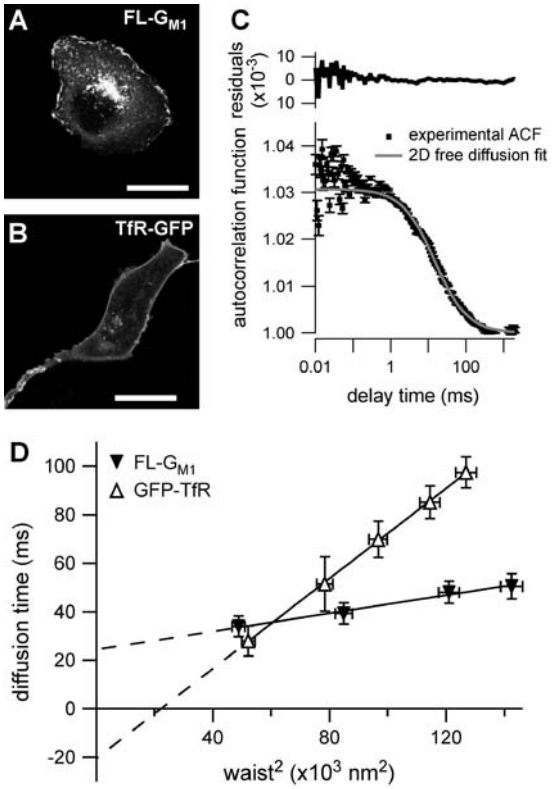

FIGURE 4 Experimental results on COS-7 cells for FL-G_{M1} and TfR-GFP. (*A*) Confocal image of a cell stained with FL-G_{M1} (scale bar, 20 μm). (*B*) Confocal image of a TfR-GFP stained cell (scale bar, 20 μm). (*C*) ACF measured by FCS on FL-G_{M1} stained cells. (*D*) Experimental FCS diffusion laws obtained for FL-G_{M1} and TfR-GFP. Curves are extrapolated to zero beam waist to make the time intercepts more visible, even if the diffusion law at small waists can be different.

Fig. 4 *C* shows the experimental ACF obtained for FL-G_{M1} diffusing in the plasma membrane of COS-7 cells. In this case, fitting the experimental ACF with an anomalous fit leads to an anomalous diffusion coefficient $\alpha \approx 1$. The studied diffusion is therefore not anomalous, which means that the potential trap energies do not vary over a wide range of time and space. Nevertheless, the diffusion of lipids at the cell membrane is certainly constrained, since the measured diffusion time is $\sim$10 times longer than the diffusion time of lipids in an artificial membrane (28).

This example shows that fitting the ACF obtained with fluorescent lipids diffusing in the plasma membrane does not permit determination of their diffusion mode. On the contrary, measuring the diffusion time at different sizes of the confocal volume is an interesting way of studying the confinement.

Experimental FCS diffusion law

For an experimentalist, it is possible to vary the waist w by changing the extension of the laser beam falling on the

microscope objective back-aperture. We name ''FCS diffusion law'' the plot of the apparent diffusion time τ_d^{app} of a membrane component measured by FCS as a function of the square of the waist $w^2\tau_d^{app}$ is defined as the FWHM of the ACF. We will show that this representation is very fruitful to study the constrained submicron diffusion in the cell membrane.

Although the 1-species free 2D diffusion curve seems to fit nicely the experimental ACFs obtained for FL-G_{M1} and TfR-GFP, the FCS diffusion laws do not reflect free diffusion. Indeed, in both cases the diffusion time is not proportional to the square of the waist w^2 as it is expected for free diffusion, where $\tau_d^{\infty} = w^2/(4D_{micro})$, but is an affine function of w^2 ($\tau_d^{app} = t_0 + bw^2$, with $t_0 \neq 0$). The intersection of the line with the time axis is strictly positive in the case of FL-G_{M1} ($t_0 = 25 \pm 3$ ms), and strictly negative in the case of TfR-GFP ($t_0 = -20 \pm 2$ ms) (Fig. 4 *D*). Knowing that G_{M1} is a putative raft marker and that TfR could be sensitive to the cytoskeleton through its cytoplasmic tail, these two different FCS diffusion laws may be signatures for two different diffusion processes.

For diffusive processes, it is expected to have a zero diffusion time at zero beam waist. However, the extrapolation of the experimental diffusion curve to zero beam waist can be nonzero independently of the real value of the diffusion time. In the next core section of this study, we will try to explain the two different intercepts and slopes of the measured diffusion laws with two models for the diffusion of membrane constituents. We will also show that these experimental results (free-like ACFs, but FCS diffusion laws that are not normal) are not paradoxical but can indeed reflect diffusion processes in a submicron structured membrane.

SIMULATION RESULTS

To explain the two experimental behaviors that we have shown in the first section, we propose and test different models. First, we give a simple example of total confinement in which a molecule is enclosed in an impermeable box. Then we propose two more refined models to account for i), the diffusion of molecules transiently sequestered in lipid microdomains and ii), the diffusion of molecules hindered by the cytoskeleton meshwork.

Simulated confinement in one impermeable domain

The purpose of this study is to determine how the diffusion behavior of a molecule (as measured by FCS) is sensitive to the presence of impermeable barriers. Moreover, this is useful in determining the minimum size of the simulation area which prevents FCS measurements from boundary effects.

Let us first analyze how ACFs are changed by the confinement of molecules in a single domain with impermeable barriers. We assume a circular domain on the center of which a laser beam is focused. The domain has a radius r and the waist of the laser beam is w. The key parameter is $X_c = w/r$, which reflects the confinement probed by the laser beam. Fig. 5 *A* shows autocorrelation functions obtained for different values of r and a fixed value of w. The microscopic diffusion coefficient D_{micro} is kept the same in all these simulations: $D_{micro} = 10.0\,\mu m^2 s^{-1}$, $w = 250$ nm, and thus $\tau_d^{\infty} = 1.56$ ms. Fig. 5 *A* clearly shows that the so-called apparent diffusion time τ_d^{app} (FWHM of the ACF) does not generally match the free diffusion time τ_d^{∞} and depends strongly on the confinement: it decreases when the size of the domain decreases. The decrease of τ_d^{app} is a direct consequence of the reduction of the area available for diffusion, which is not defined anymore by the laser beam extension. In the presence of confinement, a diffusion measurement using FCS should not be made at a single value of the waist, since the diffusion law is not that of free diffusion: it leads practically to an overestimation of D_{micro} when estimated by $D_{micro} = D_{app} = w^2/(4\tau_d^{app})$.

Let us thus assume now that the diffusion law is probed by varying w while the domain size is kept constant. Fig. 5 *B* shows the variation of τ_d^{app}, with $X_c^2 = w^2/r^2$. Three different regimes are observed. For $X_c^2 < 0.1$, τ_d^{app} increases linearly with X_c^2 as predicted for free diffusion. For intermediate values, $0.1 < X_c^2 < 1$, τ_d^{app} increases more slowly with X_c^2 and

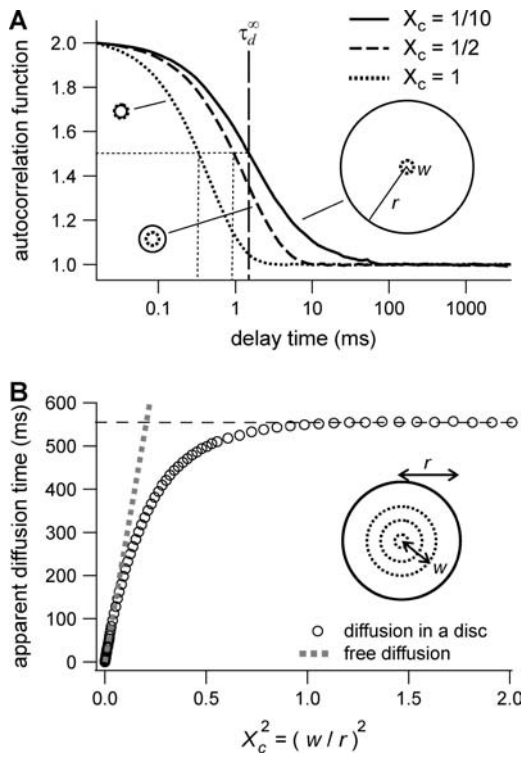

FIGURE 5 Simulation results for a molecule diffusing in a single impermeable domain. (*A*) ACFs obtained by FCS. Effect of the domain size on the shape of ACFs drawn for three values of the confinement parameter $X_c = w/r$. (*B*) Apparent diffusion time measured from ACFs as a function of the confinement parameter squared, plotted for a fixed size of the impermeable domain.

deviates from the standard formula. For $X_c^2 > 1$, τ_d^{app} reaches a saturation value. This regime is dominated by a domain size effect: as a further proof, we have verified that the saturation value of τ_d^{app} is proportional to r^2 (data not shown).

It has to be noted that these conclusions can be extended to the case of a square domain of side $2r$. The confinement probed by the laser beam is then defined by $X_c = (\pi/4)^{1/2} w/r$. The proportional coefficient $(\pi/4)^{1/2}$ is chosen so that X_c^2 is still the ratio of the excitation beam surface area (πw^2) over the confinement area ($4r^2$). Here again, the free diffusion regime is only obtained when $X_c^2 < 0.1$.

The shape of the ACF has already been studied in the case of a square domain in Gennerich and Schild (19).

Simulated confinement in multiple microdomains

In the following, we will distinguish between two hindering processes, and propose a model for both of them. First, we will focus our study on isolated circular microdomains, which try to account for lipid microdomains. Then we will study the diffusion of molecules in a meshwork, which is supposed to model the cytoskeleton.

Isolated microdomains

We have modeled rafts as permeable isolated microdomains surrounded by energy barriers. This model should be able to account for lipid rafts as well as other kinds of domains. We have simulated the diffusion of a molecule in a model membrane where microdomains (phase II) are embedded in a larger square surface of phase I (Fig. 2 *A*). Microdomains are considered as static entities that are separated from phase I by barriers. They can be either periodically or randomly distributed. We assume that domains are identical disks of radius r distributed over the surface. We make the assumption that the microscopic diffusion coefficients in and out of microdomains, respectively D_{micro}^{in} and D_{micro}^{out}, are linked by $D_{micro}^{out} = 3\,D_{micro}^{in}$, as it has been previously measured on artificial membranes (29). D_{micro}^{in} and D_{micro}^{out} stand for the microscopic diffusion coefficients in liquid-ordered and liquid-disordered phases, respectively. In each simulation, the following parameters are chosen: the microscopic diffusion coefficient outside of the domains is $D_{micro}^{out} = 3.125\ \mu m^2 s^{-1}$, and the mean jump length is $\sigma = 5$ nm. The size of the radius of the circular domain is $r = 100$ nm, and the square simulation box A has an area of 100 μm^2.

Probabilities of going out of or into a microdomain are P_{in} and P_{out}, respectively. If not otherwise stated, these two probabilities have the same value, P. The confinement probed by the laser beam is defined here by $X_c = w/r$. In the following, σ/r is kept constant, so that the confinement strength $S_{conf} = \tau_{conf}/\tau_d^{domain}$ is only a function of the probability P.

Shapes of ACFs obtained for different probabilities P of crossing a barrier. Fig. 6 *A* shows ACFs which have been obtained for different probabilities of crossing the barriers

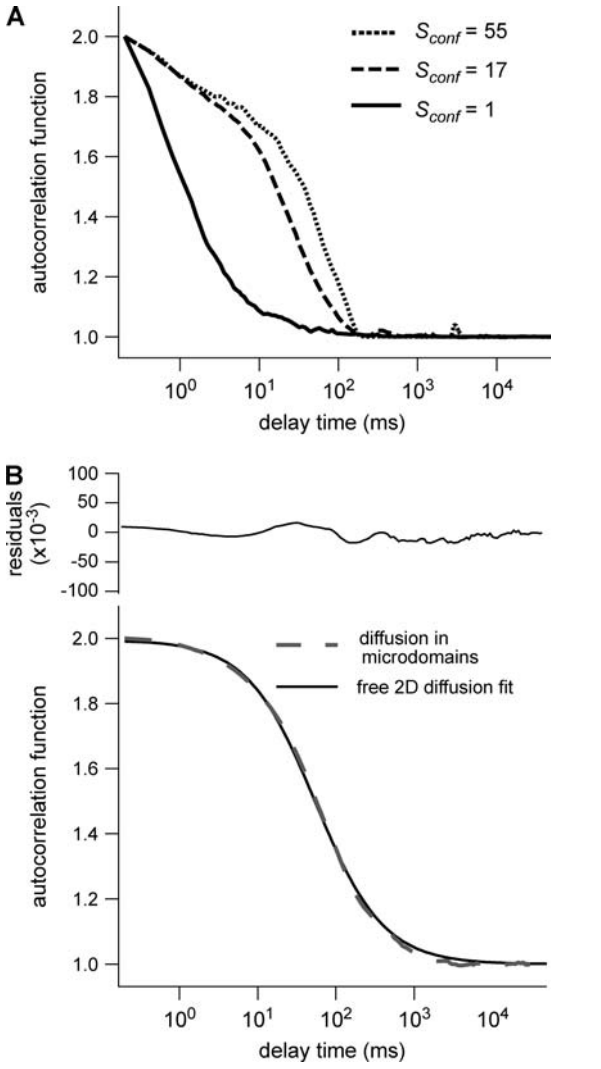

FIGURE 6 Simulated intensity ACFs for a single molecule diffusing in microdomains delimited by permeable barriers. (*A*) ACFs are calculated for a confinement parameter $X_c^2 = 1$ and for different probabilities P of crossing the barriers. (*B*) ACF calculated for a confinement parameter $X_c^2 = 16$. It is well fitted by a free 2D diffusion fit.

and for $w = r$, for a laser spot centered on a domain. When P decreases, i.e., when barriers are more impermeable and the confinement strength S_{conf} increases, the diffusion time increases. Two distinct decay times can be observed for high values of S_{conf} and small values of X_c^2: the short time is related to the diffusion time within a single domain and the longer one is related to the diffusion time through the whole illuminated area. The detection of the first bump is a signature of the presence of a domain that can be on the order of or even smaller (data not shown) than the beam extension (30).

On the contrary, ACFs obtained for large waists ($X_c^2 > 10$) can be quite nicely fitted by a 1-species 2D free diffusion fit (Fig. 6 *B*).

We put forward τ_d^{app} as an observable of physical meaning that is easy to determine since it does not require the

implementation of a complex fit. By varying w, we can explore FCS diffusion laws by observing τ_d^{app}. It is simply related in the case of free 2D diffusion to the microscopic diffusion coefficient by $\tau_d^{app} = \tau_d^{\infty} = w^2/(4D_{micro})$. In the presence of microdomains, we expect a deviation from this law depending in particular on S_{conf} and on the size and density of microdomains.

Diffusion laws for fixed size and density of domains and variable probability P of crossing a barrier. To evaluate the different regimes that a FCS experiment can probe, we have determined the variation of the apparent diffusion time with respect to w (having r fixed). We first plot τ_d^{app} as a function of X_c^2 with the laser spot centered on a microdomain, a density of microdomains $d = 0.5$ and different confinement strengths $S_{conf} \in \{1, 2, 4, 6, 15\}$ (Fig. 7 *A*). When $S_{conf} > 1$, i.e., when the diffusion is not free, three regimes can be distinguished. If $X_c^2 \leq 0.1$, particles appear to diffuse freely, and D_{app} matches D_{micro}^{in} (regime i): FCS measurements probe the microscopic diffusion coefficient within the microdomain. A transient regime is observed when $X_c^2 \approx 1$: complex diffusion occurs because of barrier effects (regime ii). Last, when $X_c^2 \geq 10$, τ_d^{app} scales linearly with w^2 (regime iii). However, it differs significantly from regime i: the intersection with the time axis becomes strictly positive and the line slope increases. The positive intercept as well as the slope are increasing functions of the probability S_{conf}.

To be closer to experimental conditions, one averages the values of τ_d^{app} obtained for different positions of the laser spot on the surface of the membrane. Fig. 7 *B* shows the average value $\overline{\tau_d^{app}}$ as an affine function of X_c^2. The first two regimes, i and ii, cannot be distinguished anymore. When $X_c^2 > 10$, $\overline{\tau_d^{app}}$ is a linear function of w^2. We find that regime iii is described by the same line as the one obtained when no average is done on the position of the laser waist. In the following, all the diffusion laws will be given with the laser spot centered on one domain. This leads to no change in the description of regime iii, which is the regime we are mostly interested in, since we expect to have $w/r >$ few units in experiments. If the sole regime iii is indeed probed experimentally, an upper limit can be given to the microdomain radius since this regime starts at $X_c^2 > 10$.

We also verified that the same regime iii is obtained for periodically and nonperiodically distributed microdomains as long as there is no percolation (data not shown).

Diffusion laws for a fixed size of domains, a fixed probability P of crossing a barrier and various densities of domains. The same study is carried out for densities ranging from 0.1 to the percolation threshold, with a periodical distribution of microdomains.

Fig. 8 *A* shows that the intercept and the slope of the line describing regime iii are increasing functions of the density d.

Diffusion laws for fixed size and densities of domains and different probabilities P_{in} and P_{out} of entering and exiting a domain. In the following, the study is carried out with $r/\sigma = 30$.

The probability of entering a microdomain may not be the same as the probability of exiting the microdomain. To study this case, the diffusion laws have first been drawn for a fixed probability $P_{out} = 0.005$ and a variable value of P_{in} (Fig. 8 *B*).

Regime iii are lines, whatever the value of P_{in} is. The intercepts and the slopes are two increasing functions of P_{in}. They behave as power laws of P_{in}.

The diffusion laws have also been drawn for a fixed probability $P_{in} = 0.005$ and a variable value of P_{out} (Fig. 8 *C*). In this case, regime iii is still a line, the intercepts and the slopes being decreasing functions of P_{out}. It can be pointed out that the different simulated diffusion laws obtained for high values of P_{out} ($P_{out} \geq 0.05$) are approximately the same. These high values of P_{out} lead to a confinement time on the order of the diffusion time in a domain ($S_{conf} = \tau_{conf}/\tau_d^{domain} \approx 1$). These cases correspond to a low confinement of the molecules in the domain, whereas the probability of

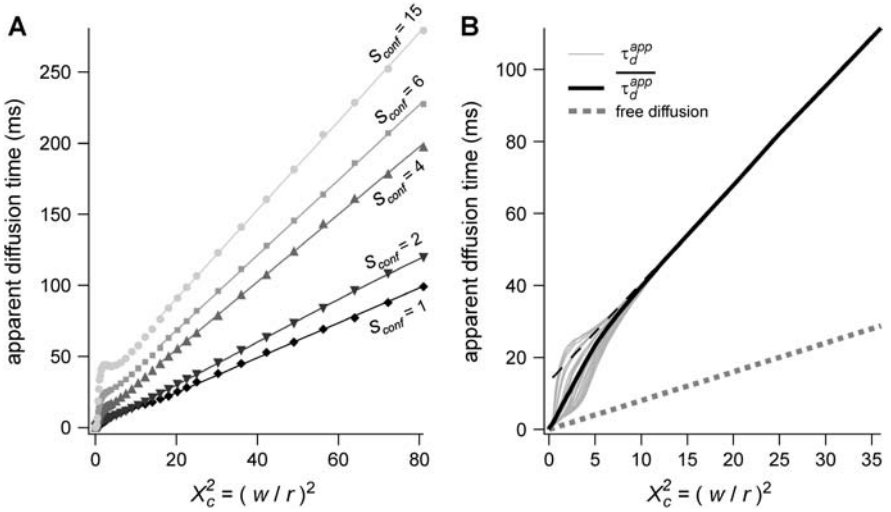

FIGURE 7 Simulated diffusion laws obtained by FCS: the apparent diffusion time measured from ACFs is plotted as a function of the confinement parameter squared X_c^2. In each case, the chosen probabilities P_{in} and P_{out} are equal. (*A*) Diffusion laws obtained for five confinement strengths S_{conf}. Here the laser spot is centered on a microdomain. (*B*) The diffusion law is averaged on all possible positions of the excitation beam for $S_{conf} = 6$. It is compared to diffusion laws plotted for different positions of the laser spot.

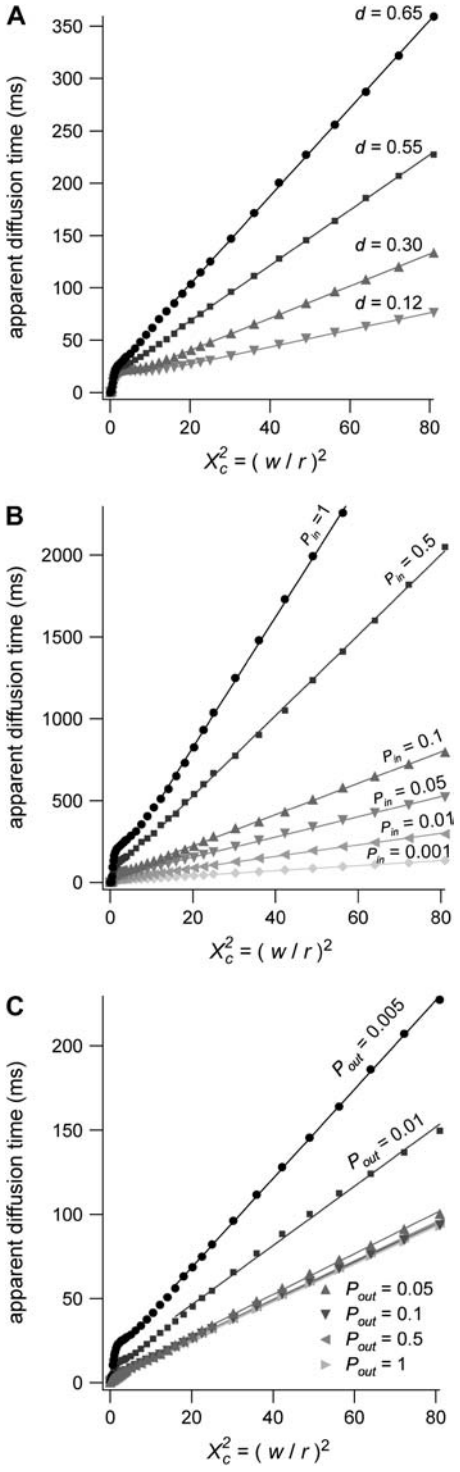

FIGURE 8 Simulated diffusion laws obtained by FCS for the microdomain geometry, when d, P_{in}, or P_{out} are changed. (*A*) Diffusion laws as a function of the density of microdomains (i.e., as a function of the ratio of the surface of all microdomains over the whole surface *A*) for $P_{in} = P_{out} = 0.05$. (*B*) Diffusion laws obtained for different probabilities of going P_{in} into microdomains (for $P_{out} = 0.05$). (*C*) Diffusion laws obtained for different probabilities P_{out} of going out of microdomains (for $P_{in} = 0.05$).

entering a domain is low: the diffusion law is very close to the one obtained for impermeable obstacles.

Regime iii of the diffusion laws is a line for densities of microdomains ranging from 0.1 to 0.65, and when $0 \leq P_{in} \leq 1$, $0.001 \leq P_{out} \leq 1$, for $r/\sigma = 30$ (which corresponds to confinement strengths ranging from 1 to 15).

Meshwork

We will now show that the diffusion law is different when the molecule diffusion is hindered by a meshwork instead of isolated microdomains. We consider the case of multiple adjacent domains separated by barriers (Fig. 2 *B*). This situation may be representative of the diffusion of transmembrane proteins in a cytoskeletal network (e.g., the actin meshwork in COS-7 cells).

For reasons of simplicity, domains are squares separated by straight barriers spaced by a distance of $2r$. In each simulation, the following parameters are chosen: the microscopic diffusion coefficient is $D_{micro} = 3.125\,\mu m^2 s^{-1}$, the jump length $\sigma = 5$ nm, and the size of the half-side of the squares $r = 100$ nm.

The confinement probed by the laser beam is defined here by $X_c = (\pi/4)^{1/2} w/r$, with the laser beam centered on a knot of the meshwork.

Fixed size of confinement and variable probability P of crossing the barrier. Fig. 9 *A* shows ACFs obtained for a fixed illumination laser waist and for different values of S_{conf}, corresponding to different values of P, since σ/r is kept constant.

As for isolated microdomains, the apparent diffusion time increases when P decreases, and two decay times are obtained for large confinement strengths and small values of X_c ($X_c^2 \approx$ few units, depending on the confinement strength). Moreover, ACFs obtained for large waists ($X_c^2 >$ few units) are well fitted by a 1-species 2D free-diffusion fit (Fig. 9 *B*). As in the case of isolated microdomains, study of the shape of the ACF does not give any information on the diffusion mode if the area of the focal spot is more than a few times larger than the area of a single mesh.

Apparent diffusion time when w varies. Fig. 10 *A* shows τ_d^{app} as a function of X_c^2 for different values of S_{conf} : $S_{conf} \in \{1, 4, 17, 55\}$. As expected, τ_d^{app} matches τ_d^{∞} when $X_c^2 < 2$. For intermediate values of X_c^2, i.e., $X_c^2 \approx 2$, a short transition regime is observed. When $X_c^2 > 2$, τ_d^{app} is a linear function of X_c^2: its slope is dependent on S_{conf} and the intersection with the time axis is negative. The slope and the absolute value of the intersection with the time axis are two increasing functions of the confinement strength S_{conf}. Fig. 10 *B* shows the average value $\overline{\tau_d^{app}}$ as a function of X_c^2 for $S_{conf} = 7$. The first two regimes i and ii cannot be distinguished anymore in the case of isolated microdomains. When $X_c^2 > 5$, $\overline{\tau_d^{app}}$ is the same linear function of w^2 as the one obtained when no average is done on the position of the laser waist.

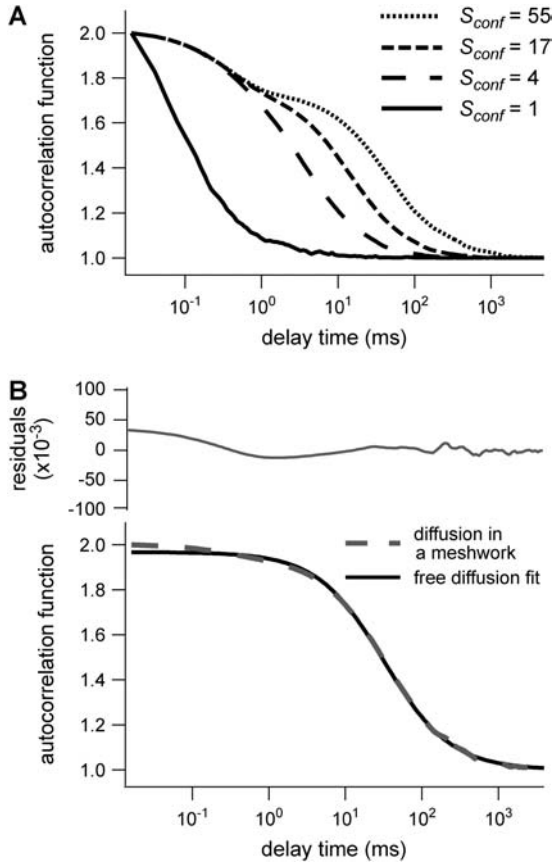

FIGURE 9 Simulated results obtained by FCS for permeable meshwork geometry. (*A*) ACFs are calculated for a confinement parameter $X_c^2 = 4$ and for different probabilities P of crossing the barriers. Effect of the confinement strength on the shape of ACFs. (*B*) ACF calculated for a confinement parameter $X_c^2 = 16$. It is well fitted by a 2D free diffusion fit.

DISCUSSION

The major applications of FCS are measurements of diffusion coefficients D (31,32). For free diffusion, the standard treatment of FCS data, which consists in fitting ACFs measured at a single size of the waist, is well adapted to determine D. However, a large number of membrane proteins and lipids are partially confined in substructures of sizes ranging from tens of nanometers to micrometers; some are impeded by the cytoskeleton, some others are thought to be raft-associated (33,34). Although sophisticated fits can give some clues on the mode of diffusion in some specific cases, we have shown here that the FCS approach can be revisited to understand diffusion in membranes and to allow inferences on membrane structures. We have introduced the ''FCS diffusion law'' concept that requires performing several FCS measurements for different sizes of the observation volume, a parameter defined by the transverse laser waist w and can be easily changed in a FCS setup by underfilling the microscope objective back-aperture. With such a technique, we have easily performed measurements for waists w ranging from 200 nm to 400 nm, which corresponds to a fourfold increase of X_c^2.

The determination of the apparent diffusion time τ_d^{app} for different values of w permits one to infer the process of diffusion; in particular, we emphasize that τ_d^{app} can bring information on the confinement. Fig. 11 summarizes our different results and is presented as a guide for discussion.

When the size of w is small with respect to the domain size ($X_c^2 \leq 0.1$ (regime i)), the diffusion appears to be free: the size of the beam does not permit probing the complexity of the system (either skeletal corrals or isolated microdomains). On the other hand, FCS can then give access to microscopic diffusion coefficients and will be sensitive to heterogeneities: it can be used to determine a two-dimension map of microscopic diffusion coefficients. For laser waists comparable to the size of the domains ($X_c^2 \approx 1$ (regime ii)), a transitional diffusion regime is observed. In this regime and for a small probability of crossing the barriers, we expect to detect confinement by a noticeable change of ACFs, which exhibit two different decay times associated respectively to diffusion through the domain and the observation volume (see Figs. 6 *A* and 9 *A*). For laser waists larger than the size of the domains ($X_c^2 > 10$ for isolated domains and $X_c^2 > 2$ for a meshwork (regime iii)), diffusion is normal again, with an apparent diffusion coefficient D_{eff} depending on the probability of crossing the barriers, the microscopic diffusion coefficients, and the density of domains (in the case of isolated microdomains). This regime can be approximated by a function of the form

$$\tau_d^{app} = t_0 + \frac{1}{4D_{eff}} w^2, \quad (5)$$

where t_0 and D_{eff} are two constants. Interestingly, in simulations, t_0 is positive for diffusion in isolated microdomains and negative for corrals.

Phenomenological models for the regime iii of the FCS diffusion law obtained in rafts and corrals

Regime iii is of particular interest since it corresponds to the experimental case when the size of the microdomains is a few times smaller than the diffraction limit. In this section, we focus on the interpretation of parameters t_0 and D_{eff} (Eq. 5) that are easily deduced from the FCS diffusion laws in this regime.

Diffusion laws in microdomains as a function of the molecular partition inside microdomains

We have shown that the intercept t_0 and the slope $1/(4D_{eff})$ of these lines depend on parameters such as the density and the probabilities of entering or exiting microdomains. They also depend on the diffusion coefficients inside and outside microdomains.

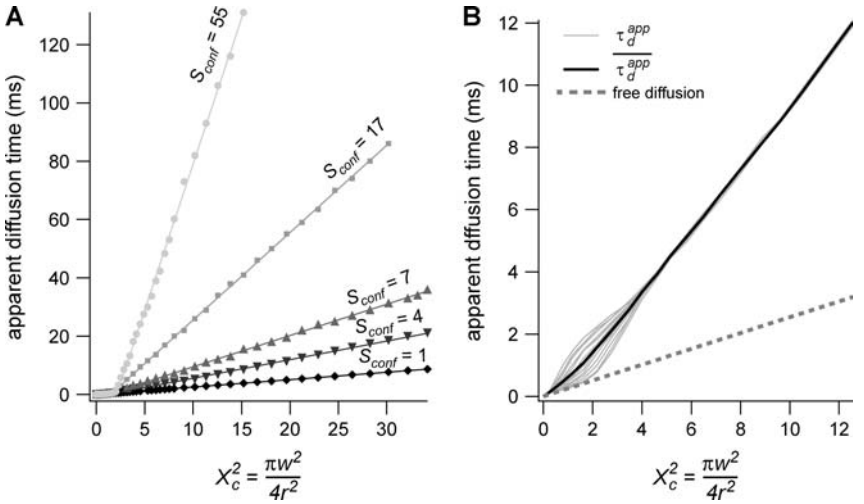

FIGURE 10 (*A*) Diffusion laws obtained for five confinement strengths S_{conf}, and a single position of the excitation beam (the laser spot is centered on a knot of the meshwork). (*B*) The diffusion law is averaged on all possible positions of the excitation beam (for $S_{\text{conf}} = 7$). It is compared to diffusion laws plotted for different positions of the laser spot.

Nevertheless, more physical parameters are needed to explain the experimental FCS diffusion laws.

The partition coefficient α of molecules into raft microdomains can be evaluated independently through biochemical studies. The partition coefficient α corresponds to the ratio measured at a given instant of molecules of a certain kind that are inside microdomains over all molecules of this kind. It can also be calculated with our simulations, since the duration of the whole simulated trajectory is much longer than the time needed for the molecule to visit all the allowed points of the state-space (ergodic principle). Hence, α is obtained from the simulated trajectory by calculating the time the molecule spends in microdomains over the whole simulation time.

In the Appendix, we show that the time intercept t_0 can be quite well described by a function of α and the confinement time

$$t_0 \approx 2\alpha(\tau_{\text{conf}} - \tau_{\text{d}}^{\text{domain}}). \tag{6}$$

Since α can be measured from biochemical studies, one can now evaluate the confinement time in a single microdomain τ_{conf} under the usually admitted assumption that $\tau_{\text{conf}} \gg \tau_{\text{d}}^{\text{domain}}$.

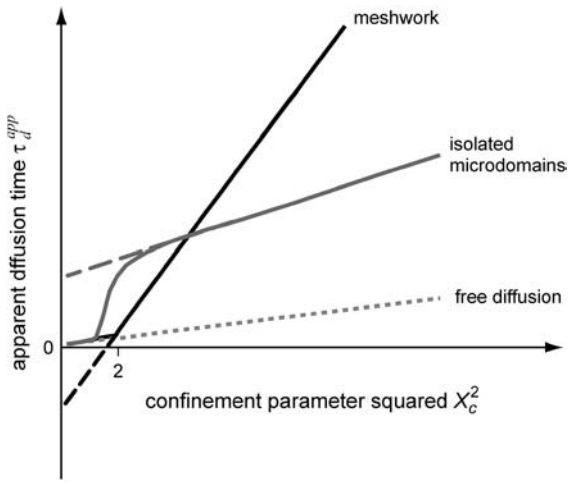

FIGURE 11 Apparent diffusion time with respect to X_c^2 for different geometries of diffusion.

To go further, we give now a possible expression for the slope $1/(4D_{\text{eff}})$ of the line describing the regime iii: the total time needed by a molecule to diffuse through the focal spot is the sum of the time it is confined in microdomains and t_{free} the time it is not being confined. In this case, one can write $\tau_{\text{d}}^{\text{app}} = N\tau_{\text{conf}} + t_{\text{free}}$, with N the average number of domains that are being crossed.

But as mentioned before, the partition is defined (in the time description) by the time a molecule spends in microdomains over the total diffusion time, which can be written as $\alpha = N\tau_{\text{conf}}/\tau_{\text{d}}^{\text{app}}$.

This leads to $\tau_{\text{d}}^{\text{app}} = t_{\text{free}}/(1-\alpha)$, which is equivalent to $D_{\text{eff}} = (1-\alpha)D_{\text{free}}$ in terms of diffusion coefficients.

If molecules enter easily in microdomains, which is the case if the partition is $\sim>0.5$, D_{free} is equal to D_{out}. If molecules do not enter easily in microdomains, which is the case if the partition is $\sim<0.5$, they diffuse among microdomains as if they were impermeable obstacles and D_{free} is equal to D_{obst}, which is the effective diffusion coefficient among impermeable obstacles. An expression of D_{obst} in terms of the surface density covered by the obstacles is given in the Appendix.

As a consequence, this leads to the following expression for the effective diffusion coefficient in the presence of permeable microdomains:

$$D_{\text{eff}} = \begin{cases} (1-\alpha)D_{\text{obst}} & \text{if } \alpha < 0.5 \\ (1-\alpha)D_{\text{out}} & \text{if } \alpha > 0.5 \end{cases} \tag{7}$$

Diffusion laws in a meshwork as a function of the confinement strength

In all diffusion simulations in a meshwork, the particle visits a certain number of meshes during its diffusion in the confocal volume. The average number N of meshes that are

crossed is only a function of the waist of the focal spot, not of the probability of passing a barrier. The mean diffusion time through the focal spot is equal to the number of crossed meshes multiplied by the confinement time in a single mesh so that $\tau_d^{app} = N\tau_{conf} = NS_{conf}\tau_d^{domain}$. In the case of free diffusion, the diffusion time in the focal spot is given by the number of crossed meshes multiplied by the diffusion time in a single mesh: $\tau_d^{\infty} = N\tau_d^{domain} = w^2/(4D_{micro})$. As a consequence, the asymptotic diffusion law needs to be a line with a slope equal to $S_{conf}/4D_{micro}$. For spatial scales much smaller than the mesh size, one expects to obtain a free diffusion law, i.e., a line with a slope equal to $1/4D_{micro}$. Finally, the spatial scale at which regime ii and regime iii cross should be close to the mesh size. It can be seen from the simulated FCS diffusion laws that the crossover is found for $X_c^2 \approx 2$. The actual FCS diffusion law can be calculated from the slopes derived from this intuitive model, and the crossover obtained from the simulations; we find

$$t_d = \begin{cases} \dfrac{w^2}{4D_{micro}} & \text{if } X_c^2 < 2 \quad (8) \\ S_{conf}\dfrac{w^2}{4D_{micro}} + k(\tau_d^{domain} - \tau_{conf}) & \text{if } X_c^2 > 2 \quad (9) \end{cases}$$

with $k = 8/(\pi \times 1.122^2) \approx 2$.

These equations fit quite nicely the FCS diffusion laws obtained from the simulations (data not shown). Note that the determination of the crossover point provides a measure of the mesh size.

Interpretation of the experimental results

Diffusion modes encountered in COS-7 cells

To end up our discussion, we now come back on the experimental results that have been presented in Fig. 4. In the framework of our model, the diffusion modes of both the FL-G_{M1} and the TfR-GFP can now be inferred from the shapes of the measured FCS diffusion laws. For FL-G_{M1}, the large waists diffusion law (regime iii) can be fitted by a line with a positive intercept. This diffusion law is well described by the microdomain model. This can be related to the fact that FL-G_{M1} is a putative raft marker, which means that biochemical studies show that it partitions into rafts.

For TfR-GFP, the large waists diffusion law (regime iii) is a line with a negative intercept, which is compatible with a diffusion hindered by the cytoskeleton meshwork.

Confinement time values

Through biochemical studies, it has be shown that 40% of G_{M1} partition into detergent resistant membranes (35,36), whereas its fluorescent analog FL-G_{M1} is expected to have a much smaller partition coefficient (37). Thus, a lower limit of the confinement time into microdomains can be inferred from the partition α and the intercept t_0 : $\tau_{conf} - \tau_d^{domain} \geq 30 \pm 10$ ms.

An upper limit can be given to the microdomain radius, because the sole affine regime (iii) is observed experimentally. Since this regime corresponds to $X_c^2 > 10$ and the experimental waist is >200 nm (diffraction-limited), the maximum value for the microdomain radius should be ~60 nm. Moreover, at a waist of 200 nm, we measured a diffusion time of 30 ms. Thus, the diffusion time through a domain would be at most 3 ms. The time intercept being much larger than this time, we can conclude that $\tau_{conf} \gg \tau_{diff}$ and $\tau_{conf} \geq 30 \pm 13$ ms.

The confinement time in a mesh of the cytoskeleton can also be calculated from the negative time intercept of TfR-GFP diffusion law, since $\tau_{conf} - \tau_d^{domain} = 10 \pm 1$ ms.

As mentioned before, these two diffusion examples are representative of some more experimental results that will be presented in detail in Lenne et al. (unpublished).

CONCLUSION

Because FCS has a high temporal resolution, it can easily capture millisecond range phenomena, in particular transient confinements, which are difficult to study with other techniques. In this article, we have shown that the ''FCS diffusion laws'', which are obtained by FCS measurements at various spatial scales, give valuable information on the diffusion processes taking place in the membranes. The shape of such FCS diffusion laws distinguishes between two different diffusion modes: diffusion among isolated microdomains (as for FL-G_{M1}) and diffusion hindered by a meshwork (as for TfR-GFP). In the regime where the laser waist w is much larger than the domain or mesh extension, we have demonstrated that the FCS diffusion laws can provide physical parameters such as the residence time into a single microdomain or mesh and an effective diffusion coefficient. Furthermore, we have shown that the FCS diffusion laws split in various regimes depending on the ratio of the waist w over the size of the microdomains (or meshes). The validity of the models has been extensively tested in membranes of live cells (more examples are given and exploited in Lenne et al. (unpublished)). These results show that FCS diffusion laws are relevant to study confinement and permit inferences about the dynamic organization of the cell membrane. We hope that these ''FCS diffusion laws'' will constitute a framework to study complex diffusion in model systems and membranes of live cells.

From a biological point of view, this will unravel the relationship between molecular confinement and biological functions such as signaling processes. From a physical point of view, this offers a new tool to study the transition from anomalous to normal diffusion (38).

APPENDIX: EFFECTIVE DIFFUSION COEFFICIENT AND TIME INTERCEPT FOR THE MICRODOMAIN MODEL

When domains are fully impermeable and molecules are restricted to diffuse outside of them, the diffusion law in regime iii is a line with a null intercept, which gives an effective diffusion coefficient D_{obst}:

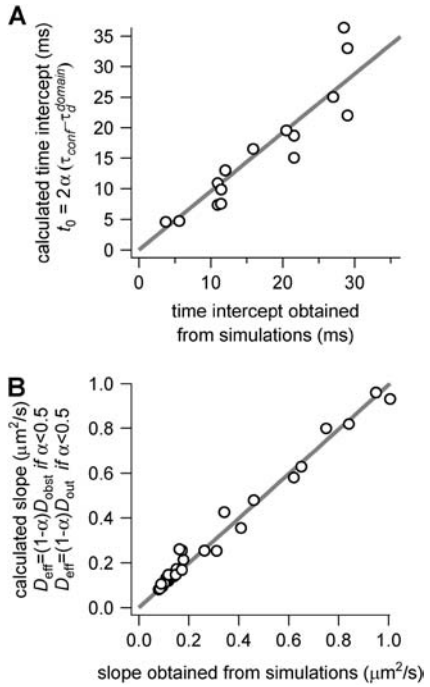

FIGURE 12 Parameters of the line describing regime iii of molecules in isolated domains geometry. (*A*) Time intercept t_0 as calculated by Eq. 6 versus the time intercept obtained from the simulations. (*B*) Slope $1/(4D_{\text{eff}})$ calculated by Eq. 7 as a function of the slope obtained from the simulations.

$$D_{\text{obst}} = f(d)D_{\text{out}},$$

where $f(d)$ is a function of the surface density d covered by the obstacles. In the case of periodically distributed impermeable circular obstacles and for $0.1 < d < 0.6$, we obtain from fit $f(d) = (1-d)/(1-0.6d)$ (data not shown).

To confront our heuristic model with the simulation results, we compare the calculated time intercept and slope given by Eqs. 6 and 7 with those obtained from our simulations. Fig. 12 shows that both the time intercept and the effective diffusion coefficient are very well described by Eqs. 6 and 7.

We thank H. Qasmi and N. Bertaux for technical help in simulations and P. Pelcé for helpful discussions.

This work was supported by institutional grants from the Centre National de la Recherche Scientifique and Institut National de la Santé et de la Recherche Médicale, and by specific grants from the Fondation pour la Recherche Médicale, Ministère de l'Education Nationale, de l'Enseignement Supérieur et de la Recherche, and Centre National de la Recherche Scientifique. L.W. is recipient of a doctoral fellowship from the Ministère de l'Education Nationale, de l'Enseignement Supérieur et de la Recherche.

REFERENCES

1. Jacobson, K., E. D. Sheets, and R. Simson. 1995. Revisiting the fluid mosaic model of membranes. *Science*. 268:1441–1442.
2. Kusumi, A., Y. Sako, and M. Yamamoto. 1993. Confined lateral diffusion of membrane receptors as studied by single particle tracking (nanovid microscopy). Effects of calcium-induced differentiation in cultured epithelial cells. *Biophys. J.* 65:2021–2040.
3. Fujiwara, T., K. Ritchie, H. Murakoshi, K. Jacobson, and A. Kusumi. 2002. Phospholipids undergo hop diffusion in compartmentalized cell membrane. *J. Cell Biol.* 157:1071–1081.
4. Singer, S. J., and G. L. Nicolson. 1972. The fluid mosaic model of the structure of cell membranes. *Science*. 175:720–731.
5. Brown, D. A., and J. K. Rose. 1992. Sorting of GPI-anchored proteins to glycolipid-enriched membrane subdomains during transport to the apical cell surface. *Cell*. 68:533–544.
6. Simons, K., and E. Ikonen. 1997. Functional rafts in cell membranes. *Nature*. 387:569–572.
7. Brown, D. A., and E. London. 2000. Structure and function of sphingolipid- and cholesterol-rich membrane rafts. *J. Biol. Chem.* 275: 17221–17224.
8. Varma, R., and S. Mayor. 1998. GPI-anchored proteins are organized in submicron domains at the cell surface. *Nature*. 394:798–801.
9. Saxton, M. J., and K. Jacobson. 1997. Single-particle tracking: applications to membrane dynamics. *Annu. Rev. Biophys. Biomol. Struct.* 26:373–399.
10. Schutz, G. J., G. Kada, V. P. Pastushenko, and H. Schindler. 2000. Properties of lipid microdomains in a muscle cell membrane visualized by single molecule microscopy. *EMBO J.* 19:892–901.
11. Pralle, A., P. Keller, E. L. Florin, K. Simons, and J. K. Horber. 2000. Sphingolipid-cholesterol rafts diffuse as small entities in the plasma membrane of mammalian cells. *J. Cell Biol.* 148:997–1008.
12. Saxton, M. J. 1995. Single-particle tracking: effects of corrals. *Biophys. J.* 69:389–398.
13. Weiss, M., H. Hashimoto, and T. Nilsson. 2003. Anomalous protein diffusion in living cells as seen by fluorescence correlation spectroscopy. *Biophys. J.* 84:4043–4052.
14. Wawrezinieck, L., P.-F. Lenne, D. Marguet, and H. Rigneault. 2004. Fluorescence correlation spectroscopy to determine diffusion laws: application to live cell membranes. *Proc. SPIE Int. Soc. Opt. Eng.* 5462:92–103.
15. Masuda, A., K. Ushida, and T. Okamoto. 2003. Japanese Patent Application. (Published as Japanese Patent Publication No. 2005–043278, Feb. 17, 2005). Tokyo, Japan.
16. Masuda, A., K. Ushida, and T. Okamoto. 2005. New fluorescence correlation spectroscopy enabling direct observation of spatiotemporal dependence of diffusion constants as an evidence of anomalous transport in extracellular matrices. *Biophys. J.* 88:3584–3591.
17. Schwille, P. 2001. Fluorescence correlation spectroscopy and its potential for intracellular applications. *Cell Biochem. Biophys.* 34:383–408.
18. Gennerich, A., and D. Schild. 2002. Anisotropic diffusion in mitral cell dendrites revealed by fluorescence correlation spectroscopy. *Biophys. J.* 83:510–522.
19. Gennerich, A., and D. Schild. 2000. Fluorescence correlation spectroscopy in small cytosolic compartments depends critically on the diffusion model used. *Biophys. J.* 79:3294–3306.
20. Pagano, R. E., and O. C. Martin. 1998. Cell Biology: A Laboratory Handbook. Academic Press, San Diego, CA.
21. Elson, E. L., and D. Magde. 1974. Fluorescence correlation spectroscopy. *Biopolymers*. 13:1–27.
22. Bouchaud, J. P., and A. Georges. 1990. Anomalous diffusion in disordered media: statistical mechanisms, models and physical applications. *Phys. Rep.* 195:127–293.
23. Yechiel, E., and M. Edidin. 1987. Micrometer-scale domains in fibroblast plasma membranes. *J. Cell Biol.* 105:755–760.
24. Lopez, A., L. Dupou, A. Altibelli, J. Trotard, and J. F. Tocanne. 1988. Fluorescence recovery after photobleaching (FRAP) experiments under conditions of uniform disk illumination. Critical comparison of analytical solutions, and a new mathematical method for calculation of diffusion coefficient D. *Biophys. J.* 53:963–970.
25. Wohland, T., R. Rigler, and H. Vogel. 2001. The standard deviation in fluorescence correlation spectroscopy. *Biophys. J.* 80:2987–2999.

26. Schätzel, K. 1985. New concepts in correlator design. *In* Institute of Physics Conference Series. Hilger, London. 77:175–184.

27. Press, W. H., S. A. Teukolsky, W. T. Vetterling, and B. P. Flannery. 1992. Numerical Recipes in C: The Art of Scientific Computing. Cambridge University Press, Cambridge, U.K.

28. Fahey, P. F., D. E. Koppel, L. S. Barak, D. E. Wolf, E. L. Elson, and W. W. Webb. 1977. Lateral diffusion in planar lipid bilayers. *Science*. 195:305–306.

29. Dietrich, C., L. A. Bagatolli, Z. N. Volovyk, N. L. Thompson, M. Levi, K. Jacobson, and E. Gratton. 2001. Lipid rafts reconstituted in model membranes. *Biophys. J*. 80:1417–1428.

30. Lenne, P.-F., E. Etienne, and H. Rigneault. 2002. Subwavelength patterns and high detection efficiency in fluorescence correlation spectroscopy using photonic structures. *Appl. Phys. Lett*. 80:4106–4108.

31. Hess, S. T., S. Huang, A. A. Heikal, and W. W. Webb. 2002. Biological and chemical applications of fluorescence correlation spectroscopy: a review. *Biochemistry*. 41:697–705.

32. Schwille, P., U. Haupts, S. Maiti, and W. W. Webb. 1999. Molecular dynamics in living cells observed by fluorescence correlation spectroscopy with one- and two-photon excitation. *Biophys. J*. 77:2251–2265.

33. Kusumi, A., C. Nakada, K. Ritchie, K. Murase, K. Suzuki, H. Murakoshi, R. S. Kasai, J. Kondo, and T. Fujiwara. 2005. Paradigm shift of the plasma membrane concept from the two-dimensional continuum fluid to the partitioned fluid: high-speed single-molecule tracking of membrane molecules. *Annu. Rev. Biophys. Biomol. Struct*. 34:351–378.

34. Simson, R., B. Yang, S. E. Moore, P. Doherty, F. S. Walsh, and K. A. Jacobson. 1998. Structural mosaicism on the submicron scale in the plasma membrane. *Biophys. J*. 74:297–308.

35. Fra, A. M., E. Williamson, K. Simons, and R. G. Parton. 1994. Detergent-insoluble glycolipid microdomains in lymphocytes in the absence of caveolae. *J. Biol. Chem*. 269:30745–30748.

36. Blank, N., C. Gabler, M. Schiller, M. Kriegel, J. R. Kalden, and H. M. Lorenz. 2002. A fast, simple and sensitive method for the detection and quantification of detergent-resistant membranes. *J. Immunol. Methods*. 271:25–35.

37. Kuerschner, L., C. S. Ejsing, K. Ekroos, A. Shevchenko, K. I. Anderson, and C. Thiele. 2005. Polyene-lipids: a new tool to image lipids. *Nat. Methods*. 2:39–45.

38. Saxton, M. J. 1996. Anomalous diffusion due to binding: a Monte Carlo study. *Biophys. J*. 70:1250–1262.

The EMBO Journal (2006) 25, 3245–3256 | © 2006 European Molecular Biology Organization | All Rights Reserved 0261-4189/06
www.embojournal.org

THE EMBO JOURNAL

Dynamic molecular confinement in the plasma membrane by microdomains and the cytoskeleton meshwork

Pierre-François Lenne[1,2,7], Laure Wawrezinieck[1,2,3,4,5,7], Fabien Conchonaud[3,4,5], Olivier Wurtz[3,4,5,8], Annie Boned[3,4,5], Xiao-Jun Guo[3,4,5,6], Hervé Rigneault[1,2], Hai-Tao He[3,4,5] and Didier Marguet[3,4,5,*]

[1]Institut Fresnel, Université Paul Cézanne, Marseille, France, [2]CNRS UMR 6133, Marseille, France, [3]Centre d'Immunologie de Marseille-Luminy, Université de la Méditerranée, Marseille, France, [4]INSERM, UMR 631, Marseille, France, [5]CNRS, UMR 6102, Marseille, France and [6]Laboratoire de Biochimie et Physicochimie des Membranes Biologiques, Université Paul Cézanne, Marseille, France

It is by now widely recognized that cell membranes show complex patterns of lateral organization. Two mechanisms involving either a lipid-dependent (microdomain model) or cytoskeleton-based (meshwork model) process are thought to be responsible for these plasma membrane organizations. In the present study, fluorescence correlation spectroscopy measurements on various spatial scales were performed in order to directly identify and characterize these two processes in live cells with a high temporal resolution, without any loss of spatial information. Putative raft markers were found to be dynamically compartmented within tens of milliseconds into small microdomains ($\varnothing < 120$ nm) that are sensitive to the cholesterol and sphingomyelin levels, whereas actin-based cytoskeleton barriers are responsible for the confinement of the transferrin receptor protein. A free-like diffusion was observed when both the lipid-dependent and cytoskeleton-based organizations were disrupted, which suggests that these are two main compartmentalizing forces at work in the plasma membrane.

The EMBO Journal (2006) **25,** 3245–3256. doi:10.1038/sj.emboj.7601214; Published online 6 July 2006
Subject Categories: membranes & transport
Keywords: actin meshwork; confined diffusion; fluorescence correlation spectroscopy; lipid rafts; membrane microdomain

Introduction

Although it is generally assumed that lateral heterogeneities exist in cell membranes (Edidin, 2003; Simons and Vaz, 2004), the factors responsible for the local organization of the plasma membrane are poorly understood. Various mechanisms have been suggested to explain the significant discrepancies observed in the diffusion rates of lipids and proteins between artificial membranes and plasma membranes. For instance, membrane protein diffusion differs from pure Brownian diffusion because of the transient interactions occurring with large multimeric complexes (Marguet *et al*, 1999), the obstacles resulting from direct and indirect molecular immobilization (Sako and Kusumi, 1994; Fujiwara *et al*, 2002), and the corrals formed on various submicrometric scales (Yechiel and Edidin, 1987). There is still some controversy about the ability of lipids to form domains, which are also known as lipid rafts, in plasma membranes (Simons and Ikonen, 1997; Brown and London, 1998; Edidin, 2003; Munro, 2003; Simons and Vaz, 2004; van Meer, 2005; Marguet *et al*, 2006). In these lipid domains, cholesterol is thought to be tightly packed with long saturated fatty acid chains of specific glycosphingolipids, thus favoring lipid phase separation processes. It has been suggested that these domains may be insoluble in nonionic detergents (Brown and London, 1998; Drevot *et al*, 2002). In addition to studies characterizing biochemical rafts, morphological approaches have been used to prove the existence of these rafts in cell membranes, but the conclusions drawn have been rather controversial, since the results depended strongly on the methods used. When the lateral motion of lipid probes was analyzed using single dye tracing methods, the domain size was found to range from 0.2 to 2 μm (Schutz *et al*, 2000). These data are in the same range as those obtained on the barrier-free paths of membrane proteins, but the latter depend mainly on how the cytoskeleton is organized (Sako and Kusumi, 1994). Other studies using biophysical approaches on live cells have strongly supported the idea that rafts are small diffusive entities (Pralle *et al*, 2000; Sharma *et al*, 2004). Fluorescence resonance energy transfer methods (FRET) have been used to probe the molecular aggregates present in lipid rafts. Experiments of this kind using different lipid-modified proteins expressed in the apical membrane of MDCK cells have led to divergent conclusions (Kenworthy and Edidin, 1998; Zacharias *et al*, 2002; Hess *et al*, 2005). FRAP measurements on live cells have provided evidence that the anchoring mode determines the protein–raft interaction dynamics (Shvartsman *et al*, 2003). A direct visualization of liquid-ordered domains was recently obtained using fluorescent cell staining procedures, although information is still lacking about the dynamic aspects of these structures (Gaus *et al*, 2003). In fact, these methods span different spatiotemporal scales, and the data obtained about the features of rafts, and even their existence in live cells, may therefore not always seem to be in agreement.

Improving our knowledge of membrane organization requires developing new methods in which the temporal resolution is improved without any loss of spatial information. For instance, FRAP measurements performed on different

*Corresponding author. Centre d'Immunologie de Marseille Luminy, CNRS, Parc Scientifique de Luminy, Case 906, 13288 Marseille Cedex 13009, France. Tel.: +33 491 269 128; Fax: +33 491 269 430;
E-mail: marguet@ciml.univ-mrs.fr
[7]These authors contributed equally to this work
[8]Present address: Université de Rouen, INSERM U413, Mont Saint Aignan, France

Received: 9 February 2006; accepted: 6 June 2006; published online: 6 July 2006

spatial scales have made it possible to identify micrometer-scale domains present in the plasma membrane of fibroblasts (Yechiel and Edidin, 1987). By applying a similar strategy using fluorescence correlation spectroscopy (FCS) methods, we recently managed to distinguish between different submicron confinement models. In the latter study, we described a novel method of performing FCS on various observation scales (Wawrezinieck *et al*, 2004) and developed a simple analytical method of investigating the complexity of the cell membrane organization and the dynamic processes involved (Wawrezinieck *et al*, 2005). This novel method could be used to identify and discriminate between variously organized submicroscopic domains preventing the free lateral diffusion of membrane components (Saxton, 2005). The *FCS Diffusion Law* was defined in the latter study as the plot of the diffusion time (i.e. the average time a fluorescent molecule stays within the illuminated area) versus the observation area. Based on extensive confined diffusion modeling studies, it was established that the *y*-intercept t_0 in the graph of the FCS diffusion laws is positive in the case of confining in microdomains (dynamic partitioning into microdomains) but negative in that of trapping in a meshwork (actin-based cytoskeleton corrals).

Here, it was proposed to investigate the dynamics of membrane organization in live cells. The diffusion behavior of various membrane components was described and it was established whether molecular confinement depends on the specific cholesterol/sphingomyelin membrane content or on the presence of actin-based cytoskeleton barriers.

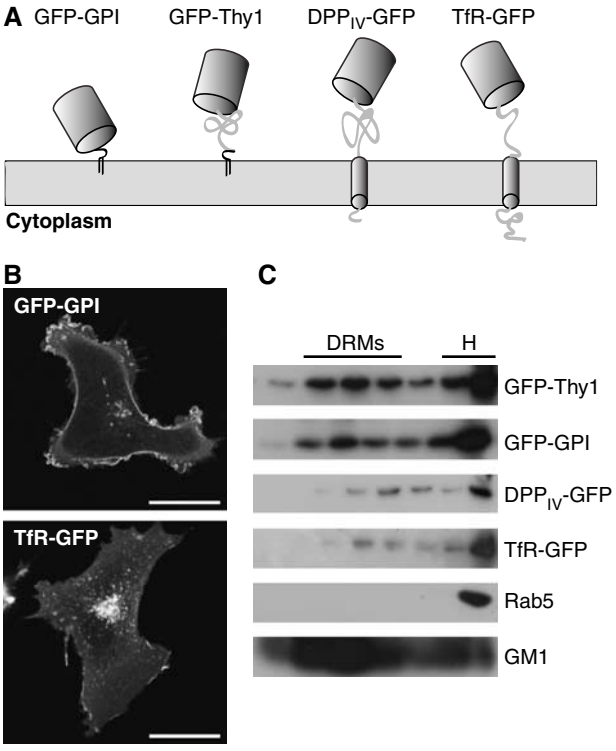

Figure 1 GFP-tagged proteins used in this study. (**A**) Membrane topology of the GFP-tagged proteins. (**B**) Confocal images of COS-7 cells expressing the GFP-GPI and TfR-GFP proteins. Scale bar is 20 μm. (**C**) Brij 98 solubilized PNS from transfected COS-7 cells was fractionated on the sucrose gradient and blotted with anti-GFP, anti-Rab 5 antibodies or cholera toxin B.

Results

Molecules used to establish the presence of domains in plasma membranes

To establish the presence of domains in the plasma membrane, the diffusion behavior of four different groups of membrane components was investigated: (1) a glycerophospholipid group with two fluorescent lipid analogs, BODIPY-C_5-phosphatidylcholine (FL-PC) and BODIPY-dihexadecanoyl-phospho-ethanolamine (FL-PE), (2) a sphingolipid group including the BODIPY-C_5-sphingomyelin (FL-SM) and BODIPY-C_5-ganglioside-G_{M1} (FL-G_{M1}) analogs, (3) a glycosylphosphatidylinositol (GPI)-anchored protein group in which the GFP was either tagged onto the GPI-anchoring signal originating from the decay accelerating factor (GFP-GPI) or inserted just after the signal peptide of Thy1 (GFP-Thy1), and (4) a GFP-tagged transmembrane protein group including the dipeptidyl peptidase IV (DPP$_{IV}$-GFP) and the transferrin receptor (TfR-GFP) (Figure 1A).

To examine the mobility of lipid analogs, COS-7 cells were labeled using the lipid exchange method (Martin and Pagano, 1994). Laser scanning confocal microscopy showed that the probes were uniformly distributed in the plasma membrane. A vesicular staining pattern consisting of small intracellular dots was also observed (Figure 2A–C). All the GFP-tagged proteins were efficiently addressed to the plasma membrane when transiently expressed in COS-7 cells (Figure 1B and data not shown). Vesicular staining was also detected in the cytosol, especially in the perinuclear area.

Based on previous studies, these molecules are known to be either present in high levels or depleted from detergent resistant membranes (DRMs). This was confirmed by Brij 98 detergent-insolubility experiments performed at physiological temperatures (Drevot *et al*, 2002). Although the BODIPY fluorophore can affect the properties of lipids, yielding analogs with quite different characteristics from those of their natural counterparts (Kuerschner *et al*, 2005), both FL-G_{M1} and FL-SM were readily detected in DRMs, where they accounted for 11 and 17% of the total fluorescence, respectively. This association is not negligible, since under the same experimental conditions, about 20% of the GFP-Thy1 or GFP-GPI molecules were detected in DRMs, whereas those anchored by a classical transmembrane peptide were barely detectable (Figure 1C).

The different groups of membrane components follow distinct FCS diffusion laws

As described previously, the *FCS diffusion law* giving the diffusion time τ_d (i.e. the average time a fluorescent molecule stays within the illuminated area) versus the beam area, where w denotes the beam radius, should provide a suitable analytical method for determining the diffusion behavior of a molecule in the membrane (Saxton, 2005; Wawrezinieck *et al*, 2005). This approach is based on the fact that if molecules diffuse freely, one can expect to obtain a linear function between τ_d and w^2: the curve $\tau_d = f(w^2)$ will intercept the time origin and its slope will correspond to the diffusion coefficient D in this environment. In most situations where diffusion is hindered, the FCS diffusion law will no longer fit this scheme. By sizing the laser beam filling the microscope objective, we varied w experimentally from 200

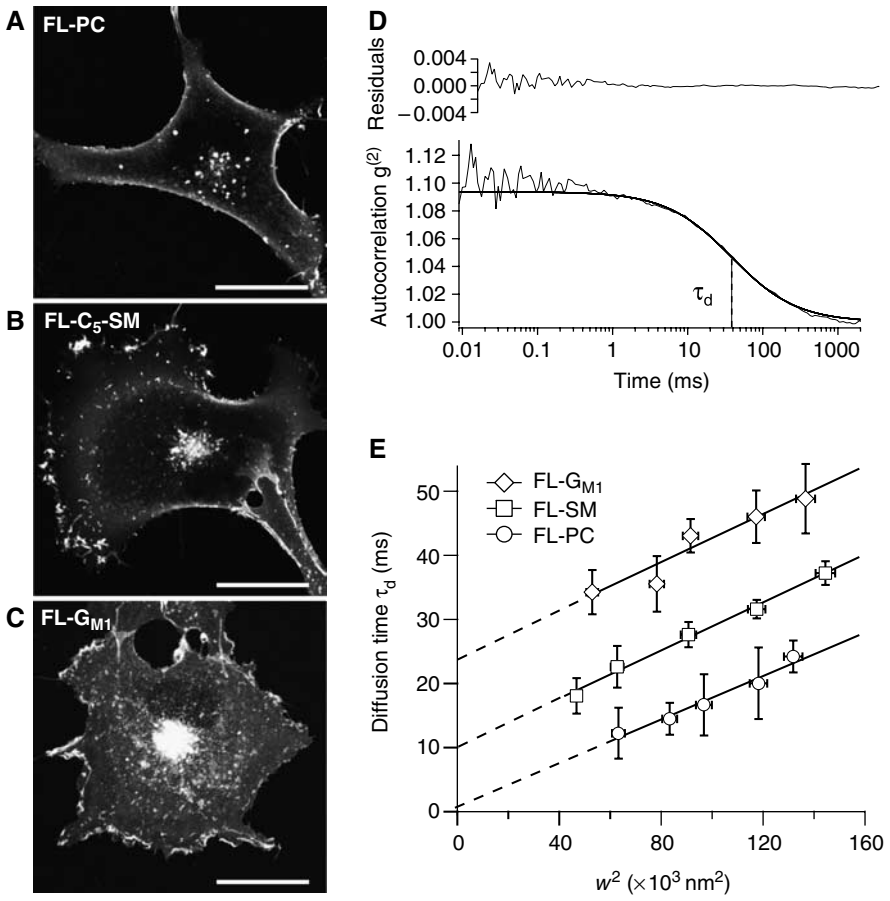

Figure 2 Diffusion behavior of lipid analogs. Confocal images of COS-7 cells after labeling with lipid analogs: (**A**) FL-PC, (**B**) FL-SM and (**C**) FL-G_{M1}. Scale bar is 20 μm. (**D**) ACF obtained with FL-G_{M1} lipids. The curve was satisfactorily fitted with a 1-species free diffusion model (see Supplementary data). The diffusion time τ_d was given by the lag time at half maximum. (**E**) Diffusion behavior of lipid analogs. Confinement times were determined from the position at which the diffusion curves and the time-axis intersected. Error bars in *x* and *y* give standard deviations (s.d.) of the means.

to 400 nm; the lower limit was imposed by the diffraction law, whereas the upper one was based on a compromise between the spatial resolution and FCS constraints.

We first investigated the lipid dynamics using trace mole fractions of probes relative to the total lipids in order to minimize any membrane perturbations. Based on experimental autocorrelation functions (ACF), the data were efficiently fitted using a single component, giving a single decay time (see Supplementary data and Figure 2D). In this case, τ_d was obtained by measuring the lag time at half the maximum ACF value. With all the lipid probes used, τ_d increased linearly with w^2 but the intersections with the time axis differed (Figure 2E). In the case of the glycerophospholipid analogs FL-PC and FL-PE, the FCS diffusion laws intercepted the time axis at the origin at almost null t_0 values (-0.4 ± 0.8 and 0.2 ± 0.7 ms, respectively). By contrast, t_0 was strictly positive in the case of the sphingolipid analogs FL-G_{M1}, FL-C_5-SM and FL-C_{12}-SM, where values of 24.3 ± 1.9, 10.2 ± 0.6 and 9.7 ± 0.5 ms were obtained, respectively.

With all the chimeric proteins used, two decay times were clearly identified from the ACFs (Figure 3A–B and data not shown): a short time τ_{fast} and a longer one τ_d. We checked that the slow decay time corresponded to the diffusion time of plasma membrane-bound molecules, whereas the fast one corresponded to that of the intracellular pool. When detected from outside by an Alexa488-conjugated anti-Thy1 Fab fragment, the lateral mobility of Thy1 showed a similar single long relaxation time to the longest one observed in the case of GFP-Thy1 (with a spot radius of ~240 nm, these times were 31.8 ± 5.8 and 27.4 ± 2.9 ms, respectively).

The FCS diffusion laws were then analyzed (Figure 3C). In the case of the two GPI-anchored proteins, GFP-Thy1 and GFP-GPI, t_0 was found to be significantly positive (18.4 ± 1.7 and 12.1 ± 2.5 ms, respectively), whereas the reverse was observed with the TfR-GFP, which gave a t_0 value of -20.4 ± 1.9 ms. Interestingly, the DPP_{IV}-GFP diffusion behavior was in between that observed with the GPI-anchored proteins and the TfR-GFP. The reason for this small positive intercept (4.8 ± 1.7 ms) will be discussed below.

In order to check whether the diffusion behavior reflected in the FCS corresponded to a significant fraction of the molecules tested, confocal FRAP measurements (Kenworthy *et al*, 2004) were performed. The mobile fraction M_f was assessed in terms of the percentage of the fluorescent molecules recovered in the bleached area during the FRAP experiment. All the lipid analogs were nearly 100% mobile, and $M_f > 95\%$ with FL-PC, FL-SM and FL-G_{M1}. In the case of the GFP-tagged proteins, the M_f value ranged between 77 and 92% (77, 85, 90 and 92% with TfR-GFP, DPP_{IV}-GFP, GFP-GPI and GFP-Thy1, respectively). The FCS diffusion laws given

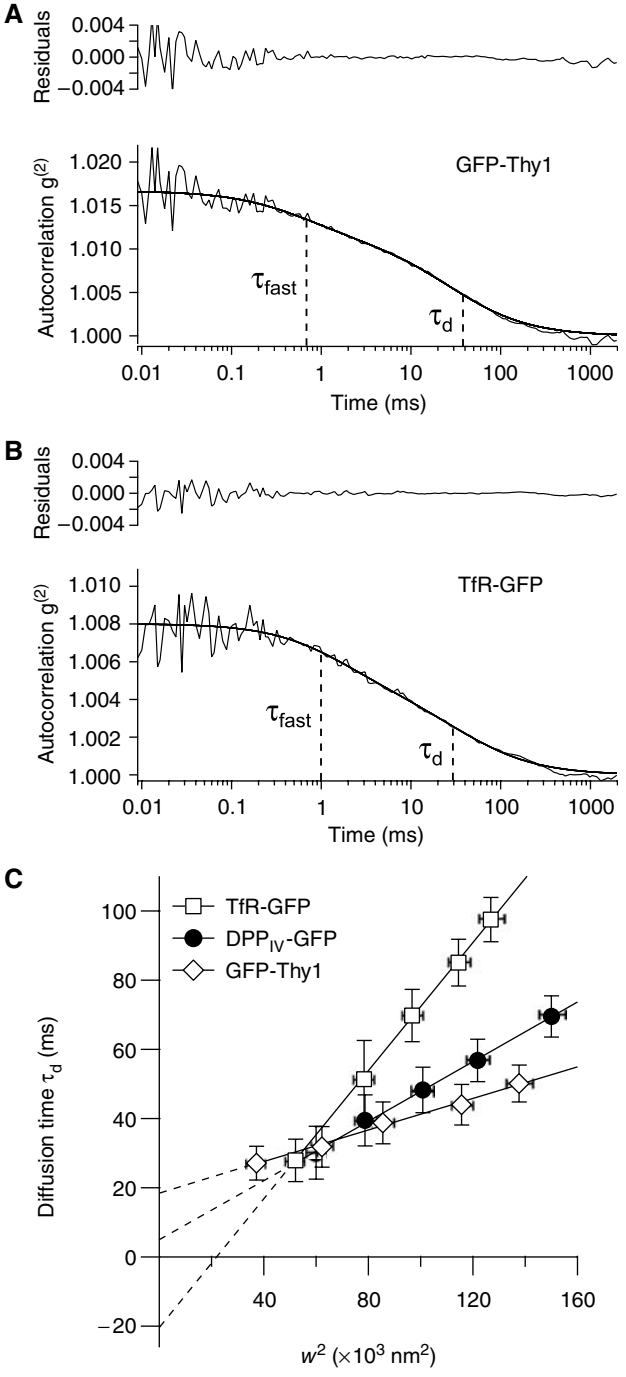

Figure 3 Diffusion behavior of GFP-tagged proteins. ACFs obtained with GFP-Thy1 (**A**) and TfR-GFP (**B**). In both cases, two decay times were clearly identified with the various probes used: a short time τ_{fast} and a longer one τ_d. (**C**) FCS diffusion laws in the case of TfR-GFP, DPP_{IV}-GFP and GFP-Thy1. Error bars on the *x* and *y* axes give the s.d.s of the means.

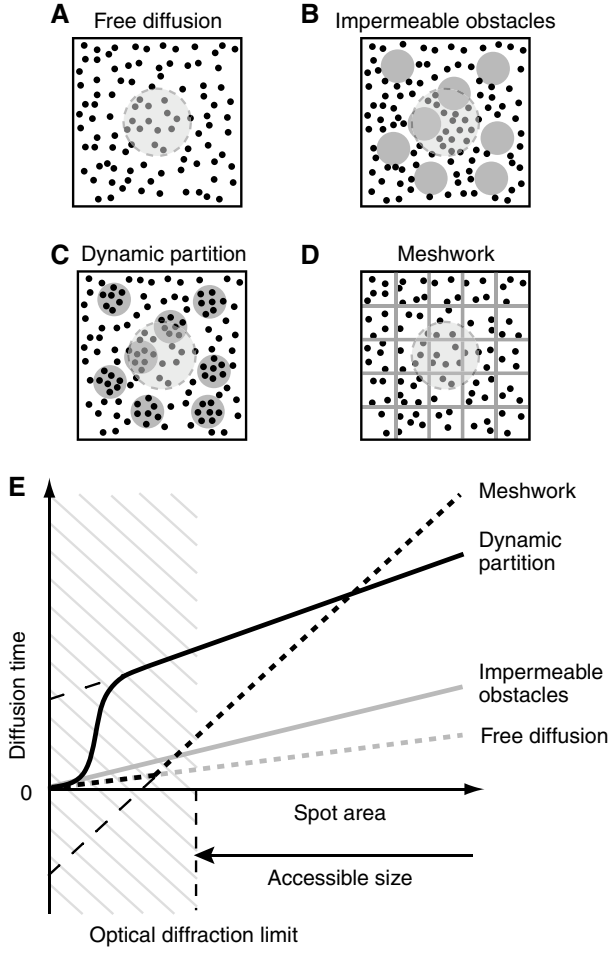

Figure 4 Simulated FCS diffusion laws corresponding to different membrane models. (A–D) Diffusion models for membrane organization. (**A**) In the free diffusion model, fluorescent molecules (black dots) show pure Brownian motion and fluoresce under the laser excitation spot (large gray circle). (**B**) In the presence of impermeable obstacles (gray spots), the diffusion is restricted to the free space. (**C**) When the domains are permeable (as the result of dynamic partition processes), the molecules can diffuse into and out of the microdomains and be transiently trapped (gray spots). (**D**) In a meshwork model, multiple adjacent domains are separated by barriers (gray lines) preventing the diffusion of the molecules. (**E**) Characteristic diffusion laws obtained for the different models. The diffusion time τ_d was analyzed as a function of the squared radius w^2. Diffusion laws applying to the free diffusion model (dotted gray curve), the diffusion process in the presence of impermeable obstacles (gray curve), the dynamic partition model (dotted black curve) and the meshwork model (black curve). Diffusion laws cannot be determined experimentally below the diffraction limit. For detailed analyses, see the Supplementary data and Wawrezinieck *et al* (2004, 2005).

above therefore accurately describe the behavior of a very large fraction of the lipid analogs and GFP-tagged proteins.

A broad range of t_0 values was obtained with the various molecules used to explore the occurrence of domains in the plasma membrane. Based on this parameter, three subsets of molecules were identified: the glycerophospholipid analogs (null t_0), the sphingolipid and GPI-anchored protein groups (positive t_0) and the transmembrane TfR-GFP (negative t_0).

In view of the above data and the results of our previous numerical simulations (Wawrezinieck *et al*, 2005), where the change in the sign of the *y*-intercept t_0 was correlated with different modes of membrane compartmentalization, we hypothesized that simple confinement models would explain the deviations from free diffusion (Figure 4; see also the Supplementary data). A positive t_0 was linked, for example, to the dynamic partition model, which may provide a basis for explaining the diffusion behavior of the sphingolipid and GPI-anchored protein groups, whereas with a negative t_0, TfR molecules may be subjected to membrane confinement due

to meshwork effects. Lastly, because of the null t_0, the glycerophospholipid analogs may neither be confined within discrete domains nor be hindered by a meshwork.

A lipid-dependent microdomain organization confines sphingolipid analogs and GPI-anchored proteins within the plasma membrane of resting cells

Among the mechanisms possibly responsible for confinement in discrete microdomains, several lines of evidence combine to support the idea that cholesterol and sphingomyelin are involved in the control and the organization of local heterogeneities: the differential packing characteristics of glycerophospholipids and sphingolipids with cholesterol promote the formation of a liquid-ordered phase or a similar state, which coexists in the membrane plane with a liquid-disordered phase (Brown and London, 1998; Rietveld and Simons, 1998). To test whether this hypothesis holds in the case of sphingolipid analogs and GPI-anchored proteins, cells were incubated in the presence of exogenous cholesterol oxidase (COase) or sphingomyelinase (SMase) to decrease the cholesterol and sphingomyelin membrane contents, respectively.

With 1 U/ml of COase, $23.3 \pm 2.2\%$ of the total cell cholesterol was converted into cholestenone. The ability of GPI-anchored proteins and sphingolipid analogs to float to the buoyant fractions of a sucrose gradient was subsequently found to be severely impaired (Figure 5A), and the FL-SM and FL-G_{M1} present in DRMs, as measured by spectrofluorimetry, decreased by 58 and 63%, respectively. This decrease in the cholesterol levels also induced significant changes in the behavior of GFP-GPI, since the curve of the corresponding FCS diffusion law then intercepted the time origin (0.2 ± 0.8 ms) (Figure 5B). Similar results were obtained with GFP-Thy1 and the sphingolipid analogs (Figures 5C, D

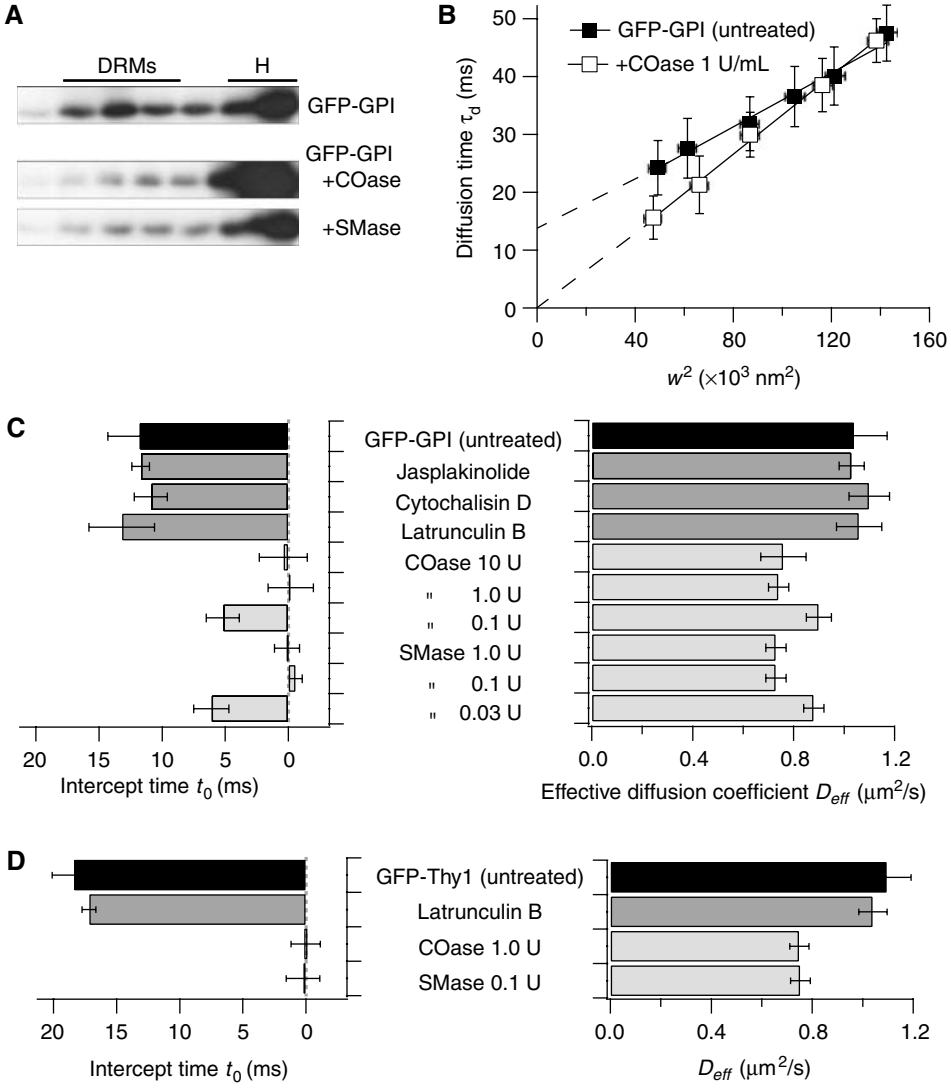

Figure 5 The confinement of GFP-tagged GPI-anchored proteins in microdomains is lipid-dependent. (**A**) Biochemical determination of GFP-GPI localization in DRMs after COase or SMase treatment. (**B**) FCS diffusion laws governing GFP-GPI proteins after cell treatment with COase. Error bars on the *x* and *y* axes are the s.d.s of the means. (**C**) Time intercept t_0 and effective diffusion coefficient D_{eff} obtained with GFP-GPI in untreated COS-7 cells (black bars), after cytoskeleton drug treatments (dark gray bars) or lipid modifications (light gray bars). (**D**) Idem in the case of GFP-Thy1 protein.

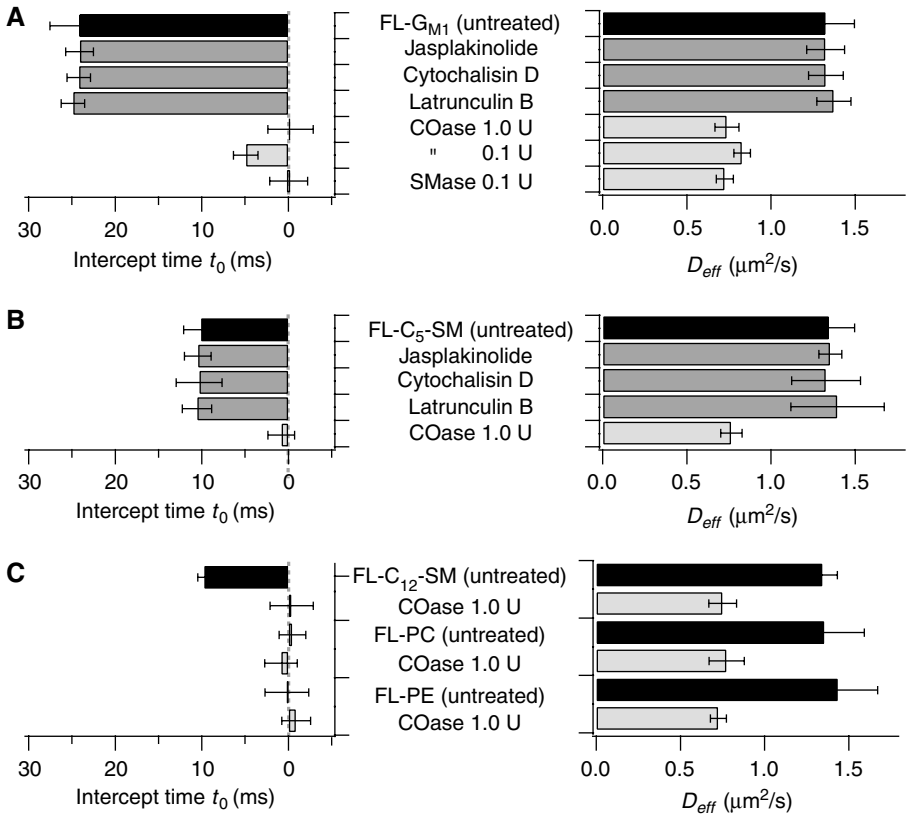

Figure 6 The confinement of lipid probes in the plasma membrane of COS-7 cells is lipid-dependent. Time intercept t_0 and effective diffusion coefficient D_{eff} obtained with FL-G$_{M1}$ (**A**), FL-C$_5$-SM (**B**) and the other lipid analogs used in this study (**C**) in untreated COS-7 cells (black bars), after applying cytoskeleton drug treatment (dark gray bars) or lipid modifications (light gray bars). Error bars give the s.d.s of the means.

and 6, respectively). Importantly, a 10-fold lower enzyme concentration, which converted $<10\%$ of the total cholesterol into cholestenone ($8.2\pm4.4\%$), led to an intermediate value between those obtained with cells treated and not with 1 U/ml of COase, as illustrated here in the case of GFP-GPI and FL-G$_{M1}$, (Figures 5C and 6A, respectively). The effects of the larger changes in the cholesterol content ($56.9\pm4.7\%$) induced by 10 U/ml of COase did not differ from those observed with 1 U/ml. All in all, these results suggest that the microdomain organization generated by dynamic partitioning processes no longer existed in these cell membranes.

We then hydrolyzed SM into ceramide by adding exogenous SMase to COS-7 cells. With 0.1 U/ml of SMase, $68\pm4\%$ of the total SM was hydrolyzed. At the same time, we noted that the presence of GFP-GPI within DRMs was also severely impaired after enzymatic treatment (Figure 5A). More importantly, the curves of all the FCS diffusion laws governing GFP-GPI, GFP-Thy1 and FL-G$_{M1}$ intercepted the time origin (Figures 5C–D and 6A). Once again, we observed that the SM membrane concentration was critical, since titration experiments showed that the confinement of GFP-GPI disappeared in a dose-dependent manner (Figure 5C). Lower concentrations (0.03 U/ml) converting $54\pm4\%$ of the total SM led to an intermediate value between those obtained with cells treated or not with 0.1 U/ml of SMase, as illustrated in the case of GFP-GPI and FL-G$_{M1}$. The effects of higher SMase concentrations (1 U/ml) did not differ from those observed with 0.1 U/ml.

It was remarkable that the lipid-mediated microdomain organization was entirely abolished when only $\sim20\%$ of the total cholesterol was converted into cholestenone by COase. This could be due to a combined effect of cholesterol hydrolysis and cholestenone production, since an antagonizing action of the cholestenone to ordered domains has been reported (Xu and London, 2000). A similar scenario might occur upon SMase treatment as well. Ceramide has recently been shown to displace cholesterol from sphingomyelin-cholesterol domains as well as to induce strong alterations of the lateral organization in model membranes (Megha and London, 2004).

After COase or SMase treatment, a similar decrease in D_{eff} occurred in both the GPI-anchored proteins and sphingolipid analogs ($\sim0.75\,\mu m^2/s$) (Figures 5 and 6). The fact that this was also the case with the glycerophospholipid analogs although the t_0 value was still null (Figure 6C) suggested that an overall change in the plasma membrane viscosity had also occurred due to the enzymatic change in the lipid membrane composition. All in all, these results strongly support the idea that in the absence of molecular crosslinking processes, sphingolipid analogs and GPI-anchored proteins are confined by a cholesterol and sphingomyelin-dependent process of microdomain formation.

A cytoskeleton-mediated meshwork hinders the lateral mobility of TfR-GFP

The TfR-GFP diffusion law curve, which showed a negative t_0, suggested that TfR molecules diffused in a meshwork

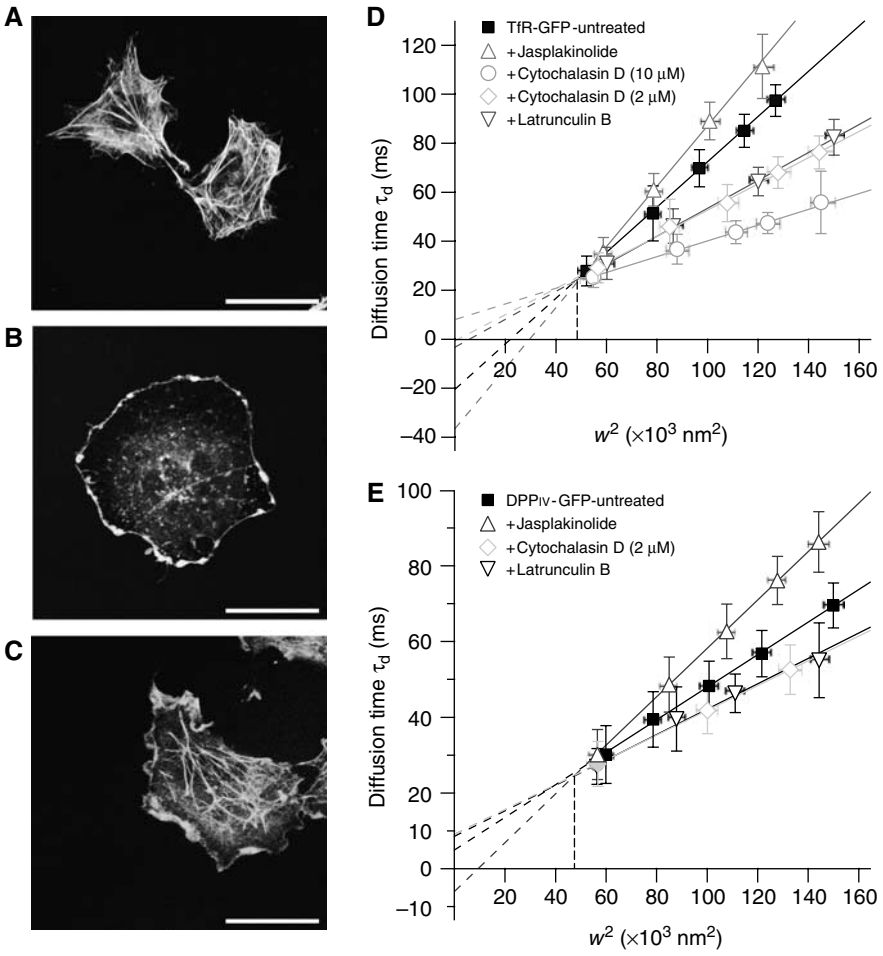

Figure 7 The GFP-tagged transmembrane protein diffusion laws are actin-dependent. Confocal images of rhodamine phalloidin labeling of F-actin in COS-7: (**A**) untreated; (**B**) 1 μM latrunculin B; (**C**) 0.4 μM jasplakinolide. Diffusion laws governing TfR-GFP (**D**) and DPP_{IV}-GFP (**E**) after applying cytoskeleton drug treatment. Error bars on the *x* and *y* axes are the s.d.s of the means.

context (Figure 4D and E). To investigate the possible involvement of the cytoskeleton, COS-7 cells were treated with drugs known to alter the actin-based cytoskeleton, such as latrunculin-B (an actin polymerization inhibitor), cytochalasin D (an actin depolymerization inducer) or jasplakinolide (an actin filament stabilizer). Suitable experimental conditions were first setup to ensure that these drugs changed the pattern of cytoskeleton organization without significantly affecting the cell morphology (Figure 7A–C).

The lateral mobility of TfR-GFP was then assessed (Figure 7D). Under latrunculin B (1 μM) or cytochalasin D (2 μM) treatment, the FCS diffusion law curve intercepted the *y*-axis near the time origin (-3.2 ± 1.8 and 0.7 ± 1.8 ms, respectively). These findings indicate that the physical barriers confining TfR-GFP were lowered. At the same time, the D_{eff} value increased from 0.27 ± 0.01 to $0.44 \pm 0.02\,\mu m^2/s$, which suggests that the long-range diffusion was less strongly impeded by the barriers between adjacent domains. Conversely, treatment with jasplakinolide (0.4 μM) decreased both the D_{eff} and t_0 values to $0.20 \pm 0.01\,\mu m^2/s$ and -36.5 ± 5.4 ms, respectively. This decrease suggests that the barriers confining TfR-GFP were reinforced by jasplakinolide treatment.

By contrast, it is noteworthy that neither the actin-based skeleton alterations induced by latrunculin B nor its stabilization by jasplakinolide had any effect on the molecular confinement observed with the GPI-anchored proteins and the sphingolipid analogs (Figures 5 and 6). Neither the t_0 nor D_{eff} values were affected under the experimental conditions that drastically altered the diffusion of TfR-GFP.

Meshwork and discrete domains contribute concomitantly to the dynamic compartmentalization of transmembrane proteins in the cell membrane

The shape of the diffusion law curve obtained for DPP_{IV}-GFP suggested that confinement by discrete domains may have occurred since, as observed in the case of GPI-anchored proteins, t_0 was positive. However, a similar study to that carried out on TfR-GFP showed that the FCS diffusion law was actin-dependent (Figure 7E). Treatment with latrunculin B or cytochalasin D led to increases in both t_0 and D_{eff}, whereas jasplakinolide treatment decreased both t_0 and D_{eff}, and even led to a negative t_0 value. More intriguingly, although TfR-GFP and DPP_{IV}-GFP were obviously sensitive to cytoskeleton-based compartmentalization, the possibility that discrete domain confinement may have occurred was

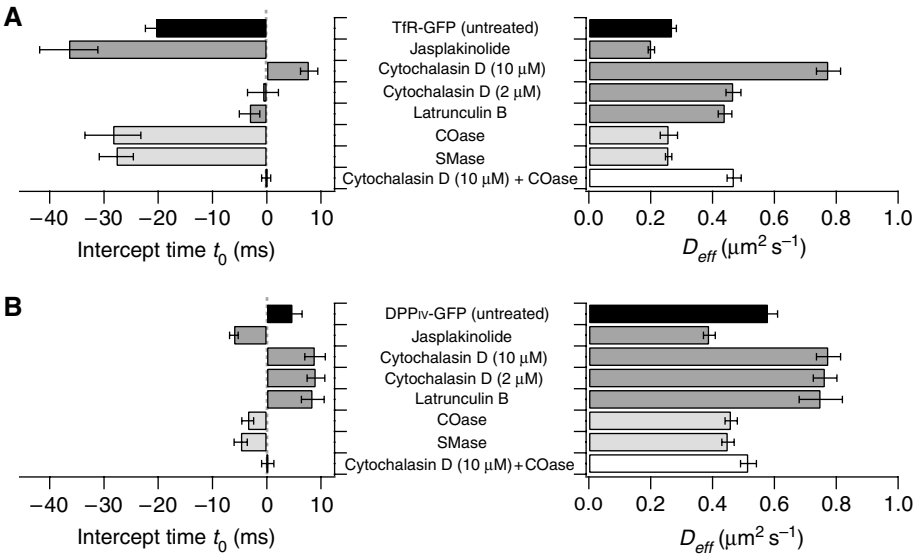

Figure 8 Both actin meshwork and lipid domains contribute to transmembrane protein compartmentalization. Time intercept t_0 and effective diffusion coefficient D_{eff} obtained with TfR-GFP (**A**) and DPP_{IV}-GFP (**B**) in untreated COS-7 cells (black bars), after applying cytoskeleton drug treatment (dark gray bars), after lipid modifications (light gray bars) or combined treatment (open bars). COase and SMase concentrations were 1 and 0.1 U/ml, respectively. Error bars are the s.d.s of the means.

suggested by the fact that high drug concentrations (cytochalasin D 10 μM) disrupted the actin network organization and gave a t_0 of 7.8 ± 1.6 and 8.9 ± 1.9 ms, respectively. In addition, the lipid modifications induced by COase or SMase systematically decreased the respective t_0 values (Figure 8). These two findings suggest that both meshwork and isolated domains contributed simultaneously to the DPP_{IV}-GFP and TfR-GFP diffusion process. To test this hypothesis, we then established the corresponding FCS diffusion laws under experimental conditions where actin-based cytoskeleton barriers and cholesterol were simultaneously modified (Figure 8). Significantly, τ_d for DPP_{IV}-GFP and TfR-GFP was found to be linear in w^2. Thus, when both confinement forces were relaxed, these proteins recovered free-like diffusion behavior.

Our study also indicated that the microdomain and the meshwork confinement may mask each other in the FCS law analysis. Indeed, we could interpret the differences in the diffusion modes between TfR-GFP and DPP_{IV}-GFP in terms of the differential strength of the actin-based and lipid-dependent confinement processes. COase and SMase treatments both abolished the lipid-dependent confinement process but unraveled the cytoskeleton-dependent one, which was in turn abolished by cytochalasin D or latrunculin B (Figure 8). With these TfR-GFP and DPP_{IV}-GFP proteins, COase treatment decreased the t_0 values to -28.4 ± 5.2 and -3.5 ± 1.1 ms, respectively. It was therefore deduced that the confinement of the cytoskeleton was about eight times stronger with TfR-GFP than DPP_{IV}-GFP. On the opposite, upon impairing the actin network, it was observed that both proteins underwent an almost identical weak lipid-dependent microdomain confinement process (7.8 ± 1.6 and 8.9 ± 1.9 ms for TfR-GFP and DPP_{IV}-GFP, respectively). It seems likely that the effects of cytoskeleton and lipid confinement may have been additive, but this hypothesis remains to be confirmed in further studies. The actin-based confinement process was stronger than the lipid-dependent one in the case of TfR-GFP, whereas the reverse was true in that of DPP_{IV}-GFP.

Discussion

The present study describing the diffusion behavior of diverse membrane components provides insights on the role of lipids in compartmentalizing the cell membrane. First, based on FCS data obtained on various spatial scales, we established that the sphingolipid analogs and GPI-anchored proteins undergo transient confinements in isolated microdomains. Secondly, the molecular origin of these confinement processes was found to be cholesterol- and sphingomyelin-dependent. Thirdly, their compartmentalization in isolated domains is independent of the actin-based cytoskeleton organization. Lastly, when the actin-based cytoskeleton confinement processes are relaxed, the contribution of lipid-dependent microdomains to confining transmembrane proteins was also readily observed. Overall, our data provide strong evidence supporting the idea that in live cells, a lipid-dependent microdomain organization is responsible for the dynamic molecular confinement of membrane components.

FCS diffusion laws provide a robust experimental frame of analysis for investigating the presence of submicron domains in live cells

Among the methods used to characterize the cell membrane, our novel experimental approach constitutes a significant advance, since it can be used to quantify relevant parameters to explore domain structure in the plasma membrane. Although FRAP and FCS methods involve similar experimental setups, the FCS method provides unique information, mainly because it combines high temporal resolution with single molecule sensitivity and robust statistical analysis (Schwille *et al*, 1999; Bacia *et al*, 2004). By comparison, the FRET methods frequently used to study membrane domains probe direct molecular interactions (Kenworthy and Edidin, 1998; Sharma *et al*, 2004), but these methods are not appropriate for studying long-range interactions and diffusive processes. SPT certainly competes with FCS, since it can be used to determine particle positions to within tens of nm and

in some cases, with a high temporal resolution (Schutz *et al*, 2000; Fujiwara *et al*, 2002). However, accurate interpretation of the SPT results generally requires analyzing large numbers of individual trajectories. Besides, in our FCS experiments, the direct conjugation of the fluorophore on the tracked molecules circumvents unwanted crosslinking and aggregation. Overall, the FCS approach described here for recording measurements on different spatial scales provides a highly appropriate means of exploring domain structure and dynamics in the plasma membranes of live cells.

The diffusion behavior of different subclasses of membrane components was determined here experimentally. Although the sphingolipid analogs show a lower affinity for DRMs than their natural counterparts (our data and Kuerschner *et al*, 2005), they are still useful to probe lipid raft organization, since FCS is sufficiently sensitive to be able to detect even small amounts of the fluorescent molecules in the coexisting phase (Korlach *et al*, 1999). The wide range of time intercepts t_0 measured (from -20 to $+20$ ms) suggests that different mechanisms may hinder the diffusion of membrane components. Based on our previous simulations (Wawrezinieck *et al*, 2005), these findings indicated that a strictly positive time intercept t_0 resulted from confinement into isolated domains, whereas a strictly negative value reflected the presence of a meshwork. It is significant that the components thought to be associated with lipid rafts, such as GPI-anchored proteins or sphingolipid analogs, showed strictly positive time intercepts, which suggests that a dynamic process of molecular partition into discrete domains mainly hinders their diffusion. By contrast, barriers predominantly impede the diffusion of the TfR-GFP since t_0 was strictly negative. Owing to the null t_0, the glycerophospholipid analogs apparently underwent unhindered diffusion.

Evidence supporting a lipid-dependent microdomain organization in live cells

A clearly visible signature of lipid-dependent compartmentalization is provided by COase and SMase enzymatic treatments. Our finding is consistent with previous data showing that both cholesterol and SM make a pivotal structural contribution to order domain formation (Brown and London, 1998; Rietveld and Simons, 1998). These results indicate that the lipid-dependent microdomain organization dictates the overall mobility of sphingolipid analogs and GPI-anchored proteins. It is also worth pointing out that the microdomains detected in the present study do actually exist in the plasma membrane of cells under steady-state conditions. This observation is in line with recently published data showing that phase separation and the formation of lipid domains do in fact occur in live cells (Meder *et al*, 2006).

Although an actin-based system of cytoskeleton compartmentalization has been described in the case of molecules located in the outer leaflet of the plasma membrane (Sako and Kusumi, 1994; Fujiwara *et al*, 2002; Kusumi *et al*, 2005), no such system was observed here in the mode of confinement of GPI-anchored proteins or sphingolipid analogs. Indeed, although cholesterol and SM modifications completely abolished the membrane confinement for these molecules, neither the actin-based cytoskeleton disorganization nor its stabilization had any such effects. Further studies are now required to determine whether the above discrepancies may be attributable to differences in the cell types, experimental conditions or techniques used. Our results are nevertheless in agreement with those of SPT analyses performed on GPI-anchored MHC class I and DiI molecules (Vrljic *et al*, 2005) as well as with the finding that cholesterol and/or SM modifications reduced the molecular mobility (Kenworthy *et al*, 2004; Nishimura *et al*, 2005; Vrljic *et al*, 2005).

The free diffusion behavior observed in the case of the glycerophospholipid analogs is similar to that previously observed in the case of Cy3-DOPE in the plasma membrane of various cell types at a recording rate of 100 ms/frame (Fujiwara *et al*, 2002; Kusumi *et al*, 2005). However, we were unable to detect any submicron-sized compartments such as those previously observed by authors performing SPT at an enhanced time resolution (25 μs/frame) using gold-tagged Cy3-DOPE molecules to label COS-7 cells (Kusumi *et al*, 2005).

A lipid-dependent microdomain organization also impedes the diffusion of transmembrane proteins

Our data clearly confirm the existence of fences confining transmembrane proteins, even if these molecules are not interacting directly with the cytoskeleton. For instance, the motion of TfR-GFP is mainly controlled by the actin-based membrane skeleton fences, and t_0 decreased when this meshwork was strengthened. It is also worth noting that all these experimental FCS diffusion laws form a bundle of lines with a common crossover point (Figure 7D). Previous simulations have shown that (i) these lines intersect at a single point in the meshwork at different barrier strengths but with the same mesh sizes; (ii) the crossover occurs when the spot area is about one to twice that of the mesh. Since the experimental crossover was obtained with $w^2 = 5 \times 10^4 \pm 1 \times 10^4$ nm^2, the area of the mesh was around $8 \times 10^4 \pm 2 \times 10^4$ nm^2. Assuming a square mesh, its sides would measure 240 ± 60 nm: this value is in good agreement with the 260 nm mesh size measured in rat kidney fibroblasts, which was determined by SPT experiments performed at 25 μs/image (Fujiwara *et al*, 2002). However, in our case, we did not detect any enlarged meshes after a partial disruption of the cytoskeleton. In addition, we observed that a treatment by cytochalasin D at 10 μM released TfR-GFP and DPP_{IV}-GFP proteins from the meshwork-based state of confinement. Nevertheless, the latter proteins still underwent the lipid domain-based constrained diffusion on a much smaller compartmentalization scale.

Some extremely interesting features have been brought to light by monitoring the motion of these proteins after subjecting them to treatments that disrupt the actin-based cytoskeleton and/or decrease the membrane cholesterol level. This combined treatment applied here induced the recovery of an FCS diffusion law curve, which intercepted the time origin. A single treatment abolishing one of the two major hindrance mechanisms served to show up the other one.

Main features of lipid-dependent microdomains

Our observations of the sphingolipid and cholesterol dependency for the lipid-dependent microdomains revealed by the FCS diffusion study suggest that they correspond to lipid rafts, a type of microdomains proposed to be involved in numerous cellular functions, but whose existence has been matter of controversy. The current view is that 'membrane

rafts are small (10–200 nm), heterogeneous, highly dynamic, sterol- and sphingolipid-enriched domains that compartmentalize cellular processes' (Pike, 2006). The analysis of our experimental data in the light of the simulation studies allow us to further conclude that the lipid-mediated microdomains described here fit the above description very nicely in many respects.

As mentioned above, our FCS method is sensitive to nanoscale confining structures. Based on dynamic molecular partition simulations, we were able to determine the upper limit of the microdomain radius r (Supplementary Figure S1). We previously observed that the graph line between τ_d and w^2 is solely observed if the observation spot is significantly larger than the domains ($w^2/r^2 > 10$ in the case of isolated microdomains) (Wawrezinieck *et al*, 2005). In our experiments, the smallest observation spot was close to the transverse resolution limit of the microscope ($\sim$200 nm); the upper limit of the microdomain radius r is therefore around 60 nm: this value is consistent with data published in the literature (Pralle *et al*, 2000; Zacharias *et al*, 2002; Prior *et al*, 2003; Sharma *et al*, 2004).

The t_0 intercept could be of special interest, since it could be used to delineate the temporal characteristics of these microdomains. In the simulation models, this value depends on both the partition factor α of a given molecule in the microdomains and the confinement time within one microdomain τ_{conf} (see equation (2) in the Supplementary data). The value of α is not yet available, but based on DRM experiments, we might tentatively take this value to range between 10 and 30%. For instance, with a t_0 value of 18.4 ms in the case of GFP-Thy1, we have 31 ms $< (\tau_{conf} - \tau_d^{domain}) <$ 92 ms. Since we measured that $\tau_d > 30$ ms when $(w/r)^2 > 10$, the diffusion time in a domain should be at most 30/10 $\sim$ 3 ms. It can therefore be concluded that τ_{conf} ranges between 34 and 95 ms. Confinement in microdomains is therefore an extremely transient process taking probably only some tens to hundreds of milliseconds. Reaching a deeper understanding of t_0 obviously constitutes one of most important and challenging issues awaiting future theoretical analysis. Our experiments showed (Figures 5 and 6) that before reaching the maximum effect (i.e. $t_0 \sim$ null), a parallel existed between the change in the sphingomyelin or cholesterol levels and the decrease in t_0. It is therefore possible to consider this parameter as a *microdomain confinement index,* since the partition factor α and the confinement time τ_{conf} are essential parameters characterizing the confinement into microdomains.

We would like to stress the fact that our results do not tell us whether membrane molecules partition dynamically into pre-existing raft domains or whether they directly participate in assembly/disassembly of the domains forming self-promoting membrane complexes. This is because the confinement time τ_{conf} is always to be either shorter than or equal to the lifetime of the microdomain in our models. In the first case, the molecule is partitioning dynamically into a pre-existing domain, whereas in the second case, the molecule accompanies/participates in the assembly and disassembly of the domain. In the same context, we observed in our FCS measurements that the diffusion time τ_d remained constant within the limits of the experimental error bars although the amount of fluorescent probe used varied by a factor of 20 (i.e. from $\sim$100 to $\sim$2000 μm^{-2} in the case of GFP-GPI) (Supplementary Figure S2). Consequently, the probe concentration does not greatly affect the diffusion behavior of the probe. However, this is not relevant to the question as to whether we are dealing with pre-existing or self-assembling raft models, because our FCS analysis did not include the probe density, contrary to recent FRET and immuno-EM studies on nanoscale membrane organization (Sharma *et al*, 2004; Hess *et al*, 2005; Plowman *et al*, 2005).

Overall, our data strongly support a dynamic picture where nanometer-scale microdomains confine constituents for up to a few tens to hundreds of milliseconds and undergo continuous changes as molecular diffusion processes occur. These findings also show that studies on diffusion behavior throw particularly useful light on the modes of lateral membrane organization, which are likely to be largely governed by weak molecular interactions.

Materials and methods

DNA constructs and cell transfection procedures

GFP-GPI was provided by A LeBivic (IBDM, Marseille, France). DPP_{IV}-GFP was obtained from G Trugnan (INSERM, Paris, France). The human TfR cDNA was provided by S Méresse (CIML, Marseille, France). The Thy1 gene expression vector and the Alexa488-conjugated anti-Thy1 Fab fragment were a kind gift from R Morris (King's College London, UK). To construct GFP-Thy1, three overlapping fragments were PCR amplified and cloned into the pEGFP-C1 plasmid. This yielded a recombinant GFP-Thy1 cDNA encoding the 19th aa of Thy1 (signal peptide), the EGFP and the remaining sequence of Thy1 (aa 20–162). To construct TfR-GFP, the TfR cDNA (aa 1–112) was cloned inframe with the GFP cDNA into the pEGFP-N3 plasmid.

All experiments were carried out on COS-7 cells (ATCC, CRL-1657). Cells were grown in DME supplemented with 10% FCS, glutamine and sodium pyruvate. Transient transfections were performed with ExGen 500 as per the manufacturer's instructions (Euromedex) and 24 h before FCS measurements.

Fluorescent staining with lipid analogs

Complexes of BODIPY-lipids (Invitrogen) and BSA were prepared in line with the manufacturer's instructions and as described in Martin and Pagano (1994). Briefly, 500 nmol of FL-SM or FL-GM1 stock solution ($CHCl_3$:MeOH 19:1) were dried under a stream of nitrogen, and then under a vacuum for at least 1 h. The dried lipid was dissolved in 200 µl of absolute ethanol and injected into 10 ml of defatted BSA solution (5 µM defatted BSA in Hanks buffered salt solution containing 10 mM HEPES pH 7.4, HBSS/HEPES) while vortexing vigorously. FL-PC and FL-PE were prepared in a similar way, except that the lipid to BSA ratio was 2:1 (mol:mol). Cell cultures were washed in HBSS/HEPES, incubated with 0.05 µM lipid/BSA complex in HBSS/HEPES for 30 min at 4°C, washed and further incubated in HBSS/HEPES at 37°C.

Treatment of cells with enzymes and drugs

To modify the cholesterol or sphingomyelin contents of plasma membrane, cells were treated with *Streptomyces* sp. COase or *Staphylocuccus aureus* SMase (Calbiochem) in serum-free HBSS/HEPES buffer at 1 U/ml for 30 min or at 0.1 U/ml for 5 min, respectively. Cells were washed in HBSS/HEPES prior to the diffusion measurements. Prior to pharmacological treatments, cells were washed in HBSS/HEPES and incubated at 37°C with 1 µM latrunculin B (5 min), 2–10 µM cytochalasin D (30 min) or 0.4 µM jasplakinolide (5 min). All FCS measurements were completed within 30 min of the cell treatment, before any significant morphological changes in the cell could take place.

Biochemical analyses

To determine the cholesterol levels, cells were scraped off and lyzed at 4°C for 30 min in a buffer containing 1% Nonidet P-40, 10 mM Tris pH 7.4, 150 mM NaCl, 1 mM EDTA and protease inhibitors. Samples were cleared by centrifugation at a rate of 12 000 *g* before

undergoing fluorometric measurements using the Amplex®Red Cholesterol kit (Invitrogen).

To determine the sphingomyelin levels, a similar procedure was used, except that the cells were lyzed at 4°C by sonication and the PNS harvested by centrifugation. Lipid extraction was performed using the Bligh–Dyer method (Bligh and Dyer, 1959) and the sphingomyelin levels were determined using a fluorometric method with the Amplex®Red sphingomyelinase assay kit (Invitrogen) as described in He *et al* (2002). With each test sample, a negative control assay was run on the sample and the reaction mixture devoid of SMase. Sphingomyelin amounts were calculated from the difference in fluorescence between the test and control samples, and compared with a standard.

To isolate DRMs, Brij98 (1%) solubilized postnuclear supernatant was fractionated on the sucrose gradient by centrifugation at 38 000 r.p.m. for 16 h in a SW41 rotor (Beckman Instruments Inc.) (Drevot *et al*, 2002). Fractions were resolved on SDS–PAGE and blotted with anti-GFP mAbs (Roche Molecular Biochemicals). The presence of DRMs was monitored, based on the distribution of Rab5 and ganglioside G_{M1} over the sucrose gradient. Spectrofluorimetry measurements were performed on the different fractions of the lipid analogs.

Fluorescence microscopy, FCS measurements and numerical analysis

Details of the experimental fluorescence microscopy, FRAP, FCS and numerical analysis procedures used are given in the Supplementary data, as well as in previous studies (Kenworthy *et al*, 2004; Wawrezinieck *et al*, 2004, 2005).

Supplementary data

Supplementary data are available at *The EMBO Journal* Online.

Acknowledgements

We thank R Morris, M Edidin, A Lellouch and P Golstein, for helpful discussions and suggestions and for critically reviewing the manuscript, J Blanc for editing the English. R Morris, A LeBivic, G Trugnan and S Méresse generously provided reagents and the use of the PICsL imaging core facility and technical assistance. This research was supported by institutional grants from INSERM and CNRS, and by specific grants from FRM, MENRT, EU FEDER and CNRS. LW and FC have been awarded fellowships from the MENRT.

References

Bacia K, Scherfeld D, Kahya N, Schwille P (2004) Fluorescence correlation spectroscopy relates rafts in model and native membranes. *Biophys J* **87:** 1034–1043

Bligh EG, Dyer WJ (1959) A rapid method of total lipid extraction and purification. *Can J Biochem Physiol* **37:** 911–917

Brown DA, London E (1998) Functions of lipid rafts in biological membranes. *Annu Rev Cell Dev Biol* **14:** 111–136

Drevot P, Langlet C, Guo XJ, Bernard AM, Colard O, Chauvin JP, Lasserre R, He HT (2002) TCR signal initiation machinery is preassembled and activated in a subset of membrane rafts. *EMBO J* **21:** 1899–1908

Edidin M (2003) The state of lipid rafts: from model membranes to cells. *Annu Rev Biophys Biomol Struct* **32:** 257–283

Fujiwara T, Ritchie K, Murakoshi H, Jacobson K, Kusumi A (2002) Phospholipids undergo hop diffusion in compartmentalized cell membrane. *J Cell Biol* **157:** 1071–1081

Gaus K, Gratton E, Kable EP, Jones AS, Gelissen I, Kritharides L, Jessup W (2003) Visualizing lipid structure and raft domains in living cells with two-photon microscopy. *Proc Natl Acad Sci USA* **100:** 15554–15559

He X, Chen F, McGovern MM, Schuchman EH (2002) A fluorescence-based, high-throughput sphingomyelin assay for the analysis of Niemann–Pick disease and other disorders of sphingomyelin metabolism. *Anal Biochem* **306:** 115–123

Hess ST, Kumar M, Verma A, Farrington J, Kenworthy A, Zimmerberg J (2005) Quantitative electron microscopy and fluorescence spectroscopy of the membrane distribution of influenza hemagglutinin. *J Cell Biol* **169:** 965–976

Kenworthy AK, Edidin M (1998) Distribution of a glycosylphosphatidylinositol-anchored protein at the apical surface of MDCK cells examined at a resolution of <100 A using imaging fluorescence resonance energy transfer. *J Cell Biol* **142:** 69–84

Kenworthy AK, Nichols BJ, Remmert CL, Hendrix GM, Kumar M, Zimmerberg J, Lippincott-Schwartz J (2004) Dynamics of putative raft-associated proteins at the cell surface. *J Cell Biol* **165:** 735–746

Korlach J, Schwille P, Webb WW, Feigenson GW (1999) Characterization of lipid bilayer phases by confocal microscopy and fluorescence correlation spectroscopy. *Proc Natl Acad Sci USA* **96:** 8461–8466

Kuerschner L, Ejsing CS, Ekroos K, Shevchenko A, Anderson KI, Thiele C (2005) Polyene-lipids: a new tool to image lipids. *Nat Methods* **2:** 39–45

Kusumi A, Ike H, Nakada C, Murase K, Fujiwara T (2005) Single-molecule tracking of membrane molecules: plasma membrane compartmentalization and dynamic assembly of raft-philic signaling molecules. *Semin Immunol* **17:** 3–21

Marguet D, Lenne PF, Rigneault H, He HT (2006) Dynamics in the plasma membrane: how to combine fluidity and order. *EMBO J* [E-pub ahead of print: 22 June 2006; doi:10.1038/sj.emboj.7601204]

Marguet D, Spiliotis ET, Pentcheva T, Lebowitz M, Schneck J, Edidin M (1999) Lateral diffusion of GFP-tagged H2Ld molecules and of GFP-TAP1 reports on the assembly and retention of these molecules in the endoplasmic reticulum. *Immunity* **11:** 231–240

Martin OC, Pagano RE (1994) Internalization and sorting of a fluorescent analogue of glucosylceramide to the Golgi apparatus of human skin fibroblasts: utilization of endocytic and nonendocytic transport mechanisms. *J Cell Biol* **125:** 769–781

Meder D, Moreno MJ, Verkade P, Vaz WL, Simons K (2006) Phase coexistence and connectivity in the apical membrane of polarized epithelial cells. *Proc Natl Acad Sci USA* **103:** 329–334

Megha, London E (2004) Ceramide selectively displaces cholesterol from ordered lipid domains (rafts): implications for lipid raft structure and function. *J Biol Chem* **279:** 9997–10004

Munro S (2003) Lipid rafts: elusive or illusive? *Cell* **115:** 377–388

Nishimura SY, Vrljic M, Klein LO, McConnell HM, Moerner WE (2005) Cholesterol depletion induces solid-like regions in the plasma membrane. *Biophys J* **90:** 927–938

Pike LJ (2006) Rafts defined. *J Lipid Res* [E-pub ahead of print: 27 April 2006; doi:10.1194/jlr.E600002-JLR200]

Plowman SJ, Muncke C, Parton RG, Hancock JF (2005) H-ras, K-ras, and inner plasma membrane raft proteins operate in nanoclusters with differential dependence on the actin cytoskeleton. *Proc Natl Acad Sci USA* **102:** 15500–15505

Pralle A, Keller P, Florin EL, Simons K, Horber JK (2000) Sphingolipid-cholesterol rafts diffuse as small entities in the plasma membrane of mammalian cells. *J Cell Biol* **148:** 997–1008

Prior IA, Muncke C, Parton RG, Hancock JF (2003) Direct visualization of Ras proteins in spatially distinct cell surface microdomains. *J Cell Biol* **160:** 165–170

Rietveld A, Simons K (1998) The differential miscibility of lipids as the basis for the formation of functional membrane rafts. *Biochim Biophys Acta* **1376:** 467–479

Sako Y, Kusumi A (1994) Compartmentalized structure of the plasma membrane for receptor movements as revealed by a nanometer-level motion analysis. *J Cell Biol* **125:** 1251–1264

Saxton MJ (2005) New and notable: fluorescence corralation spectroscopy. *Biophys J* **89:** 3678–3679

Schutz GJ, Kada G, Pastushenko VP, Schindler H (2000) Properties of lipid microdomains in a muscle cell membrane visualized by single molecule microscopy. *EMBO J* **19:** 892–901

Schwille P, Haupts U, Maiti S, Webb WW (1999) Molecular dynamics in living cells observed by fluorescence correlation spectroscopy with one- and two-photon excitation. *Biophys J* **77:** 2251–2265

Sharma P, Varma R, Sarasij RC, Ira, Gousset K, Krishnamoorthy G, Rao M, Mayor S (2004) Nanoscale organization of multiple GPI-anchored proteins in living cell membranes. *Cell* **116:** 577–589

Shvartsman DE, Kotler M, Tall RD, Roth MG, Henis YI (2003) Differently anchored influenza hemagglutinin mutants display distinct interaction dynamics with mutual rafts. *J Cell Biol* **163:** 879–888

Simons K, Ikonen E (1997) Functional rafts in cell membranes. *Nature* **387:** 569–572

Simons K, Vaz WL (2004) Model systems, lipid rafts, and cell membranes. *Annu Rev Biophys Biomol Struct* **33:** 269–295

van Meer G (2005) Cellular lipidomics. *EMBO J* **24:** 3159–3165

Vrljic M, Nishimura SY, Moerner WE, McConnell HM (2005) Cholesterol depletion suppresses the translational diffusion of class II major histocompatibility complex proteins in the plasma membrane. *Biophys J* **88:** 334–347

Wawrezinieck L, Lenne P-F, Marguet D, Rigneault H (2004) Fluorescence correlation spectroscopy to determine diffusion laws: application to live cell membranes. *Proc SPIE* **5462:** 92–102

Wawrezinieck L, Rigneault H, Marguet D, Lenne P-F (2005) Fluorescence correlation spectroscopy diffusion laws to probe the submicron cell membrane organization. *Biophys J* **89:** 4029–4042

Xu X, London E (2000) The effect of sterol structure on membrane lipid domains reveals how cholesterol can induce lipid domain formation. *Biochemistry* **39:** 843–849

Yechiel E, Edidin M (1987) Micrometer-scale domains in fibroblast plasma membranes. *J Cell Biol* **105:** 755–760

Zacharias DA, Violin JD, Newton AC, Tsien RY (2002) Partitioning of lipid-modified monomeric GFPs into membrane microdomains of live cells. *Science* **296:** 913–916

Chapitre 3

Structures photoniques et applications biologiques, 2000-2006

Sommaire

Lorsque j'ai débuté mes activités à l'Institut Fresnel en octobre 2000, Hervé Rigneault et moi avons porté nos efforts sur le renforcement et le contrôle de la fluorescence à l'aide de structures optiques pour la détection de molécules biologiques individuelles et la réduction des volumes d'observation.

À l'époque, nous étions encore dans l'euphorie du domaine des molécules individuelles, mais les voir ne suffisait déjà plus, il fallait les voir mieux !

La question était importante pour les applications biologiques car le fond de fluorescence endogène dans les cellules est assez fort et les fluorophores utilisés pour le marquage sont souvent peu stables.

3.1 Miroirs diélectriques

J'ai tout d'abord travaillé sur l'utilisation de miroirs diélectriques, structures simples et robustes, et donc *a priori* faciles à mettre en œuvre dans des expériences

de biologie. Sur ce sujet, j'ai co-encadré avec Hervé Rigneault la thèse d'Émilien Etienne, soutenue en décembre 2003.

La méthode que nous avons proposée consiste à placer un miroir dans le plan de focalisation d'un objectif, afin de réfléchir les faisceaux d'excitation et d'émission [25, 19] (Figure 3.1). L'interférence des faisceaux excitateurs incident et réfléchi conduit à une modulation axiale de l'intensité d'excitation de période $\lambda/2$, où λ est la longueur d'onde du faisceau excitateur dans le milieu. Lorsque des molécules fluorescentes diffusent à travers le volume de collection, elles émettent un signal de fluorescence fluctuant au cours du temps. Le passage d'une molécule à travers une frange claire s'accompagne d'une fluctuation dont la durée dépend de l'interfrange et du coefficient de diffusion moléculaire. L'analyse temporelle de ces fluctuations par FCS donne accès à une mesure absolue du coefficient de diffusion des objets diffusants (protéines, lipides...) à travers le volume confocal, indépendante de la géométrie du faisceau focalisé. En outre, le miroir a pour effet de rediriger la fluorescence vers l'objectif de microscope et conduit à une exaltation du signal collecté (>4). Ces travaux ont donné lieu au dépôt d'un brevet [27].

En 2003, j'ai proposé de mettre à profit ces structures optiques pour mesurer la diffusion confinée de protéines dans le cytoplasme de cellules de petite taille. Je travaillais alors sur le confinement membranaire et avais mis en place les simulations de diffusion en géométrie confinée. Dans ce but, nous avons collaboré avec James Sturgis, spécialiste de l'organisation membranaire des bactéries E. Coli (Institut de Biologie Structurale et Microbiologie, Marseille). Nous avons démontré expérimentalement et numériquement que la mesure de diffusion dans les franges permet de déterminer le coefficient de diffusion de molécules se déplaçant dans des volumes de petite taille [3] : alors que l'analyse classique de FCS ne s'applique que lorsque la taille caractéristique l du réservoir est dix fois plus grand que celle le volume d'observation ($l > 10 \times \lambda$), la méthode avec miroir est valide dès que $l > \lambda/2$.

3.2 Ouvertures nanométriques dans un film métallique

3.2.1 Exaltation de la fluorescence

La mise en forme des volumes d'excitation et de détection peut également s'appuyer sur la structuration transverse des matériaux grâce à l'introduction de "défauts" de petite taille. En 2003, nous nous sommes tournés vers des structures sub-longueur d'onde, et plus particulièrement des trous nanométriques percés dans un film métallique, pour réduire les volumes d'observation et avec l'espoir de renforcer les champs

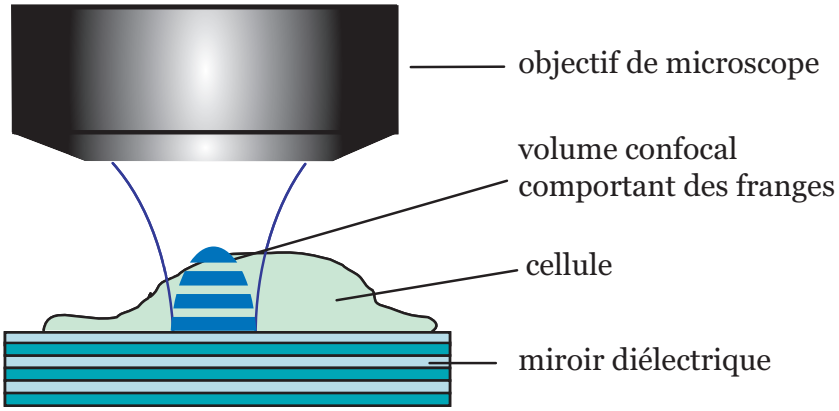

FIG. 3.1 – Schéma du dispositif de détection exaltée à l'aide d'un miroir diélectrique. Le miroir réfléchit à la fois le faisceau excitateur et la lumière de fluorescence. Il en résulte une modulation axiale de l'intensité d'excitation et une augmentation de l'efficacité de détection moléculaire.

lumineux. Largement étudiés pour leurs propriétés remarquables de transmission en champ lointain[4], peu de chose était connu alors sur leurs propriétés électromagnétiques locales. Nous avons proposé d'utiliser des molécules fluorescentes pour sonder localement le champ lumineux dans ces nanostructures et mesurer le couplage émetteur dipolaire - nanostructure. Pour cela, nous étudions l'émission de fluorescence de molécules individuelles diffusant dans des trous nanométriques isolés (Figure 3.2). Ces nanotrous peuvent être circulaires ou rectangulaires, et possèdent des dimensions inférieures à la longueur d'onde optique. Les structures sont fabriquées par le groupe de T. W. Ebbesen de l'Institut des Sciences et Ingénieries Supramoléculaires (ISIS) de Strasbourg.

La méthode de FCS nous permet de quantifier le nombre moyen de molécules observées et le nombre moyen de photons détectés par émetteur. Nous avons démontré ainsi qu'un trou nanométrique permet d'exalter la fluorescence de molécules individuelles d'un facteur significatif environ égal à 6.5 pour une structure circulaire optimisée [14].

Nous avons cherché à comprendre l'origine de cette exaltation de la fluorescence, ce qui nous a amené à différentes études à la fois théoriques et expérimentales (en collaboration avec l'équipe CLARTE de l'Institut Fresnel). Hors saturation du fluorophore, nous montrons que l'essentiel du phénomène d'exaltation peut s'expliquer

[4]Ebbesen TW, Lezec HJ, Ghaemi HF, Thio T, Wolff PA : Extraordinary Optical Transmission through Sub-Wavelength Hole Arrays. Nature 1998, 391 :667-669.

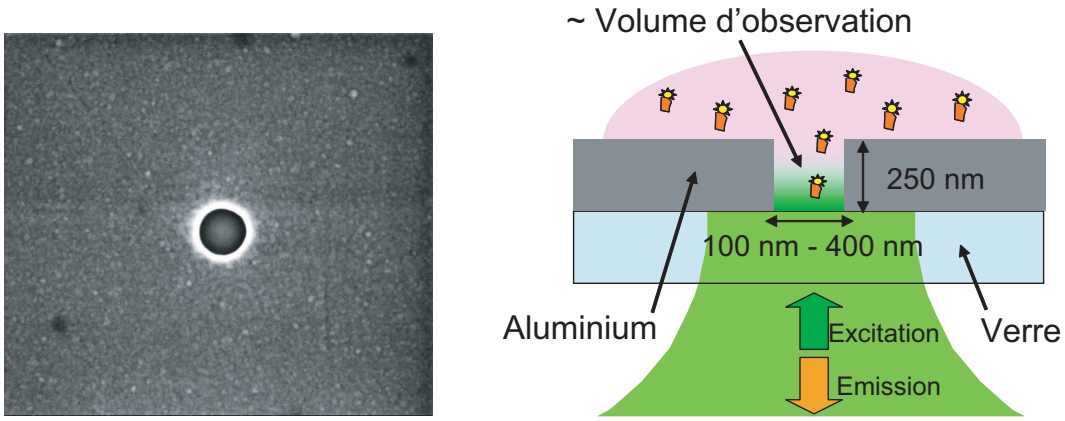

FIG. 3.2 – Micrographe électronique d'un nanotrou de diamètre 200 nm et schéma expérimental

une augmentation locale de l'intensité d'excitation. Cette exaltation du champ excitateur intervient au voisinage de la coupure du mode fondamental pouvant se propager dans le guide formé par le nanotrou. De manière surprenante, aucune résonance avec un plasmon de surface n'est alors mise en jeu (absence de mode électromagnétique propre à l'interface métallique). Par ailleurs, nous avons observé une réduction importante du temps de vie de la molécule (supérieure à 10), ainsi qu'un retard dans l'instauration de la saturation de la fluorescence. Cela traduit une modification des paramètres photophysiques de l'émetteur, notamment une augmentation du coefficient de couplage radiatif.

Un deuxième effet des nanotrous est de réduire fortement le volume d'analyse par rapport au volume standard obtenu en microscopie confocale, avec un facteur de réduction d'environ 400 pour des trous de 100 nm de diamètre. On peut ainsi contourner les limites imposées par la diffraction, et observer notamment des molécules individuelles dans des solutions de fortes concentrations[5] (une concentration élevée est une condition nécessaire pour l'étude des associations de faible affinité, les réactions enzymatiques en particulier).

3.2.2 La structure fine de la membrane révélée à l'aide des structures photoniques

Les trous sub-longueur d'onde peuvent-ils nous offrir la possibilité de sonder l'organisation membranaire sous la limite de diffraction et d'explorer les régimes de

[5]Levene MJ, Korlach J, Turner SW, Foquet M, Craighead HG, Webb WW : Zero-mode waveguides for single-molecule analysis at high concentrations. Science 2003, 299 :682-686.

diffusion inacessibles à nos mesures de FCS (voir chapitre 2) ? L'idée, séduisante a priori, valait d'être testée. Avec Jérôme Wenger (qui a rejoint notre équipe en octobre 2004), nous avons montré tout d'abord que le temps de diffusion d'une espèce, diffusant librement dans une membrane modèle, est proportionnelle à l'aire des ouvertures [11]. L'étape suivante a consisté à établir les lois de diffusion FCS sur des cellules vivantes à l'aide de trous de diamètres variables [1](Figure 3.3).

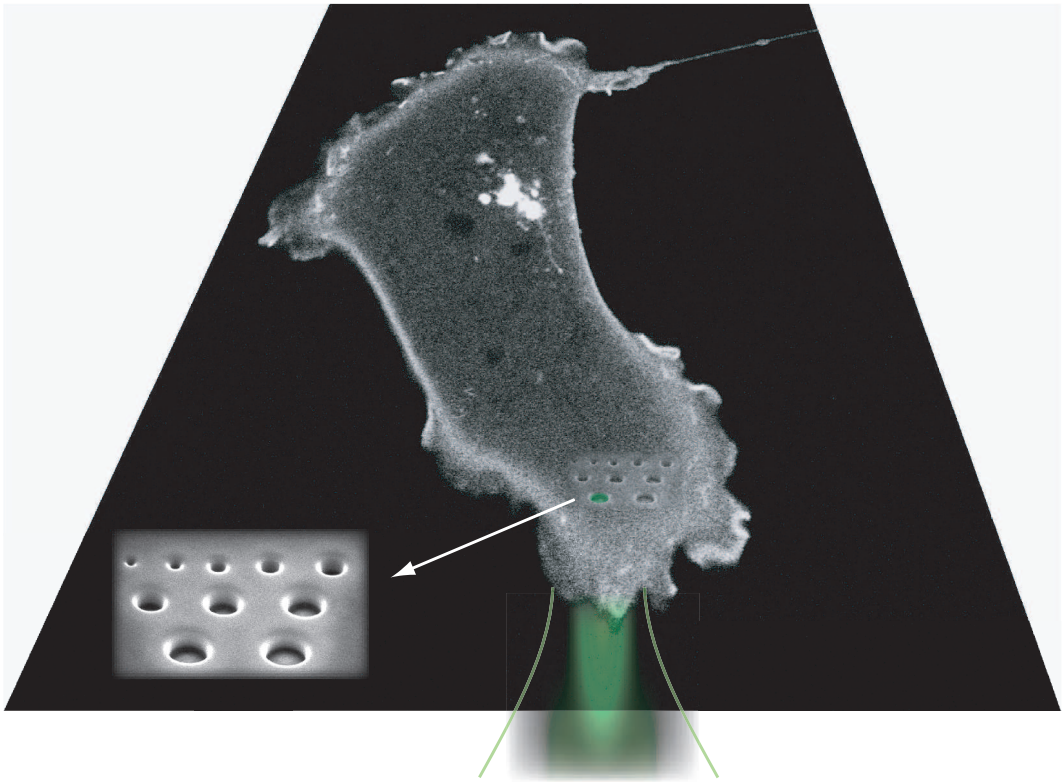

FIG. 3.3 – Une cellule déposée sur un film métallique percé d'ouvertures sub-longueur d'onde. Le diamètre des trous varient entre 100 et 450 nm. Pour l'illustration, les trous sont rapprochés alors qu'ils sont en réalité distants de plusieurs microns

On observe sous la limite de diffraction des régimes de transition à la diffusion normale, qui dépendent de la nature de la molécule étudiée. Les régimes de transition se produisent pour des tailles de trous proches de ceux des domaines de confinement, nous permettant de déterminer la taille des domaines membranaires.

Ces résultats renforcent non seulement les études réalisées au dessus la limite de diffraction mais ouvrent également la voie à des études fines de la diffusion dans les systèmes complexes, en particuliers membranaires.

Subwavelength patterns and high detection efficiency in fluorescence correlation spectroscopy using photonic structures

P.-F. Lenne,[a] E. Etienne, and H. Rigneault[b]
Institut Fresnel UMR CNRS 6133, Ecole Nationale Supérieure de Physique de Marseille, Domaine Universitaire Saint Jérôme, 13397 Marseille Cédex 20, France

(Received 27 November 2001; accepted for publication 9 April 2002)

We present theoretical and experimental evidence of subwavelength resolution and high detection efficiency in fluorescence correlation spectroscopy (FCS) using photonic structures. We show that multilayered dielectric mirrors or metallic mirrors may be used in a conventional FCS setup to improve fluorescence detection and fluctuation analysis. © *2002 American Institute of Physics.* [DOI: 10.1063/1.1483116]

Since the pioneering work of Orrit[1] and Moerner[2] on single molecules at cryogenic temperature, fluorescence spectroscopy has became the master tool for probing single-molecule properties in different environments. In particular, the analysis of temporal fluctuations of the fluorescence light is now a widely used method for studying diffusion of single molecules in solutions and in artificial or biological membranes. In fluorescence correlation spectroscopy (FCS),[3] the fluctuations arise from the number variation of fluorescently labeled molecules present in a collection volume V. This volume is generally defined by a far-field confocal microscopy setup and can be as small as 1 fl with a high numerical aperture (NA) microscope objective. The same objective collects the total emitted light with an efficiency up to 30% (1.2 NA, water immersion) while the total photon collection efficiencies range from 0.5% to 5% due to filtering and detector quantum efficiency. Although FCS is a very powerful technique to study single-molecule dynamics, it still presents two limitations: (1) quantitative analysis requires detailed knowledge of the geometry and dimensions of the collection volume V, which is usually difficult to obtain with the necessary accuracy; and (2) the collection efficiency of the fluorescence signal is in many cases too low to overcome the background noise and to allow fast analysis. To circumvent the first limitation, interference fringes can be produced to set a well-defined length scale. First suggested by Asai and Ando for FCS with standing waves,[4] this concept has been extended for dynamics study with traveling interference fringes.[5,6] The second limitation can be reduced with photonic structures.[7,8] For example, mirrors with high and broad reflectivity in the fluorophore emission band allow redirection of the emitted fluorescence signal towards the collection optics. The resulting fluorescence enhancement increases notably the signal-to-background ratio.

Here, we present a method combining these two concepts. By using a simple photonic structure, in particular a planar mirror, in a conventional FCS setup, we demonstrate that it is possible to (1) set a well-defined length scale in the collection volume, which permits accurate measurement of diffusion coefficients and (2) increases the collection efficiency, allowing fast analysis.

In a conventional FCS setup, an excitation laser beam is focused by a high NA lens [Fig. 1(a)]. The excitation intensity profile $I_e(\mathbf{r},z)$ is usually a Gaussian beam well defined by its lateral waist w_0, where $\mathbf{r}=(x,y)$ is the lateral coordinate and z is the distance away from the focal plane, so that $I_e(\mathbf{r},0)=I_0\exp(-2\mathbf{r}^2/w_0^2)$. Assuming a linear regime, any fluorescent particle intercepting the beam emits light with an intensity following this fundamental Gaussian profile. Usually, a pinhole is located in the image plane of the microscope lens (confocal setup), so that the detected intensity depends on the location and size of the point source image with respect to the pinhole. This effect is described using the fluorescence collection efficiency function CEF $(\mathbf{r},z)$, defined as the fraction of the light emitted by a point source that passes through the pinhole.[9] Although the exact computation of the CEF requires nontrivial Gaussian optics consideration in the objective lens, it has been shown that a semi-geometric approach gives excellent results.[10,11] As the overall collection intensity results both from the excitation and the collection, we define the molecule detection efficiency function MDE $(\mathbf{r},z)$ as:[10] MDE $(\mathbf{r},z)=$CEF $(\mathbf{r},z)\cdot I_e(\mathbf{r},z)$. The

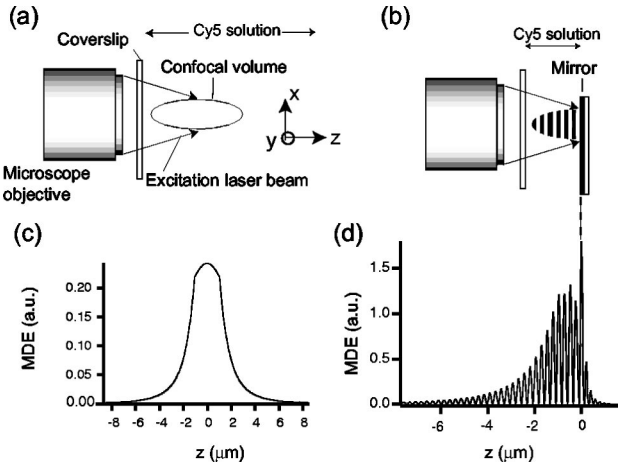

FIG. 1. (a) Standard confocal collection volume and (b) modified collection volume by a reflecting mirror placed at the focal point of the excitation beam. (c) and (d) computed $\mathrm{MDE}_m(\mathbf{0},z)$ for Cy5 molecules in (a) and (b) configurations, respectively (oil immersion objective 1 NA, pinhole diameter 50 μm, focal plane/pinhole plane magnification: 20, $w_0=0.5$ μm).

[a]Electronic mail: lenne@fresnel.fr
[b]Electronic mail: herve.rigneault@fresnel.fr

result is well approximated by a Gaussian distribution for the detected intensity:[10] MDE $(\mathbf{r},z)=M_0\exp(-2r^2/w_0^2)\exp(-2z^2/z_0^2)$, where z_0 is the axial radius resulting mostly from the pinhole z confinement.

When a flat broadband mirror is located at the focal point of the excitation beam and perpendicular to the optical axis [Fig. 1(b)] both $I_e(\mathbf{r},z)$ and CEF $(\mathbf{r},z)$ are affected. The coherent excitation beam, which is reflected, produces an interference pattern along the z optical axis with an interfringe spacing of $\lambda_0/2n$, where λ_0 is the excitation wavelength and n is the medium refractive index so that the new excitation intensity $I_{e,m}(\mathbf{r},z)$ becomes $I_{e,m}(\mathbf{r},z)\approx 4\cdot I_e(\mathbf{r},z)\cos^2(kz)$, where $k=2\pi/\lambda_0$. We have found that the latter expression is a good approximation of the exact electromagnetic computation for the intensity resulting from a focused Gaussian beam falling on a high reflecting dielectric or metallic mirror. The second expected mirror effect is a CEF alteration for the fluorescent particles located in the mirror vicinity. The main effect of the planar mirror is to redirect the emitted fluorescence[12] rather than to alter the emitter lifetime.[13] The result is a spatially dependent enhancement of the fluorescence light emitted into the objective numerical aperture and passing through the pinhole that we computed in two dimensions (2D) and for an aberration free objective using a modal analysis of spontaneous emission.[14] This leads to a new $\mathrm{CEF}_m(\mathbf{r},z)$ that we used to compute numerically the expected MDE in the presence of the mirror: $\mathrm{MDE}_m(\mathbf{r},z)=\mathrm{CEF}_m(\mathbf{r},z)\cdot I_{e,m}(\mathbf{r},z)$. Figures 1(c) and 1(d) show the computed $\mathrm{MDE}_m(\mathbf{0},z)$ for Cyanine 5 (Cy5) molecules in the absence and in the presence of a mirror, respectively, in a confocal setup (oil immersion objective 1 NA, pinhole diameter 50 μm, focal plane/pinhole plane magnification: 20, $w_0=0.5\,\mu$m). Cy5 molecules are considered as three-dimensional (3D) electromagnetic dipoles weighted over the Cy5 spectral bandwidth. They are uniformly distributed in bulk liquid [Fig. 1(a)] or in a 8-μm-thick water layer on top of the mirror and perpendicular to the optical axis z [Fig. 1(b)]. The mirror is located at the excitation laser beam ($\lambda_0=632.8$ nm) focal point and is a 16-layer stack whose design is $(HL)^{15}L$, where H and L stand, respectively, for a high ($n_H=2.2$, Ta_2O_5) and low ($n_L=1.5$, SiO_2) refractive index quarter-wavelength layer at $\lambda_1=660$ nm. The reflectance of this mirror in normal incidence is above 99% not only for the excitation wavelength λ_0 but as well for the Cy5 spectral bandwidth.

Let us consider first the mirror effect on the mean intensity collected per molecule. In our experiment, we set the laser power of 25 kW/cm^2 at the focal point. The average count rate per molecule goes from 2.1 kHz in the absence of the mirror to 6.8 kHz in its presence, so that it is a gain of 3.2 fold. We found a similar result with an aluminum mirror although the noise that it produced was higher. It is of common concern that the proper fluorescence of dielectric materials could enhance the background noise: it turned out that the average background count rate was not affected by the presence of the mirror and remains below 1 kHz. In comparison, our model (2D, aberration free) predicts a 4.5 enhancement factor, which is a nontrivial combination of (1) the enhancement of the excitation intensity by reflection and (2) the modification of the radiation pattern in the microscope lens NA resulting from the fluorescence reflection. In spite of this discrepancy, this result demonstrates that the mirror notably enhances the detected intensity.

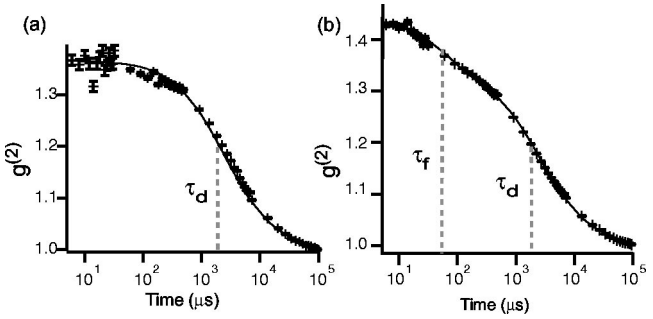

FIG. 2. Autocorrelation functions of diffusing particles (20-nm-diam nonobeads) in the absence (a) and presence (b) of the mirror. τ_d and τ_f represent the characteristic diffusion times through the confocal volume and the interference fringes, respectively.

To obtain information about dynamical processes at the molecular level, the detected fluorescence intensity $I_f(t)$ is analyzed in the form of the autocorrelation function

$$g^{(2)}(\tau)=\frac{\langle I_f(t)I_f(t+\tau)\rangle}{\langle I_f\rangle^2},$$

where $I_f(t)=q\int\int \mathrm{MDE}_m(\mathbf{r},z)\cdot C(\mathbf{r},z,t)d\mathbf{r}dz$, $C(r,z,t)$ is the time-dependent concentration and q is a factor taking into account emitter absorption and emission cross sections and detector efficiency. Two typical experimental autocorrelation functions obtained for diffusing fluorescent nanospheres (Crimson nanobeads from Molecular Probes, 20 nm diam) are shown in Fig. 2, one in the absence of the mirror the other in its presence. To switch over the configuration, was equivalent to removing the mirror or to bringing it away from the focal point of the laser. The integration time was 10 min for both experiments. A direct consequence of the enhancement of the molecule detection efficiency is that the standard deviation $\sigma(t)$ at any time scale (calculated with Koppel's formula[15]) is reduced in the presence of the mirror. At the concentration we used (5×10^{-10} M), the nanospheres are expected to undergo a 3D Brownian motion and exhibit Fickian dynamics. For the usual Gaussian confocal detection volume [Fig. 2(a)], $g^{(2)}(\tau)$ follows, indeed, the expression derived by Aragon and Pecóra for such motion:[16] $g_G^{(2)}(\tau)=1+1/N\times(1+4D\tau/w_0^2)^{-1}(1+4D\tau/z_0^2)^{-1/2}$, where D is the translational diffusion coefficient and N is the average number of fluorescent molecules in the sample volume. The time $\tau_d=w_0^2/4D$ is the characteristic diffusion time through the confocal collection volume.

For the fringe-patterned confocal volume in the presence of the mirror, our numerical simulation reveals the presence of a second characteristic time τ_f at short time, in good agreement with the experiment [Fig. 2(b)]. Neglecting the spatial contribution of the spontaneous emission control in $\mathrm{CEF}_m(\mathbf{r},z)$, we get an approximate analytical expression for the detected fluorescence intensity in the presence of the mirror

$$\mathrm{MDE}_m(\mathbf{r},z)=m\exp\left(-2\frac{r^2}{w_0^2}\right)\exp\left(-2\frac{z^2}{z_0^2}\right)\cos^2(kz), \quad (1)$$

TABLE I. Results extracted from the autocorrelation curves shown in Fig. 2. Diffusion coefficient D was calculated from τ_d and τ_f in the absence and in the presence of the mirror, respectively. Numerical values used were: $w_0 = 0.50 \pm 0.05$ μm, $\lambda_0 = 632.8$ nm, and $n = 1.33$.

	No mirror	Mirror
τ_d (μs)	2800 ± 200	2600 ± 200
τ_f (μs)	⋯	65 ± 5
$\frac{\tau_d}{\tau_f}$	⋯	40 ± 6
$\left(\frac{\tau_d}{\tau_f}\right)_{\text{calc}} = \left(\frac{2\pi n w_0}{\lambda_0}\right)^2$	⋯	44 ± 9
D (μm^2 s^{-1})	$\frac{w_0^2}{4\tau_d} = 22 \pm 6$	$\frac{\lambda_0^2}{16\pi^2 n^2 \tau_f} = 22 \pm 2$

where m is related to the excitation and emission mirror enhancement. Expression (1) leads to the correlation function[4] $g_f^{(2)}(\tau) = g_G^{(2)}(\tau)\ [1 + A \exp(-t/\tau_f)]$, where A is a constant and $\tau_f = \lambda_0^2/16\pi^2 n^2 D$. τ_f is only dependent on the interfringe spacing $\lambda_0/2n$, and contrary to τ_d, does not require any *a priori* knowledge of w_0.

Results of the fits are summarized in Table I. We calculated the ratio τ_d/τ_f from the fit results and compared it to its theoretical expression $(\tau_d/\tau_f)_{\text{calc}}$. The diffusion coefficient extracted from τ_f is in excellent agreement with the theoretical value obtained from the Stokes–Einstein formula: $D_{\text{Stokes}} = kT/6\pi\eta R = 24$ μm^2 s^{-1} (kT is the thermal energy, R is the radius of the nanobead, and η is the viscosity of the medium). The measurement of D from τ_f does not depend on the collection volume V in contrast to that from τ_d (the uncertainty on D calculated from τ_f is, therefore, lower, as shown in Table I). We checked this behavior by modifying V with a diaphram, under filling the NA of the microscope lens (data not shown). The time τ_d increases when the diaphragm closes since w_0 increases, while τ_f is not affected.

Although methods based on fringe patterns have been already used to study liquid state dynamics,[5,6,17] this is evidence of a patterned structure within a very small confocal volume and easily applicable in a conventional FCS setup. The precited methods use, generally, two intersecting laser beams that define a large excitation volume in contrast to our technique. Moreover, the use of a planar mirror does not allow only generating interference fringes, but also enhances the detected fluorescence signal. It makes, therefore, this method interesting for nonrobust fluorophores, too. In the future, we expect that the use of photonic structures will allow us to shape the collection volume in a more-controlled manner and offer the possibility of studying weak fluorescent molecules since photonic structures can be designed as ''fluorescence enhancers.'' This will be of particular interest for probing macromolecular diffusion in different compartments of living cells with subwavelength resolution and high detection efficiency.

The authors are grateful to J. G. Rarity for stimulating discussions.

[1] M. Orrit and J. Bernard, Phys. Rev. Lett. **65**, 2716 (1990).
[2] W. E. Moerner and L. Kador, Phys. Rev. Lett. **62**, 2535 (1989).
[3] E. L. Elson and D. Magde, Biopolymers **13**, 1 (1974).
[4] H. Asai and T. Ando, J. Phys. Soc. Jpn. **40**, 1527 (1976).
[5] M. Hattori, H. Shimizu, and H. Yokoyama, Rev. Sci. Instrum. **67**, 4064 (1996).
[6] M. K. Knowles, T. J. Grassman, and A. H. Marcus, Phys. Rev. Lett. **85**, 2837 (2000).
[7] S. Kitson, P. Jonsson, J. Rarity, and P. Tapster, Phys. Rev. A **58**, 620 (1998).
[8] C. Begon, H. Rigneault, P. Jonsson, and J. G. Rarity, Single Mol. **3**, 207 (2000).
[9] D. Koppel, D. Axelrod, J. Schlessinger, E. L. Elson, and W. Webb, Biophys. J. **16**, 1315 (1976).
[10] R. Rigler, Ü. Mets, J. Widengren, and P. Kask, Biophys. J. **22**, 169 (1993).
[11] J. Enderlein, Opt. Lett. **25**, 634 (2000).
[12] H. Benisty, H. De Neve, and C. Weisbuch, IEEE J. Quantum Electron. **34**, 1612 (1998).
[13] D. Deppe, C. Lei, C. Lin, and D. L. Huffaker, J. Mod. Opt. **41**, 325 (1994).
[14] H. Rigneault and S. Monneret, Phys. Rev. A **54**, 2356 (1996).
[15] D. E. Koppel, Phys. Rev. A **10**, 1938 (1974).
[16] S. R. Aragon and R. Pecóra, J. Chem. Phys. **64**, 1791 (1976).
[17] J. Davoust, P. Devaux, and L. Leger, EMBO J. **1**, 1233 (1982).

Enhancement of Single-Molecule Fluorescence Detection in Subwavelength Apertures

Hervé Rigneault,[1,*] Jérémie Capoulade,[1] José Dintinger,[2] Jérôme Wenger,[1] Nicolas Bonod,[1] Evgeni Popov,[1] Thomas W. Ebbesen,[2] and Pierre-François Lenne[1,†]

[1]*Institut Fresnel, Domaine Universitaire de Saint Jérôme, Université d'Aix-Marseille III, CNRS UMR 6133, 13397 Marseille Cedex 20, France*

[2]*ISIS, Université Louis Pasteur, CNRS UMR 7006, 8 allée G. Monge, 67000 Strasbourg, France*

(Received 9 December 2004; published 6 September 2005)

We report the experimental proof of molecular count rate enhancement (up to 6.5-fold) and lifetime reduction for single fluorescent molecules diffusing in subwavelength apertures milled in aluminum films. The observed enhancement dependence with the aperture diameter agrees qualitatively with numerical electromagnetic computations of the excitation power density into the aperture volume.

DOI: 10.1103/PhysRevLett.95.117401 PACS numbers: 78.67.−n, 32.50.+d, 81.07.−b, 82.37.Vb

In any single-molecule experiment, the weak fluorescence signal needs to be discriminated against the background. A strategy consists in enhancing the spontaneous emission by tailoring the electromagnetic environment the molecule can radiate into [1,2]. In principle, both the emission rate and the angular radiation pattern can be affected, and these fundamental effects have been investigated at the single-molecule level in near field optics experiments where a metal coated tip aperture is scanned above a fixed fluorescent molecule [3,4]. The influence of nanometric photonics structures to enhance single emitters radiation has recently gained interest since the observation of the enhanced fluorescence by a sharp metal tip [5] or nanometric particles in Raman scattering [6]. Much work has also been motivated by the discovery of the enhanced transmission phenomena where surface plasmons give rise to strong electromagnetic fields at the entrance of subwavelength apertures [7]. Of particular interest are isolated single holes (possibly surrounded by corrugated surfaces) where localized surface plasmon modes are involved [8,9] to enhance the transmission of light.

Fluorescence correlation spectroscopy (FCS) may offer new applications to characterize the use of nanophotonics devices. FCS is a well-known and powerful technique to study single-molecule fluorescence properties [10], where the fluctuations are analyzed by autocorrelating temporally the recorded photocount signal $n(t)$. This is quantified by the fluctuation autocorrelation function (ACF), $g^{(2)}(\tau) = \frac{\langle n(t)n(t+\tau)\rangle}{\langle n(t)\rangle^2}$ where $\langle\,\rangle$ stands for an ensemble averaging. Recently, Levene *et al.* [11] investigated for the first time the diffusion dynamics of single molecules in nanometric metallic apertures using FCS. In this work, tiny subwavelength holes (diameter $d < 80$ nm) were milled in aluminum films and were shown to act as small reaction chambers with an effective observation volume V_{eff} down to 10^{-21} l, allowing one to study chemical reactions at molecular concentrations up to 0.2 mM. Although no alteration of the spontaneous emission was reported in [11], a subwavelength aperture containing few molecular emitters is very similar to the near field optics experiments where drastic alteration of the spontaneous emission has been observed [3,4]. However, the tiny aperture diameter used in [11] may have prevented Levene and his coworkers from observing any alteration of the molecular fluorescence.

In this Letter, we investigate the potential of single nanometric apertures milled in metal films to enhance the photocount rate per molecule η in FCS experiments. This is performed by studying apertures with a diameter between 110 and 420 nm, thus significantly larger than in [11]. Using isolated single holes, we report a striking 6.5-fold enhancement of η as compared to free solution together with a significant decrease of the observation volume V_{eff} for small hole diameters. The fluorescence enhancement is associated with a dramatic reduction of the molecular lifetime, which demonstrates that the energy levels' branching ratios are affected for molecules located in subwavelength apertures. A fundamental point reported here is that the metal nanoaperture allows one, on one hand, to postpone the fluorescence saturation by affecting the molecular branching ratios, while, on the other hand, the local excitation intensity is increased by the aperture, thus yielding a net fluorescence rate per molecule significantly higher as compared to open solution. Numerical electromagnetic simulations using the differen-

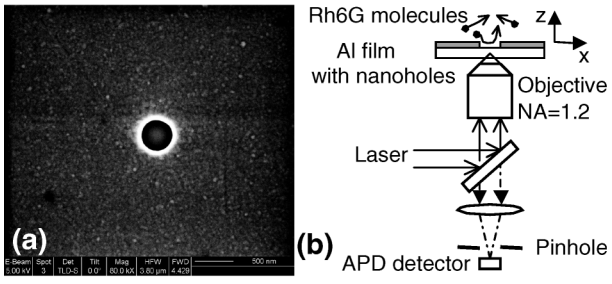

FIG. 1. (a) Scanning electron micrograph of an isolated subwavelength aperture milled in an Al film coated on a microscope slip. (b) Schematic view of the optical setup (APD: avalanche photodiode).

tial theory are implemented and give predictions consistent with our observations.

Optically thick Al metal films (thickness $h = 300$ nm) were coated on conventional microscope slips (thickness 150 μm) by thermal evaporation. Subwavelength apertures (diameter d from 110 to 420 nm) were fabricated by focused ion beam (FEI Strata DB235 using Ga^+ ions exhibiting a 5 nm nominal beam diameter). Figure 1 shows the scanning electron micrograph of such an aperture. FCS experiments were performed in a custom setup based on an inverted microscope (Zeiss Axiovert 200) with an NA = 1.2 objective lens (Zeiss C-Apochromat). Nanopositioning of the aperture was possible thanks to a multiaxis piezostage (Physik Instrumente P527). ACFs were recorded by a hardware correlator (ALV 6000) and fitted with IgorPro software (WAVEMETRICS). We used as fluorescent reporters Rhodamine 6G molecules (Rh6G) with an excitation wavelength of 488 nm provided by an argon ion laser (Fig. 1). Tight focusing conditions were used to shine a single subwavelength aperture with a beam waist of 250 nm (calibrated from FCS experiments carried out on Rh6G in solution). This setup provides an observation volume V_{eff} of 750 attoliters. For the experiments reported here, the laser polarization was set linear. The incoming power was kept below 1 mW at the back microscope lens aperture to avoid the sample damage. Two photons fluorescence lifetime of Rh6G was recorded by a time-to-amplitude converter (TimeHarp-PicoQuant) following a 4 MHz ps pulses train provided by a pulsed picked mode locked Ti:sapphire laser tuned at a wavelength of 800 nm.

Figure 2 presents the measured evolution of V_{eff} with the subwavelength aperture diameter d. Knowing the molecular concentration, the observation volume is deduced from the mean number of molecules N that is obtained from $g^{(2)}(0) = 1 + \frac{1}{N}(1 - \frac{\langle b \rangle}{\langle i \rangle})^2(1 + n_T)$ where $\langle i \rangle$ is the mean intensity, $\langle b \rangle$ the mean background, and n_T the triplet amplitude related to the fraction F of molecules in the triplet state by $F = n_T/(1 + n_T)$. Let us point out that this expression of $g^{(2)}(0)$ is independent of the shape of the excitation field and the type of molecular diffusion, and its validity holds for a stationary system and a dilute solution where the spatial correlation length of concentration fluctuations is much smaller than the detection volume [12]. For each experimental run, the triplet amplitude n_T was fitted to the raw experimental ACFs (assuming a free 3D diffusion; see Fig. 3). For instance, with an excitation power of 300 μW, n_T was found in the range $n_T = 0.35 \pm 0.15$ for the various nanohole diameters. The background noise b within the apertures was recorded with a nanohole filled with pure water [see the photocount trace and the $g^{(2)}(\tau)$ for the noise in Fig. 3]. b does not exhibit any time correlation. A clear reduction of V_{eff} is observed, which is always equal to or smaller than the geometrical nanohole volume ($\pi d^2 h/4$), suggesting that the electromagnetic fields involved in the FCS process are essentially limited to this volume. The 110 nm diameter aperture exhibits a V_{eff} of 1.8 attoliters enabling single-molecule detection for concentrations in the μM range. This volume reduction is associated with the reduction of the diffusion time across V_{eff} as illustrated by the ACF functions presented in Fig. 3, which are recorded in open solution and into a $d = 150$ nm

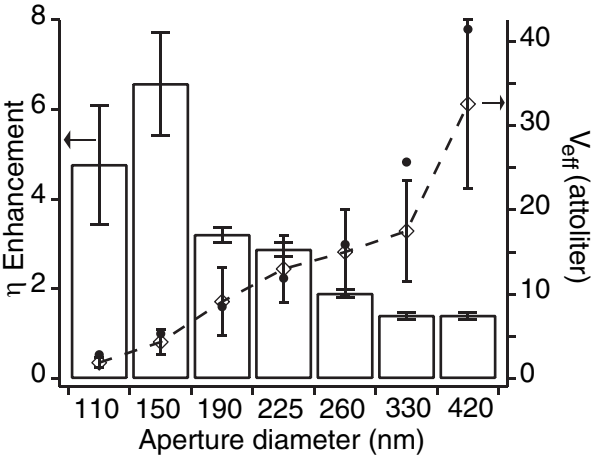

FIG. 2. V_{eff} evolution versus the aperture diameter (◇, right scale—dashed line to guide the eyes) and nanohole geometric volume (●, right scale). Enhancement of η (histogram, left scale) as compared to its value in open solution versus the aperture diameter ($P_{\text{ex}} = 0.2$ mW).

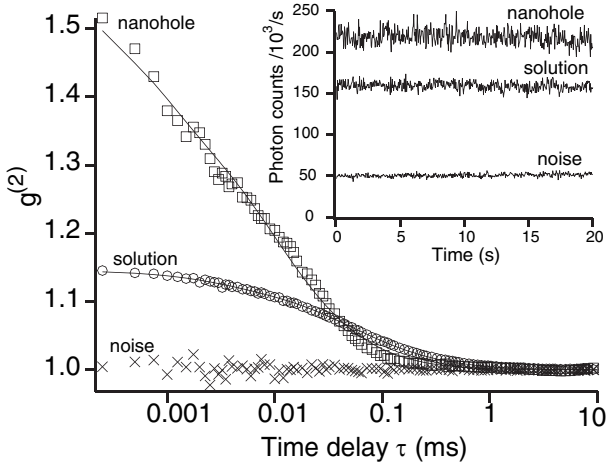

FIG. 3. Line traces and autocorrelation functions in open solution (○) in a 150 nm diameter aperture (□) and for the noise within the aperture (×) for an excitation power of 0.3 mW (the noise was negligible in open solution: <200 counts/s). The molecular concentration for the experiment in open solution was set to 20 nM, while it was taken to 600 nM within the aperture. For the open solution, numerical fits assuming a 3D free diffusion yield the set of parameters: $N = 7.8$, $n_T = 0.15$, diffusion time is 53 μs, count rate per molecule is 20 kHz. For the 150 nm aperture, $N = 1.5$, $n_T = 0.35$, diffusion time is 10 μs, count rate per molecule is 112 kHz.

aperture. We found that this diffusion time reduction is consistent with the measured V_{eff} shown in Fig. 2.

To study the ability of these nanostructures to alter single-molecule fluorescence detection, we investigated the evolution of the detected count rate per molecule η with the aperture diameter. This information is readily obtained in FCS measurements by dividing the photon counted signal by the number of molecules N present in V_{eff} computed from $g^{(2)}(0)$. Figure 2 presents the enhancement of η as compared to its value in open solution for an excitation laser power $P_{\text{ex}} = 0.2$ mW, at which the fluorescence is in the linear regime for FCS experiments carried out in the nanohole or in free solution. A significant enhancement is observed for the small holes' diameters ($<$200 nm) although a twofold enhancement is commonly seen for aperture diameters in the 250–400 nm range. Figure 4 shows the evolution of η with the excitation laser power in a 150 nm diameter aperture and in open solution. In the linear regime ($P_{\text{ex}} < 0.4$ mW), η was found up to $\sim$6.5 times stronger for the molecule diffusing within the subwavelength apertures as compared to open solution. For $P_{\text{ex}} > 0.4$ mW, η saturates to $\sim$30 kHz for Rh6G molecules in open solution, whereas the linear regime persists in nanoholes up to $P_{\text{ex}} \sim 1$ mW. Let us emphasize that since Rh6G is a high quantum efficiency dye, the triplet amplitude n_T remains quite small while increasing the excitation power. By fitting the experimental data for each excitation power, we found that n_T increased slowly with typically $n_T = 0.25$ at 150 μW and $n_T = 0.5$ at 900 μW for a 150 nm nanohole. We confirmed that no bleaching processes were involved in the saturation curve in open solution or in the nanoholes as the diffusion time and the number of molecule remain constant with increasing power. A striking η of 350 kHz was recorded into the 150 nm aperture for $P_{\text{ex}} = 1$ mW, in this case the apparent enhancement reaches 12.

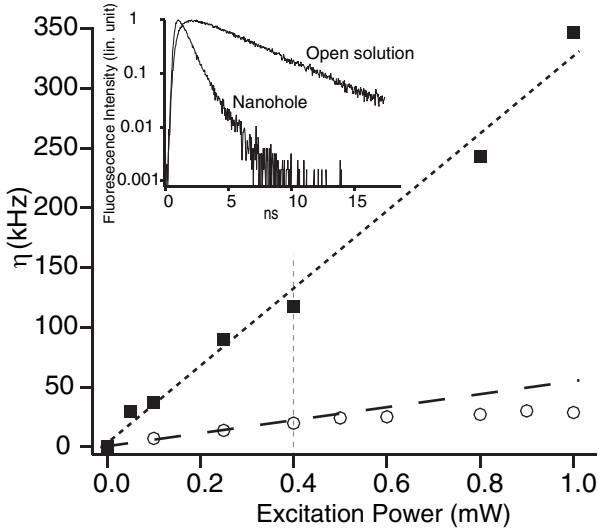

FIG. 4. Evolution of η versus the incident power P_{ex} in a 150 nm aperture (■) and in open free solution (○). Inset: Fluorescence decay curves in open solution and into a $d =$ 150 nm nanohole.

To get insight into the radiative processes involved in this fluorescence enhancement, we investigated the molecular excited state lifetime inside the nanoholes as compared to open solution. The inset of Fig. 4 shows the fluorescence radiative decay curve in open solution and into a $d = 150$ nm aperture. A striking reduction from 3.7 ns in open solution down to our apparatus response time (0.9 ns) is observed in good agreement with the previously observed lifetime reduction at the rim of the metallic tip in near field optics [13,14]. This shows that the molecular energy levels branching ratios are affected for dye molecules diffusing in nanoholes as compared to open solution, allowing for a delay of the fluorescence saturation inside the subwavelength apertures. Although nonradiative processes due to the metal surface must be involved in the observed lifetime reduction, the enhancement of η demonstrates that the overall effect acts in favor of the radiative processes as compared to open solution. In addition to the possible alteration of the intersystem branching ratio, a coupling between the molecule and plasmon resonances may also increase the radiative rate.

Several physical arguments can contribute to the observed enhancement, which can be simply written as $\eta = \frac{1}{N} \int \text{CEF}(r) I_{\text{ex}}(r) dr$, where N is the FCS mean number of molecules present in V_{eff}, $I_{\text{ex}}(r)$ is the local excitation intensity, and CEF(r) stands for the local collection efficiency function [15]. This expression is valid when no saturation occurs. Note that CEF(r) stands for the electromagnetic power emitted by a dipole located at $\mathbf{r}$, which is collected by the detector; in this respect, it includes the radiation pattern alteration and the possible lifetime reduction. Both the CEF(r) and $I_{\text{ex}}(r)$ are expected to be affected by the metallic subwavelength aperture boundary conditions as compared to open solution [16]. The observed η enhancement cannot be solely due to an increase of $I_{\text{ex}}(r)$ because otherwise one would expect the fluorescence to saturate as in open solution, without yielding any supplementary photocount. On the other hand, an alteration of the molecular radiation pattern collection could increase CEF(r) only by, at most, a factor of 3.3 since the objective microscope lens already collects 30% of the emitted light in open solution. In this case the saturation would be expected at $30 \times 3.3 \sim 100$ kHz in nanoholes. Because of the dramatic fluorescence lifetime reduction inside the nanohole, we conclude that the molecular energy levels' branching ratios are affected, leading to a delay in the fluorescence saturation.

The complete description of the process would require the calculation of the CEF(r) and is beyond the scope of this paper. We rather focus here on the role played by the excitation field $I_{\text{ex}}(r)$ on η. We therefore made the assump-

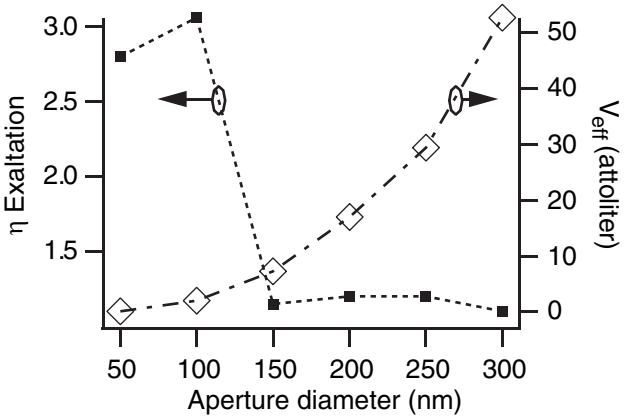

FIG. 5. Results of simulations in a 200 nm thick metal film. Count rate per molecule η (normalized to the open solution case) and effective volume V_{eff} as a function of the aperture diameter.

tion that $\mathrm{CEF}(r) = 1$ to compute η and the effective FCS volume [15] defined in this case as $V_{\mathrm{eff}} = \frac{(\int I_{\mathrm{ex}}(r)dr)^2}{\int I_{\mathrm{ex}}{}^2(r)dr}$. To perform such calculations in a single circular hole drilled in a plane metallic sheet, we use the generalized differential theory that we have recently developed to study diffractive structures described in cylindrical coordinates [17,18]. Figure 5 presents the computed evolution of η (normalized to open solution) and V_{eff} with the aperture diameter. Numerical convergence constraints [17,18] make impossible the modelling of very highly conducting metals and, we have used material with lower conductivity. In order to preserve almost the same decay depth of the field in the aperture, the calculation were performed with a collimated beam incoming on a 200 nm thick metal layer with and $\epsilon = -8 + i3$, which is different from the real case ($h = 300$ nm and $\epsilon_{\mathrm{AL}} = -30 + i7$). Despite this difference and the $\mathrm{CEF}(r) = 1$ assumption, we observe a clear reduction of V_{eff}. The striking feature is the enhancement of η for the small diameter apertures (around 100 nm). Numerical results indicate that this behavior is related to the field enhancement, which takes place at the edge of the nanohole [9,19,20]. This field enhancement is due to the plasmon excitation and is localized close to the holes' edges. When compared to the total aperture surface, the region of the enhanced field is relatively larger for smaller apertures than for larger ones, thus leading to an enhancement of η. For very small diameters (<100 nm), the field penetrates at a very small depth inside the hole, and this edge effect becomes less important.

These numerical simulations are qualitatively consistent with our experimental observations. Nevertheless, the 6.5-fold enhancement of η experimentally observed is not explained and requires a deeper investigation of the radiation pattern and the lifetime changes of a source located inside a nanohole.

In conclusion, we have investigated by FCS the fluorescence of individual molecules diffusing in subwavelength apertures milled in aluminum films. Besides the reduction of the observation volume, we report a significant enhancement of the count rate per molecule for small aperture diameters. Because the fluorescence lifetime is dramatically reduced in nanohole, we conclude that the molecular energy levels' branching ratios are affected leading to a delay in the fluorescence saturation. The combination of this effect together with an increase in the local excitation intensity induced by the metal aperture yields an overall fluorescence enhancement as compared to open solution. The experimental observations are qualitatively confirmed by electromagnetic calculations of the excitation field density inside the aperture. By taking benefit of this significant enhancement, such apertures could serve as efficient nano-optical sources or nanowells for fast and highly parallel molecular analysis at high concentration.

The authors are grateful to J. M. Gérard and M. Nevière for stimulating discussions and M. Cathelinaud for the realization of the aluminum coatings. This work was funded by the "ACI Nanosciences" of the Research French Ministry.

*Electronic address: herve.rigneault@fresnel.fr
†Electronic address: lenne@fresnel.fr

[1] E. M. Purcell, Phys. Rev. **69**, 681 (1946).
[2] K. H. Drexhage, Prog. Opt. **12**, 163 (1974).
[3] X. S. Xie and R. C. Dunn, Science **265**, 361 (1994).
[4] H. Gersen *et al.*, Phys. Rev. Lett. **85**, 5312 (2000).
[5] E. J. Sánchez, L. Novotny, and X. S. Xie, Phys. Rev. Lett. **82**, 4014 (1999).
[6] S. Nie and S. R. Emory, Science **275**, 1102 (1997).
[7] T. W. Ebbesen *et al.*, Nature (London) **391**, 667 (1998).
[8] H. J. Lezec *et al.*, Science **297**, 820 (2002).
[9] A. Degiron *et al.*, Opt. Commun. **239**, 61 (2004).
[10] D. Magde, E. Elson, and W. W. Webb, Phys. Rev. Lett. **29**, 705 (1972).
[11] M. J. Levene *et al.*, Science **299**, 682 (2003).
[12] E. L. Elson and D. Magde, Biopolymers **13**, 1 (1974).
[13] W. P. Ambrose *et al.*, Science **265**, 364 (1994).
[14] L. Novotny, Appl. Phys. Lett. **69**, 3806 (1996).
[15] R. Rigler *et al.*, Eur. Biophys. J. **22**, 169 (1993).
[16] H. Rigneault and P. F. Lenne, J. Opt. Soc. Am. B **20**, 2203 (2003).
[17] E. Popov, M. Neviere, and N. Bonod, J. Opt. Soc. Am. A **21**, 46 (2004).
[18] N. Bonod, E. Popov, and M. Neviere, J. Opt. Soc. Am. A **22**, 481 (2005).
[19] A. R. Zakharian, M. Mansuripur, and J. V. Moloney, Opt. Express **12**, 2631 (2004).
[20] L. Yin *et al.*, Appl. Phys. Lett. **85**, 467 (2004).

Chapitre 4

Projet de recherche

Après quelques années consacrées à l'organisation de la membrane biologique et aux structures photoniques, j'ai décidé de m'orienter vers un sujet différent portant sur la géométrie et la dynamique des épithélia. Il revêt plusieurs facettes, certaines étant en lien étroit avec mes études antérieures (domaines membranaires et cytosquelette), d'autres plus éloignées (modélisation inspirée de la physique des mousses). Les projets que je vais présenter sont expérimentaux et théoriques, motivés par mon désir de décrire quantitativement certains processus du vivant et de les modéliser.

Au cours du développement de l'embryon et lors de la formation des organes, les cellules changent de forme et modifient leurs contacts de façon très dynamique. Les interactions cellulaires sont finement régulées pour permettre un équilibre entre robustesse et plasticité du tissu biologique. La morphogenèse tissulaire dépend en partie d'un processus universel dit d'intercalation, au cours duquel les cellules changent de position et de voisine de façon ordonnée. J'étudierai cette question fondamentale en prenant comme système modèle l'embryon précoce de Drosophile, en collaboration avec le Laboratoire de Biologie de Béveloppement de Marseille-Lumniny (IBDML, Equipe de Thomas Lecuit)

En raison de sa simplicité, l'embryon de Drosophile est un système dont on peut extraire des grandeurs quantitatives à partir de données expérimentales et il se prête bien aux modélisations décrivant par exemple les propriétés mécaniques des cellules de l'embryon.

4.1 Dynamique et organisation des domaines d'E-cadhérine

Un des acteurs importants de l'adhesion entre des cellules épithéliales est l'E-cadhérine (E-cad). Les E-cad sont des protéines transmembranaires capables de former des complexes homophiliques conduisant à l'adhésion entre cellules adjacentes. La répartition de ces complexes doit être finement régulée pour permettre le remodelage des jonctions adhérentes et doit être couplée dans une certaine mesure à l'organisation du cytosquelette cellulaire. On considère couramment que les E-cad contribuent à l'adhésion en s'associant tout d'abord en dimères sur la même surface cellulaire (configuration *cis*), puis s'attachent à des dimères d'une cellule adjacente pour former des liaisons adhérentes (*trans*). Si les mécanismes de l'adhésion médiée par l'E-cadherine sont assez bien étudiés et connus aux échelles moléculaire et macroscopique, l'organisation et la dynamique mésoscopique de ces structures sont peu documentées.

Le but de mon projet est de décrire quantitativement et de prédire comment les molécules d'E-cad s'organisent à la surface cellulaire. Nous aborderons ce problème en associant des données expérimentales et le développement d'outils de modélisation permettant de rendre compte de la formation et la stabilisation de structures d'adhésion. Les molécules d'E-cad diffusent dans la membrane d'une manière largement indéterminée et s'associent par ailleurs en complexes ordonnés formant des microdomaines entre 70 et plusieurs centaines de nm (visibles et quantifiables en microscopie électronique ou en microscopie confocale). Cette structure mosaïque est activement maintenue dans la cellule et représente un état d'organisation intermédiaire hors équilibre entre une distribution aléatoire de molécules E-cad et leur partage en deux phases, une contenant toutes les molécules d'E-cad homophiliques, et l'autre totalement dépourvue de molécules d'E-cad. Des données expérimentales permettront de mieux déterminer le régime de concentrations d'E-cad à la surface cellulaire compatibles avec la formation de ces microdomaines, les modes de diffusion d'E-cad à différentes échelles de temps, la diffusion de ces microdomaines et leur fusion en *cis*. On analysera aussi le rôle de l'endocytose de l'E-cad homophilique. Par ailleurs nous chercherons à modéliser l'assemblage de ces microdomaines en prenant en compte la concentration et la diffusion aléatoire des molécules d'E-cad, leur association à des microdomaines, la mobilité de ces microdomaines et leur croissance par fusion, ainsi que leur décroissance par endocytose. Cette modélisation permettra notamment d'extraire une loi de croissance temporelle de ces microdomaines et de se doter d'outils

prédictifs à partir de données précises. La combinaison d'approches expérimentales permettant d'extraire le maximum de paramètres quantitatifs et d'outils de modélisation permettant de vérifier notre compréhension de l'organisation dynamique de molécules d'E-cad constituera l'élément original de ce projet.

4.2 Mécanique des jonctions adhérentes

L'intercalation dépend d'un remodelage polarisé dans le plan de l'épithélium des interfaces cellulaires, et en particulier des jonctions adhérentes. La géométrie des interfaces cellulaires suit une transformation irréversible comprenant la disparition puis la formation d'une nouvelle jonction adhérente[6] (Figure 4.1).

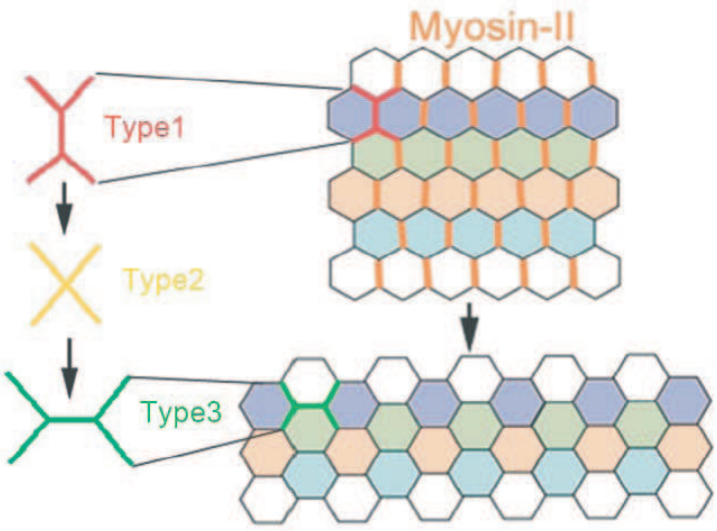

FIG. 4.1 – L'intercalation cellulaire est un moyen d'allonger un tissu. Les jonctions verticales (type 1) disparaissent et laissent place à des jonctions horizontales (type 3). La transition nécessite un recrutement des myosines-II au niveau des jonctions de type 1.

Ce processus ne dépend pas des forces extrinsèques au tissu mais certainement des forces locales opérant aux interfaces jonctionnelles. La Myosine-II est enrichie dans des jonctions instables et est un moteur essentiel du remodelage polarisé des jonctions.

[6]Bertet C, Sulak L, Lecuit T : Myosin-dependent junction remodelling controls planar cell intercalation and axis elongation. Nature 2004, 429 :667-671.

Nous chercherons à : 1-) modéliser simplement le processus par un modèle inspiré de la physique des mousses ; 2-) développer des méthodes spécifiques pour mesurer les forces de tension locale du réseau d'acto-myosine et en déterminer le rôle.

4.2.1 Simulations de type mousse

Un premier axe de recherche consiste à développer un modèle inspiré de la physique des mousses prenant en compte la tension de surface comme le paramètre principal gouvernant la forme des cellules et donc la stabilité des interfaces cellulaires au cours de l'intercalation[7].

Nous considérons le cas d'une assemblée bidimensionnelle de N cellules en contact, de surface constante, et nous faisons l'hypothèse que l'énergie du tissu s'écrit comme la somme des énergies des interfaces cellulaires :

$$E = \sum_{1 \leq i < j \leq N} \gamma_{ij} l_{ij} \tag{4.1}$$

où γ_{ij} est la tension de ligne de l'interface entre les cellules i et j, et l_{ij} sa longueur. γ_{ij} s'exprime en $J.m^{-1}$. Dans le cas d'une mousse constituée de bulles de savon, γ_{ij} est une constante indépendante de l'interface et la minimisation d'énergie du système est un problème purement géométrique de minimisation du périmètre total de la mousse. La dépendance de la tension de ligne en fonction de l'interface est introduite pour modéliser l'anisotropie de tension des jonctions cellulaires. Nous testerons si une anisotropie de tension de surface suffit à générer un processus intercalant *in silico*, et déterminerons les valeurs de tension de surface nécessaires à ce processus.

Par ailleurs, nous développerons des outils d'analyse permettant de décrire les données expérimentales (images confocales principalement) en terme de forme géométriques, changements de forme, anisotropie et transitions de voisinage. Pour cela, nous mettrons en œuvre des descripteurs utilisés dans la physique des mousses. Les configurations initiales des cellules réelles serviront de données initiales pour les simulations. Cette étude autorisera une comparaison de l'évolution *in silico* des interfaces cellulaires et les données expérimentales réelles.

[7] Ce type d'approche a été utilisé avec succès pour prédire la forme des arrangements cellulaires de la rétine de la drosophile (Hayashi T, Carthew RW : Surface mechanics mediate pattern formation in the developing retina. Nature 2004, 431 :647-652.)

4.2.2 Mesures mécaniques

Pour mesurer *in situ* les tensions mécaniques présentes aux interfaces cellulaires, nous développerons en premier lieu un système expérimental de "nanodissection". Il s'appuiera sur un montage de microscopie comportant un laser infra rouge femtoseconde, permettant de casser des structures sub-cellulaires (Figure 4.2). Ce type d'approche a été suivie avec succès par plusieurs équipes dans le monde, comme celles de K. König à l'université de Jena ou d'E. Mazur à l'université de Harvard. Grâce à cet outil, nous romprons certains contacts cellulaires ou le réseau cortical sous-jacent et mesurerons les temps caractéristiques de relaxation, qui sont liés aux paramètres de tension et de visco-élasticité.

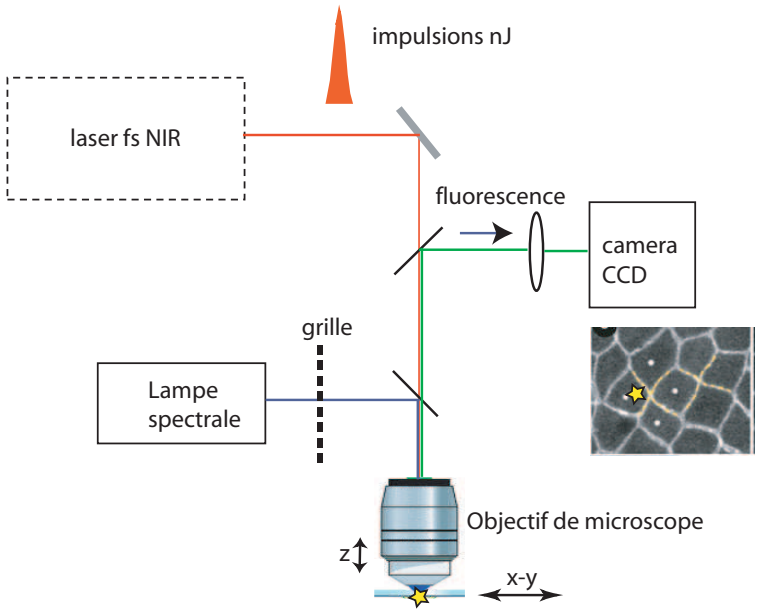

FIG. 4.2 – Schéma de l'expérience de nanodissection. Des impulsions femtosecondes sont focalisées par un objectif de microscope sur l'échantillon. L'imagerie est réalisée par illumination structurée.

Par ailleurs, nous développerons un système expérimental permettant de mesurer les corrélations spatiales et temporelles des fluctuations de fluorescence du réseau cortical d'acto-myosine, afin de déterminer les propriétés rhéologiques du cortex cellulaire (mesures de type FCS).

L'ensemble de ces expériences permettra de mesurer les propriétés visco-élastiques du cortex cellulaire, tester le rôle de la Myosine et de l'actine dans ce contexte et déterminer si une anisotropie de tension corticale contrôle l'intercalation.

4.3 Modèle dynamique de la morphogénèse

Les données expérimentales sur le réseau cortical et l'assemblage moléculaire des structures d'adhésion seront ensuite incorporées dans un modèle mécanistique plus élaboré que le modèle inspiré de la physique des mousses. Ce modèle dynamique de la morphogénèse visera à prédire les formes cellulaires et leur réarrangement à partir des forces sub-cellulaires locales agissant dans des cellules assemblées en tissu. Ce modèle permettra d'établir le lien entre les propriétés cellulaires locales et la dynamique d'arrangement d'un tissu. Nous pourrons déterminer ainsi quels processus dépendent des propriétés locales d'adhésion et de tension, et ceux qui découlent d'une contrainte physique externe, due par exemple à des contacts mécaniques avec des tissus adjacents.

4.4 Conclusion

Ces trois projets reposent donc sur la complémentarité entre des approches expérimentales originales et de modélisation. L'expérience nous fournira les grandeurs physiques caractérisant l'organisation biologique à différentes échelles (moléculaire, cellulaire et tissulaire), tandis que la modélisation pourra nous indiquer, en relation avec l'expérience, quels paramètres sont nécessaires et suffisants pour rendre compte de l'état d'organisation et dans quelle proportion. Une compréhension approfondie de ces systèmes organisés dépendra d'une bonne adéquation entre les prédictions des modèles quantitatifs et les données expérimentales.

Bibliographie

[1] Wenger J, Conchonaud F, Dintinger J, Wawrezinieck L, Ebbesen T, Boned A, Rigneault H, Marguet D, Lenne PF : **Diffusion analysis within single nanometric apertures reveals the ultrafine cell membrane organization**. *Biophys. J.* 2007, **in the press**.

[2] Djaker N, Gachet D, Sandeau N, Lenne PF, Rigneault H : **Refractive effects in coherent anti-Stokes Raman scattering microscopy.** *Appl. Opt.* 2006, **45**(27) :7005–7011.

[3] Etienne E, Lenne PF, Sturgis JN, Rigneault H : **Confined diffusion in tubular structures analyzed by fluorescence correlation spectroscopy on a mirror.** *Appl. Opt.* 2006, **45**(18) :4497–4507.

[4] Lenne PF, Wawrezinieck L, Conchonaud F, Wurtz O, Boned A, Guo XJ, Rigneault H, He HT, Marguet D : **Dynamic molecular confinement in the plasma membrane by microdomains and the cytoskeleton meshwork**. *EMBO J.* 2006, **25**(14) :3245–56.

[5] Marguet D, Lenne PF, Rigneault H, He HT : **Dynamics in the plasma membrane : how to combine fluidity and order**. *EMBO J.* 2006, **25**(15) :3446–57.

[6] Monneret H, Rauzi M, Lenne PF : **Highly flexible whole-field sectioning microscope with liquid-crystal light modulator**. *J. Opt. A : Pure Appl. Opt.* 2006, **8** :S461–S466.

[7] Popov E, Nevière M, Wenger J, Lenne PF, Rigneault H, Chaumet P, Bonod N, Dintinger J, Ebbesen T : **Field enhancement in single subwavelength apertures**. *J. Opt. Soc. Am. A* 2006, **23**(9) :2342–2348.

[8] Rigneault H, Lenne PF : **Nano-biophotonics**. In *Nanophotonics*. Edited by Rigneault H, Lourtioz JM, Delalande C, Levenson A, ISTE 2006 :293–317.

[9] Wenger J, Dintinger J, Bonod N, Popov E, Lenne PF, Ebbesen T, Rigneault H : **Raman scattering and fluorescence emission in a single nanoaperture : Optimizing the local intensity enhancement**. *Opt. Comm.* 2006, **267** :224–228.

[10] Wenger J, Lenne PF, Popov E, Capoulade J, Rigneault H, Dintinger J, Ebbesen TW : **Nanopuits métalliques pour exalter les contrastes en microscopie optique**. *Photoniques* 2006, **23** :44–46.

[11] Wenger J, Rigneault H, Dintinger J, Marguet D, Lenne PF : **Single-fluorophore**

diffusion in a lipid membrane over a subwavelength aperture. *J. Biol. Phys.* 2006, **32** :SN1–SN4.

[12] Lenne PF, Rigneault H : **Applications des lasers impulsionnels en biologie : génération de contraste et résolution**. In *Lasers et technologies femtosecondes*, Saint Etienne : Publications de l'Université de Saint Etienne 2005.

[13] Popov E, Bonod N, Nevière M, Rigneault H, Lenne PF, Chaumet P : **Surface plasmon excitation on a single subwavelength hole in a metallic sheet.** *Appl. Opt.* 2005, **44**(12) :2332–2337.

[14] Rigneault H, Capoulade J, Dintinger J, Wenger J, Bonod N, Popov E, Ebbesen TW, Lenne PF : **Enhancement of single-molecule fluorescence detection in subwavelength apertures.** *Phys. Rev. Lett.* 2005, **95**(11) :117401–404.

[15] Rigneault H, Lenne PF : **Nanobiophotonique**. In *Nanophotonique*. Edited by Rigneault H, Lourtioz JM, Delalande C, Levenson A, Hermes Science - Lavoisier 2005 :311–336.

[16] Sandeau N, Giovannini H, Lenne PF, Rigneault H : **Observation of the interferences between the emitted beams in a 4Pi microscope by partial coherence interferometry**. *Appl. Phys. Lett.* 2005, **87** :181103–4.

[17] Wawrezinieck L, Rigneault H, Marguet D, Lenne PF : **Fluorescence correlation spectroscopy diffusion laws to probe the submicron cell membrane organization.** *Biophys. J.* 2005, **89**(6) :4029–4042.

[18] Wenger J, Lenne PF, Popov E, Dintinger J, Ebbesen T, Rigneault H : **Single molecule fluorescence in rectangular nano-apertures**. *Opt. Express* 2005, **13**(18) :7035–7044.

[19] Rigneault H, Lenne PF : **Fluorescence correlation spectroscopy on a mirror**. *J. Opt. Soc. Am. B* 2003, **20** :2203–2214.

[20] Altmann S, Grunberg R, Lenne PF, Ylanne J, Raae A, Herbert K, Saraste M, Nilges M, Horber J : **Pathways and intermediates in forced unfolding of spectrin repeats.** *Structure* 2002, **10**(8) :1085–1096.

[21] Altmann SM, Lenne PF : **Forced unfolding of single proteins.** In *Atomic Force Microscopy in Cell Biology, Volume 68.* Edited by Jena BP, Hörber JKH, Academic Press 2002 :311–335.

[22] Courty S, Lebeau L, Martel L, Lenne PF, Balavoine F, Dishert W, Konovalov O, Mioskowski C, Legrand JF, Venien-Bryan C : **Two-dimensional crystallization of a histidine-tagged protein on monolayers of fluidity-enhanced Ni2+-chelating lipids**. *Langmuir* 2002, **24** :9502 – 9512.

[23] Lenne PF, Rigneault H, L Escoubas WL, Giovannini H : **Dispositif de mesure des propriétés optiques de l'oeil**. *Brevet FR2837373 - WO03077739* 2002.

[24] Lenne PF, Colombo D, Giovannini H, Rigneault H : **Flow profiles and directionality in microcapillaries measured by fluorescence correlation spectroscopy**. *Single Molecules* 2002, **3**(4) :194–200.

[25] Lenne PF, Etienne E, Rigneault H : **Subwavelength patterns and high detection efficiency in fluorescence correlation spectroscopy using photonic structures**. *Appl. Phys. Lett.* 2002, **80**(22) :4106–4108.

[26] Altmann SM, Lenne PF, Hörber JKH : **Multiple sensor stabilization system for local probe microscopes**. *Rev. Sci. Instrum.* 2001, **72** :142–149.

[27] Rigneaut H, Lenne PF : **Dispositif permettant la détection exaltée et l'analyse de la diffusion de particules luminescentes ou réfléchissantes optiquement**. *Brevet FR63860M - WO03010523* 2001.

[28] Lenne PF, Bonosi F, A R, Bellet-Amalric E, Legrand JF, Petit JM, Rieutord F, Berge B : **Growth of two-dimensional solids in alcohol monolayers in the presence of soluble amphiphilic molecules**. *Langmuir* 2000, **16**(5) :2306–2310.

[29] Lenne PF, Berge B, Renault A, Zakri C, Vénien-Bryan C, Courty S, Balavoine F, Bergsma-Schutter W, Brisson A, Grübel G, Boudet N, Konovalov O, Legrand JF : **Synchrotron radiation diffraction from two-dimensional protein crystals at the air/water interface.** *Biophys J* 2000, **79** :496–500.

[30] Lenne PF, Raae AJ, Altmann SM, Saraste M, Hörber JK : **States and transitions during forced unfolding of a single spectrin repeat.** *FEBS Lett.* 2000, **476**(3) :124–128.

[31] Renault A, Lenne PF, Zakri C, Aradian A, Vénien-Bryan C, Amblard F : **Surface-induced polymerization of actin.** *Biophys J* 1999, **76**(3) :1580–1590.

[32] Berge B, Lenne PF, Renault A : **X-ray grazing incidence diffraction on monolayers at the surface of water**. *Curr. Opin. Colloid Interface Sci.* 1998, **3**(3) :321–326.

[33] Venien-Bryan C, Lenne PF, Zakri C, Renault A, Brisson A, Legrand JF, Berge B : **Characterization of the growth of 2D protein crystals on a lipid monolayer by ellipsometry and rigidity measurements coupled to electron microscopy**. *Biophys. J.* 1998, **74**(5) :2649–57.

[34] Lenne PF, Valance A, Bonosi F, Berge B, Misbah C : **Growth morphologies during 2D solidification of Langmuir Monolayers Limited by both Surface and Bulk diffusion**. *Europhys. Lett.* 1997, **38**(4) :301 – 306.

[35] Hawker P, Lenne PF, Tonouchi M, Rampton VW, Mellor CJ, Henini M : **Surface-Acoustic-Wave Absorption By Edge Magnetoplasmons in the 2DHG At a GaAs/AlGaAs Heterojunction**. *Physica B* 1994, **194** :419–420.